The development of an SPH tree-based algorithm to investigate the evolution of self-gravitating Protoplanetary Disks.

Scuola di dottorato Vito Volterra

Dottorato di Ricerca in Astronomy, Astrophysics and Space Science – XXX Ciclo

Candidate

Luis Diego Pinto
ID number 1064576

Thesis Advisor	Co-Advisor
Prof. Roberto Capuzzo Dolcetta	Dr. Gianfranco Magni

A thesis submitted in partial fulfillment of the requirements
for the degree of Doctor of Philosophy in Astronomy, Astrophysics and Space Science

December 2017

Contents

Chapter 1

Introduction

Nowadays, *Circumstellar Disks* represent a very modern object of investigation, for many reasons. First, the investigation on their evolution aims at explaining the configuration of several thousand of planetary systems detected so far and may give important answers even on the formation of Solar System. Secondly, the early development of the interferometric technique to observe in the infrared and mm wave-length, opened a wide range of possibilities to observe disks with very short angular resolution, so they constitute a wide target, stimulating the application and the improvement of the most advanced observational techniques. Thirdly, not less important, disks systems involve several physical processes, both dynamical and hydrodynamical, they are indeed one of the most important objects of application of several sophisticated numerical techniques. Furthermore, the circumbinary disks have become, since the last 20 years, a key target in the field of star clusters. Their evolution of heterogeneous context-rich of stars and gas represents a new frontier for the Numerical Astronomy because it carries several issues still not overcome. For such purposes, our research group aims at building a suitable numerical environment, able to face this and many other analogous problems. The aim of this work is to present a new Algorithm developed to treat the interaction of gaseous systems (both selfgravitating and non-selfgravitating). The Code is based on the well-known Lagrangian Smoothed Particle Hydrodynamics approach, and contains a numerical technique to couple a few amount of point-mass particles, evaluating, with high precision, their motion. The calculus of self-gravity is accomplished with a tree-scheme approach.

The following chapter will give an introduction to the object of our investigations: the protoplanetary disks, illustrating the basic schematizations with which they are modelled, and remarking their importance in the context of Star Clusters.

The third chapter is dedicated to the introduction and the description of the code, illustrating the formalism of the Smoothed Particle Hydrodynamics tree-based codes and showing the peculiar formulations that we implemented.

In the fourth chapter, a series of test will be shown, both validation tests applied to physical problems of well-known analytical solutions, and scalability tests finalized to illustrate the main performances of the algorithm.

Chapter 5 treats the main scientific targets we focused on, by applying our code to investigate on the Protoplanetary disks perturbations induced by passing-by stars.

In Chapter 6 we will show the conclusions and some remarks for further developments of the work.

Chapter 2

Protoplanetary Disks

2.1 An overview of Extrasolar Systems

Up to the present day, the existence of 3,529 exoplanets has been confirmed (according to the NASA official catalog https://exoplanets.nasa.gov/). They orbit in 2,633 Solar-like Systems; dynamical and physical characteristics of such environments is often far different from the one of our Solar System. Such a circumstance led the astronomers to reconsider several paradigms of planet formation which were based just on the models for the Solar System. Furthermore, the recent discovery of 87 binaries and of 24 multiple star systems both hosting planets, opened new perspectives on the theory of planet formation in so complex and unstable environments. Planetary systems are thought to arise from the condensation of matter belonging to primordial gaseous *circumstellar disks*. Such disks form from the condensation of a gravitationally unstable dusty-gas nebula, in the very early phases of star formation. After that, the nebula starts to collapse, due to its rotation assumes a flat shape. In the meanwhile, at the center of the system, the very strong condensation of matter gives rise to a protostar. All the remnant matter of the nebula keeps on falling towards the flat distribution of gas constituted around the star, until a final system is constituted: a central pre-main sequence star, or a binary star, surrounded by a rotating *protoplanetary disk* in hydrodynamical equilibrium. This process is mainly driven by the specific angular momentum of the initial molecular cloud and of the infalling gas (for an exhaustive comprehension about the general processes of matter condensation, star formation and planetary system constitution, see for example Lissauer, 1993, Shu et al., 1987). After this stage, a disk necessarily dissolves, due to intrisic processes (turbulent dissipation) or interaction with the central star (stellar wind), but during its survival, accretion process on gas and dust take place, forming planets with different mass and structure. Since the last 20 years, it was clear that two are the main processes which can trigger the planet formation. One requires relatively short timescales ($\approx 10^3 \div 10^4$ yr) and involve the condensation of gas through gravitational instabilities, leading to the formation of giant gaseous planets (see Boss, 1997, 1998, 2003, Mayer et al., 2002, Mayer et al., 2004, for wide examples of numerical investigations). Another process, the core accretion, leads to the formation of the rocky planets by means of a series of subsequent aggregation phases (Lissauer, 1987). Since the early phases of disk formation, dust grains aggregates by forming larger and larger solid units, until $1km$-sized planetesimal are constituted. The aggregation of planetesimal will give rise to planets. All such processes are more complex and request time-scales of the order of $10^6 \div 10^7 yr$ which may be the same timescale, as it will be discussed below, of disk dissipation.

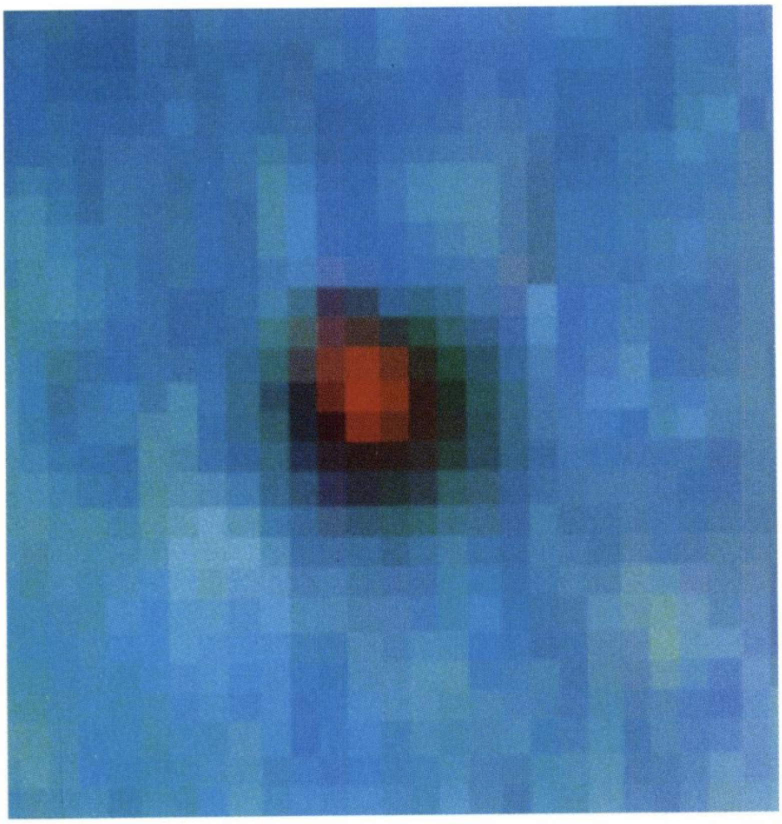

Figure 2.1. Evidence of circumstellar disk in the Orion Nebula Cluster : the Hubble Space Telescope discovers IR light (in 2.2 μm band) coming from a disk which covers a pre-main sequence star. (from O'dell et al., 1993, , pp. P14)

As pointed out above, protoplanetary disks are mainly made of dust(μm-scaled grains), and gas (mainly molecular hydrogen).The observation of such systems has always been a hard issue, for two kinds of reasons. Firstly, gas is the main component in terms of mass but is very difficult to observe since the H_2 can be detected just from the emission lines corresponding to particular transitions between molecular energy states ; on the other hand, dust is less abundant but can be detected more easily since the grains scatter the light in the far-IR. Secondly, disk scale lengths are $\approx 100AU$ but their structure may be complex and, to investigate its internal details, a high-resolution instrument is required. Before direct observations, the presence of circumstellar disks was inferred from the Spectral Energy Distribution(SDE) which was very different than the one expected from a pre-main sequence star alone. Rucinski (1985) investigated 54 T-Tauri stars finding an anomalous specific flux F_λ in the near infrared, with a less steep slope than the one expected (typically $F_\lambda \propto \lambda^{-2}$) . Supplementary infrared emission was ascribable to the IR light coming from the dust of circumstellar disks. An early direct detection of protoplanetary disk comes from the *Hubble Space Telescope* (O'dell et al., 1993): figure 2.1 shows a dusty-gaseous disk covering the light coming from a T-Tauri star. The Atacama Large Millimeter and Submillimeter Array (Brown et al., 2004) represents the edge of the technology for the interferometric detection of flux in the Infrared and microwave band, reaching even an angular resolution of 0.01". Figure 2.2 shows a fascinating example of hi-res observation, in mm band, of a circumstellar disk around a T-Tauri. The picture shows the light scattered by the dust.

2.2 Circumstellar disks

2.2.1 General model of a circumstellar disk

A general model for circumstellar disks consists of a flat, azimuthally symmetric distribution of matter in a hydrodynamical equilibrium and revolving around the central forming star with a Keplerian angular velocity $\Omega_k = \sqrt{\frac{GMstar}{R^3}}$ (with respect to a cylindrical coordinates system (R, θ, z) originating on the central object and with the z-axis perpendicular to the disk rotating midplane). Assuming a short vertical aspect ratio i.e. a little ratio between the height scale and the radial extension, we can model approximately a 2D distribution of matter in which temperature T and velocity Ω_k are constant along the z direction. Fundamentally, the gas matter is concentrated in the midplane and the density and pressure fade out quickly as one moves vertically. For a fixed value of R, density and pressure vertical scale law can be easily evaluated by means of the hydrostatic equilibrium condition :

$$\frac{\partial P}{\partial z} = -\rho \frac{GM_{star}}{R^3} z \tag{2.1}$$

Provided that $T \approx cost.$ along the vertical direction, a simple equation of state can be used : $P = c_s^2 \rho$, where the sound speed c_s is constant with respect to z and depends only on the radial coordinate. Integrating the 2.1 along the z direction we

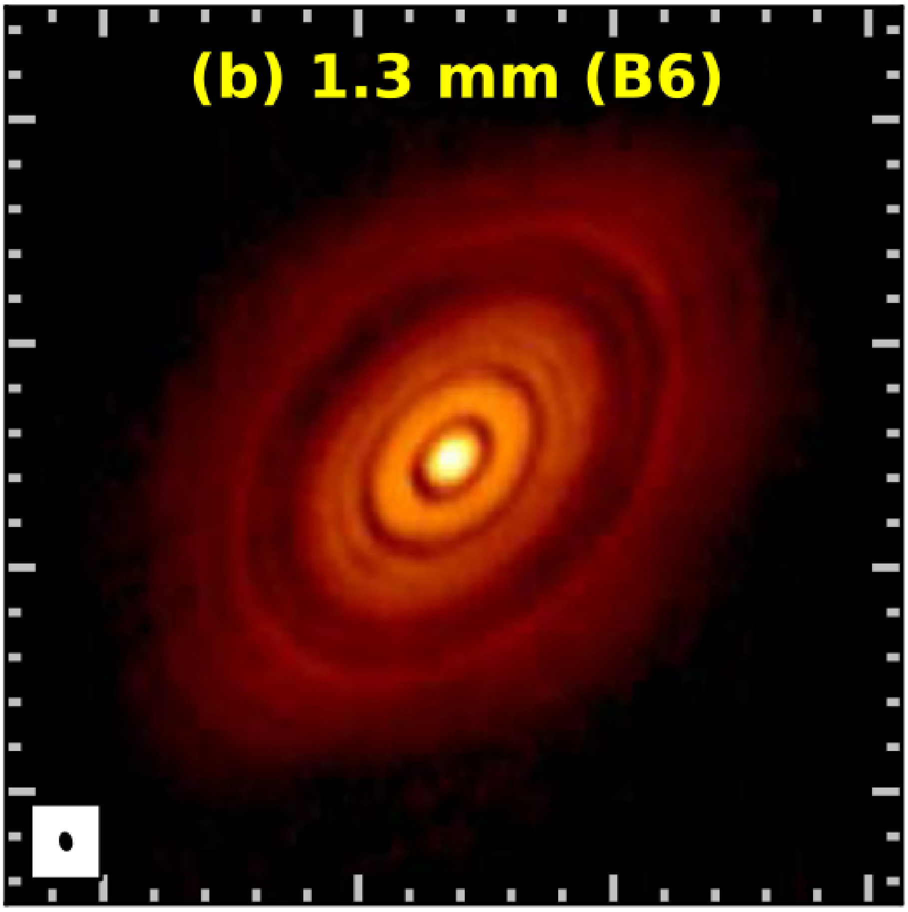

Figure 2.2. HL-Tauri protostellar disk, detected in 1.3 mm band, res. 0.1" (14 AU). (from ALMA Partnership et al., 2015, , pp. 6)

have:

$$
\begin{aligned}
d \ln P &= -\frac{1}{c_s^2} \frac{GM_{star}}{R^3} z dz \\
P(z) &= P_0 e^{-\frac{z^2}{2H^2}}
\end{aligned}
\tag{2.2}
$$

where $P(0)$ is the pressure at the midplane, while $H = c_s \left(\frac{GM_{star}}{R^3}\right)^{-1/2} = c_s \Omega_K^{-1}$ is the vertical pressure scale height. H represents the vertical lenght at which pressure and density decrease substantially and gives a measure of the disk thickness. Tipically, H is about $5\% \div 10\%$ of the radial distance from the star. The general solution for the volume density $\rho(\vec{r})$ is made of a radial term coupled indipendently with the vertical exponential term $\exp\left(-\frac{z^2}{2H^2}\right)$. By means of the 2.2, we deduce the density $\rho(R, z) = \rho_0(R) \exp(-\frac{z^2}{2H^2})$. Integrating $\rho(R, \theta, z)$ along z we would obtain:

$$\begin{aligned}\Sigma(R) &= 2\pi \int \rho(R,z)dz \\ \rho_0 &= \frac{\Sigma(R)}{\sqrt{2\pi}H}\end{aligned} \tag{2.3}$$

$\Sigma(R)$ defines the radial *Surface density*: it represents an important quantity since it is proportional to the column density of the dust one would observe if the disk was faced on with respect the line of sight. By considering a model for the Minimum Mass Solar Nebula, a disk that has just the right quantity of light elements necessary to build the actual Planetary System, at a stage in which the primordial circumsolar disk was about to be fully formed, Hayashi (1981) found a simple power law $\Sigma(R) \propto R^{-p}$ for the gas density, with $p = 3/2$:

$$\Sigma(R) = 1700 \left(\frac{R}{1\ AU}\right)^{-3/2} g\ cm^{-2} \tag{2.4}$$

with the distribution extended up to 36 AU. The dust, mainly made of rocky grains and ice, was found to follow a distribution proportional to the gas density law, with a dust-to-gas mass ratio of ≈ 0.018.

Disk thermodynamics is usually dominated by the radiative processes, hence the heating due to internal viscous processes (see below) is neglectable. Disks are in general optically thick, so in order to be thermally affected by the central star, they can receive flux from their external surface, i.e. the height z at which the mean optical path reduces to $\tau_{sup} \approx 2/3$ and the matter becomes transparent. Thus, the shape of disk surface affects substantially its thermal configuration. In considering a flat disk, hence with a ratio $\frac{H}{R} \approx cost.$, the stellar radiation hits the surface with a fixed angle of incidence, and the flux F_{rad} turns out to scale as R^{-3}. Assuming the disk surface as a black body, it will show an effective temperature $T \propto F_{rad}^{1/4} \propto R^{-3/4}$. Such a profile corresponds to Spectral Energy Distribution characteristic of accretion disks but, in the case of circumstellar matter in equilibrium, it doesn't match any usually observed spectra (see Garcia (2011), chapter 2, and Dullemond et al. (2007) for a full clarification). A better improvement is reached with flared disk models, such as the ratio $\frac{H}{R}$ increases with R. A common scheme is adopted by evaluating the effective black body temperature in the optically thin limit, such that the fraction of irradiant energy absorbed by the surface is much smaller than 1, and the midplane temperature is close to the black body temperature: $T_0 \approx T_{eff}$. It turns out that $T_0 \propto R^{-1/2}$. An improved model has been adopted by D'Alessio et al. (1999), making the assumption that the thermal processes in the inner layers of the disks don't affect its dynamical stability. No viscous heating nor cosmic rays effect has been taken into account in the energy balance equation, and the following midplane temperature profile has been obtained: $T_0 \propto R^{-3/7}$. It must be stressed that, in order to perform a realistic investigation of the thermal processes in a flared disk, a vertical isothermal profile must be improved by letting the temperature evolve and solving the radiative transport equations. Nevertheless, in geometrically thin disks the mass is concentrated in regions close to the midplane since the density decreases rapidly along the vertical direction. Thus, vertical isothermal profile represents a common schematization. In this work, we will adopt such an approach, by taking a radial profile for the midplane temperature $T_0(R) = R^{-q}$, and assuming it to be locally uniform, for all the values of z.

2.2.2 Turbulence Viscosity

A Keplerian disk in equilibrium around a star and stable with respect to the gravitational fragmentation is just in a pseudo-equilibrium state because it undergoes a secular evolution. Time evolution is driven by internal turbulence processes which contribute to dissipate kinetic energy and to transport angular momentum. Such mechanisms are intrinsically hard to be modelled and require high-level Magneto Hydrodynamical numerical integrators: weak magnetic fields are likely the main engines which trigger the turbulence giving rise to *Magnetorotational Instabilities* (some recent investigation can be found in Riols, A. et al. (2015), Hasegawa and Takeuchi (2015) ; see also Balbus and Hawley (1998), Tout (2000) for a general discussion of the relation between viscosity and magnetic field). In order to perform a simple, but realistic, numerical investigations, such issue can be partially overcome by means of a simpler approach. In practice, the whole dynamical effect given by the eddies are modeled as the disk was provided with an intrinsic viscosity ν. Such a quantity represents an effective kinematic viscosity which dissipates the macroscopical keplerian energy of the gas. An early investigation according to such scheme comes fromLynden-Bell and Pringle (1974). Let's consider the flat disk model illustrated above. Such keplerian disk has a radial differential velocity, thus, as the simple scheme in figure 2.3 shows, different layers at adjacent positions R and $R + dR$ move with different velocity and indeed they undergo different kinematic resistance. As a consequence, a couple arises, and the matter enclosed in the annulus $R, R + dR$, increase its angular momentum.

Given l the specific angular momentum, one can show that a single portion of mass δm, moving in the ring between R and $R + dR$, thanks to the couple g formed with the innermost adjacent layer, gains angular momentum according to the following law:

$$\frac{D\left(l\delta m\right)}{Dt} = -\delta m \frac{\partial g}{\partial R} \tag{2.5}$$

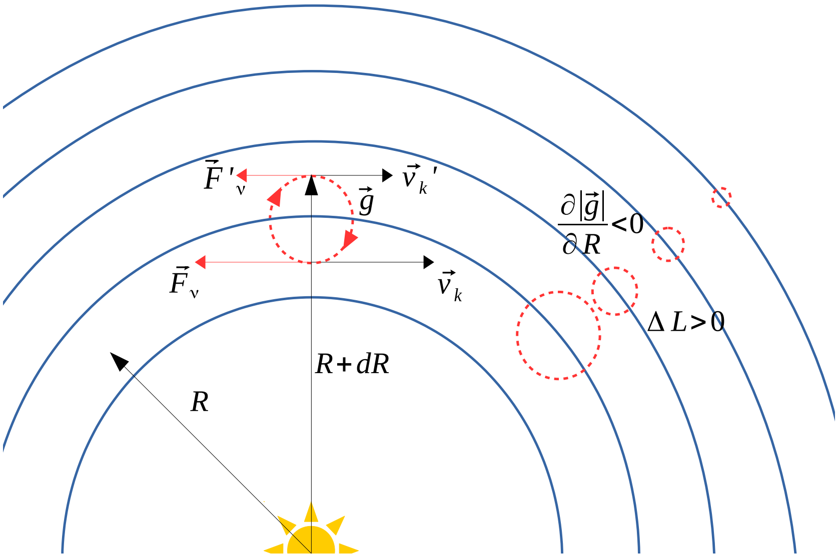

Figure 2.3. Schematic representation of the outward $\vec{L}$ transport due to viscosity. Different velocities among two adjacent rings at R and $R' = R + dR$ cause different viscous reaction $\vec{f_\nu}$ which give rise to a couple $\vec{g}$. Since $|\vec{g}|$ decreases with R, each layer gains angular momentum $l\delta m$ from its next internal ring. $l\delta m$ itself is an increasing function of R, which means that the uppermost layers gain more momentum than they lost. Thus, angular momentum moves definitely outwards, the disks enlarges its outer boundaries, while the innermost gas spirals towards the central star.

being $g = -2\pi R^3 \Sigma \frac{\partial \Omega_k}{\partial R}$. Since the differential angular rotation scales as $R^{-3/2}$, and given the common density profiles $\Sigma \propto r^{-p}$ discussed above, with $p = 3/2$ or $p = 1$, g turns out to decrease with R. As a consequence, due to the viscosity external layers inherit a larger and larger amount of $\vec{L}$ from their inner neighbour rings, giving raise to a net outward transfert of angular momentum. In principle, viscosity tends to smooth the radial gradient of velocity and thus the disk would be supposed to evolve into a rigid rotator. Actually, this scenario does not happen. In fact, in order to conserve $\vec{L}$, the matter which lies in the most external parts of the disk reacts to the gaining of l by migrating to larger orbits. On the other hand, the innermost gas particle, after losing l, migrates inwards. Thus, the keplerian differential velocity remains unchanged, and the gas accretes towards the star. Shakura and Sunyaev (in their well-known work done in 1973), formulated the so-called α-disk model. The effective viscosity in a circumstellar disk can be expressed as follows:

$$\nu = \alpha_{ss} \frac{c_s^2}{\Omega_k} = \alpha_{ss} c_s H \tag{2.6}$$

where α_{ss} represents an efficiency coefficient for the transport of momentum.

Timescales for the disk evolution can be globally estimated as:

$$\tau_\nu \approx \frac{R^2}{\nu} = \frac{R^2}{\alpha_{ss} c_s H} = \frac{1}{\alpha_{ss}\Omega_k}\left(\frac{R}{H}\right)^2 \tag{2.7}$$

Despite the intrinsic complexity of the viscous processes, several investigations have been performed in order to constrain the value of α_{ss}. The Shakura-Sunyaev coefficient is commonly modeled as constant along a disk and ranges from 10^{-4} to 10^{-1} (see for instance the works of Brandenburg et al., 1995, Mukhopadhyay, 2008). This simple framework reflects our ignorance about the deep dynamical and magnetic processes internal to the disk itself, whose numerical and theoretical schematizations still represent a hard issue. Regarding the effective viscosity ν, it may be non-uniform due to the variation of the speed of sound and the angular velocity through the disk. Given a keplerian non-selfgravitating disk around a $1M_\odot$ star, with an extension of $\approx 100AU$, with a vertical aspect ratio $H/R \approx 0.1$, we can scale $\Omega_k \approx \Omega(1AU)(R[AU])^{-3/2}yr^{-1}$. Thus, according to the 2.7, we can parametrize the typical viscosity evolution timescale, at an intermediate radial position $R = 50AU$, as $\tau_{50AU} \approx 5.63 \times 10^3 \alpha^{-1} yr$, and thus τ may range from 50×10^3yr to 50×10^6 yr.

In section 5.1 we will discuss several choices of disk configuration, for which ν can be either variable or uniform, and illustrate how such a viscosity can be easily integrated with suitable algorithms.

2.2.3 Circumstellar disks in Open Clusters

Nowadays it is well-known that star cluster host protoplanetary disks and is likely the easiest environment for the birth of planetary systems. Even the Solar System may have probably arisen in a leaky cluster constituted by no more than 1000 stars (Pfalzner, S., 2013) . The observation of Disks in Clusters have been always performed indirectly by means of detections, together with the star spectrum, of the continuum infrared radiation emitted by the dust. As an example, the *Spitzer Space Telescope* detected several circumstellar disks in the γ *Orionis Cluster*, through a combination of optical and mid-infrared techniques (Hernández et al., 2010) . Disks can be detected by analyzing the continuum-mm emission in the 887νm band, as Mann et al. (2015) reports, describing the detection of 22 disks in the NGC 2024 Cluster. The presence of such systems makes the evolution of circumbinary disks a more complex problem. Up to now, poor theoretical works have involved realistic simulations of such systems. Issues arise mainly because, typically, there is a huge difference between the characteristics time-scales of the star dynamics and the disks hydrodynamics (typical timescales are, respectively 10^6 yr and 10^3 yr). As a consequence, disks in clusters have been always treated as secondary objects.

According to the most common approaches present in literature, the dynamic of the stars is integrated by means of a gravitational N-body code, then, with some analytical models, the main effects that the trajectories of the stars may have on the shape of the disks are determined (Olczak et al., 2006, Olczak et al., 2012, Vincke, Kirsten et al., 2015, Bhandare, Asmita et al., 2016). For such reasons, the evolution of circumstellar disks represents still an unresolved field, whose issues should be approached with direct hydrodynamical simulations.

Chapter 3

A new SPH algorithm for the evolution of self-gravitating systems

In this chapter, we will discuss the main characteristics of a new TREE-based Smoothed Particle Hydrodynamics (SPH) code we developed to investigate the evolution of self-gravitating systems. The algorithm is able to integrate the time evolution of a distribution of gas, with the possibility to add a few point-mass objects which contribute just with their gravitational field. The latter, provided with suitable sink radius and softening radius for the gravitational field, may represent both planets or stars.

Starting with a short introduction to the basic theoretical formulation of Tree Codes and the Smoothed Particle Hydrodynamics (hereafter SPH) formalism, we'll discuss the implementation of such technique inside the algorithm.

3.1 Basic structure of the algorithm

The general scheme of the code is illustrated by the diagram in figure 3.1. A system composed of N lagrangian points is set up to represent a physical medium and it is let evolve by the numerical integration of the equations of motion. Three kinds of physical systems are allowed to be studied: selfgravitating gas, non-selfgravitating gas, and collisionless self-gravitating non-gaseous systems. In the first two systems, at each time-step, the calculation requires two preliminary cycles: one to evaluate the thermodynamical variables (such as density, pressure, and Temperature) with the SPH schematization, another for the estimation of the hydrodynamical interactions i.e. pressure gradient and internal energy variation (details are explained in section 3.2). If the gas is self-gravitating, i.e. its self-potential is not negligible in comparison with its thermo-kinetic energy, the Newtonian interactions are evaluated with a tree scheme approximation (as explained in the next section), at the same time as the pressure gradient. The third case is performed by switching off the hydrodynamical routines and treating the particles as mere point-masses interacting with a Newtonian field approximated with the same tree-scheme mentioned above.

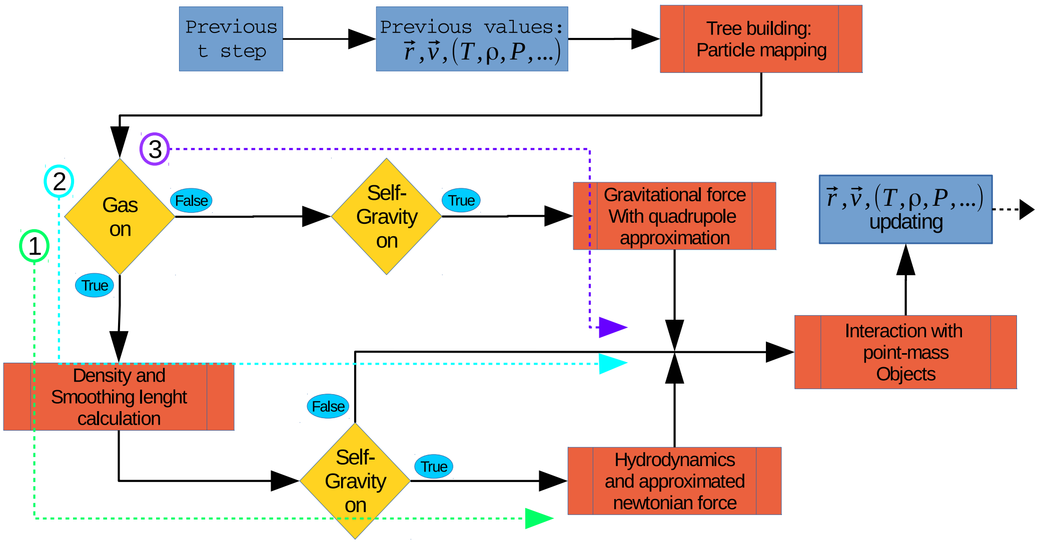

Figure 3.1. The general scheme of the code, for a single time-step. Each iteration, a set of N particles are mapped in a grid; the accelerations may be evaluated in three different ways. (1) self-gravitating gas: a preliminary routine evaluates the density and pressure according to SPH scheme, a second routine calculates the pressure gradient and the Newtonian field following an SPH plus tree scheme. (2) Non-selfgravitating gas: the same as (1) but neglecting the Newtonian field. (3) Since we are dealing with a non-gas system, there is only the routine for the evaluation of the gravitational forces. A final routine deals with additional N' objects(stars or planets). The Newtonian interactions of the N particles in all the three cases are approximated with a tree scheme, while the N' additional objects interact directly with the system, approximations.

In every case, before the force calculations, particles are requested to be mapped in a grid, in order to locate efficiently both the nearest neighbors and the farther points. Thus, every timestep a preliminary phase is dedicated to mapping the points. Eventually, if additional few objects are considered (such as stars or planets), their contribution to the system is taken into account by means of a direct point-to-point interaction, without any approximation.

3.2 Tree-scheme algorithm for the self-gravity

The gravitational field in a Lagrangian approach is treated by setting a system of N particles. Particles may interact either at short or at long distances. Thus, in a classical direct N body code, the Newtonian equations of motion are integrated by considering all the mutual interactions and number of operations $\propto N^2$ is required (a general treatment can be found in Spurzem (1999)). Conversely, gravitational TREE codes allow to evaluate the Newtonian field by making some approximations in such a way that, for a generic particle, only the contribution given by closer points is calculated correctly by a direct *particle-particle* coupling. On the other hand, far particles are collected in large clusters with a global mass, and particles interact with them just with a single *particle-cluster* coupling. The net amount of calculus per time iteration then can be shown to scale as $N \log N$ (Hernquist, 1987) , and thus turns to be neglectable in comparison with N^2, for sufficiently great N .
The scheme we are going to describe in this section takes the basic principles of the gravitational *Tree-Code* developed for the first time by (Barnes, 1986)(see also Barnes and Hut, 1986, Hernquist, 1987, Warren and Salmon, 1992).

3.2.1 Fundamental theory: multipolar expansion of the potential field

The Tree-scheme approximation exploits the multipolar expansion of the gravitational field generated by a distribution of matter enclosed in a finite volume with a characteristic extension length R. We are interested in finding an approximated expression of the gravitational potential $\Phi(x, y, z)$, at distances $r = |\vec{r}| >> R$ (the reference system corresponds to the center of mass frame). Details on multipolar field approximation formalism can be found in Binney and Tremaine (1987), chap. 2, and Hernquist (1987). Starting with the Poisson equation $\vec{\nabla}^2\Phi = 4\pi G\rho$ and expressing it in spherical coordinates (r, θ, ϕ), we can expand the potential solution $\Phi(r, \theta, \phi)$ for $r >> R$:

$$\Phi(r, \theta, \phi) = -4\pi G \sum_{l,m} \frac{Y_{lm}(\theta, \phi)}{(2l+1)\ r^{l+1}} \cdot \int Y^*_{lm}(\theta', \phi')\ r'^{l}\ \rho(\vec{r'})\ d^3\vec{r'} \tag{3.1}$$

where Y_{lm} and Y^*_{lm} are the generic spherical harmonics functions and its complex conjugate, characterized by a multipole order l and an angular number m ; and $d^3\vec{r'}$ represents the infinitesimal volume element of integration $r'^2 sin\theta' dr' d\theta' d\phi'$. For sufficiently large r we can arrest our expansion to the dipole term (for l=2) and sum all over the possible values of m. Switching to cartesian coordinates we then obtain :

$$\Phi(\vec{r}) = -\frac{GM}{r} - \frac{\vec{p}\cdot\vec{r}}{r^3} - \frac{1}{2}\frac{G}{r^5}\vec{r}\bar{\bar{Q}}\vec{r} \tag{3.2}$$

in which we can recognize the first monopole term which is the exact value the potential would have if the whole mass M of the distribution was concentrated in a single point. The second term contains the dipole moment $\vec{p} = \int \vec{r'}\rho\vec{r'}d^3\vec{r'}$ which is null in the center of mass frame. In the last term we find the quantity $\vec{r}\bar{\bar{Q}}\vec{r} \equiv \sum\limits_{i,j} Q_{ij}\ x_i x_j$, where $\bar{\bar{Q}}$ represents the traceless *quadrupole moment tensor*, defined as :

$$Q_{ij} = \int \left(3x_i'x_j' - r'^2\delta_{ij}\right)\rho(\vec{r'})d^3\vec{r'} \tag{3.3}$$

while x_i, x_j are two generic cartesian coordinates x,y,z. Besides the monopole term, the quadrupole moment introduces a significant perturbation which depends on the shape of the mass distribution through the radial coordinate only. Once we are able to evaluate $\bar{\bar{Q}}$, we are then able to write an approximated expression of $\Phi(r)$ for large distances r. In an N body simulation, in place of a continuous distribution, we have a discrete ensemble of particles (a *cluster*), so the quadrupole momentum is discretized:

$$Q_{ij} = \sum_k \left(3x_{ik}'x_{jk}' - r_k'^2\delta_{ij}\right)m_k \tag{3.4}$$

where m_k is the mass of the particle. It is straightforward to obtain the expression of the acceleration field generated by the cluster: $\vec{a}(\vec{r}) = -\vec{\nabla}\Phi(\vec{r})$. Thus, finally we have :

$$\Phi(\vec{r}) = -\frac{GM}{r} - \frac{1}{2}\frac{G\ \vec{r}\bar{\bar{Q}}\vec{r}}{r^5} \tag{3.5a}$$

$$\vec{a}(\vec{r}) = -\frac{GM}{r^3}\cdot\vec{r} + \frac{G\bar{\bar{Q}}\cdot\vec{r}}{r^5}\cdot\vec{r} - \frac{5}{2}\frac{G\ \vec{r}\bar{\bar{Q}}\vec{r}}{r^7}\cdot\vec{r} \tag{3.5b}$$

The main task of a tree scheme consists in classifying the particles in clusters and keeping in memory the main parameters (center of mass $\vec{r}_C$, total mass M and their total Q tensor). Once we realize that a particle is far enough from a cluster, we evaluate once their mutual forces, by means of 3.5b.

3.2.2 Implementing the scheme

A tree algorithm uses an easy and efficient approach to this problem. As shown in figure 3.2, a 3-Dimensional integration domain is enclosed in a D-sided cube, called the *Root Box*. Starting from this base, we apply a recursively octal-based subdivision: the root box is thus decomposed in eight $\frac{D}{2}$-sided cubes; conventionally we consider it as L=1 order partition. Further orders of subdivision (L=2, L=3, L=4 and so forth...) generate subgrids of cubes having side $D_L = D \cdot 2^{-L}$.

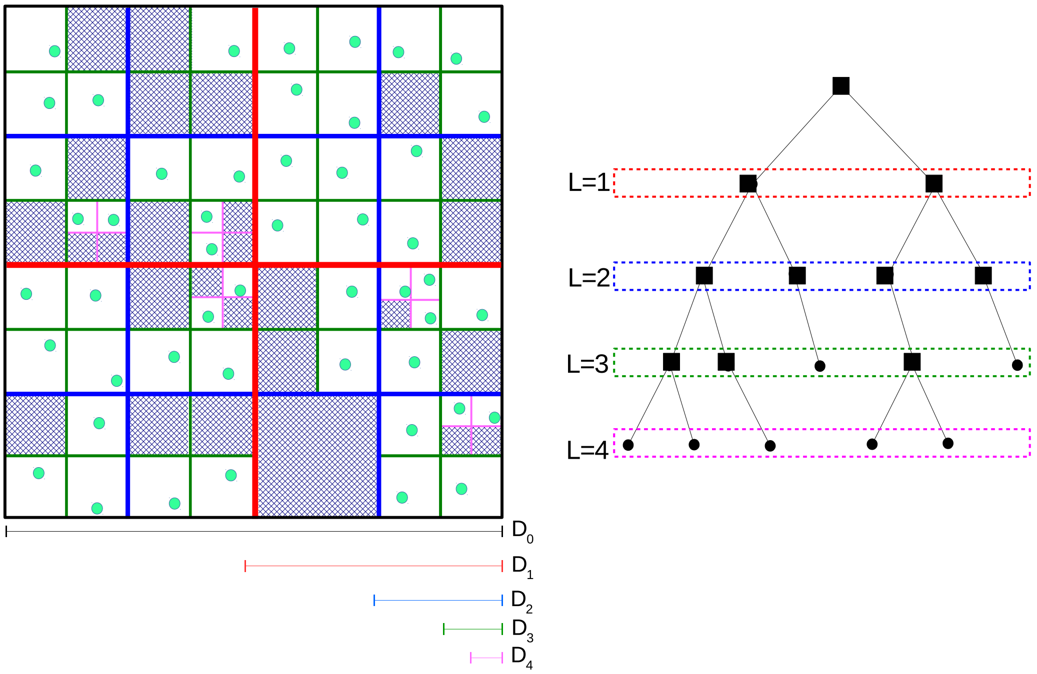

Figure 3.2. Representation of the particle mapping with a tree code. Left diagram: simplified 2D representation of the octal domain decomposition. The root box of length D is further subdivided into sub-boxes until each of them contains just one particle. Grey-filled cells represent void boxes. Right diagram: tree structure; every box is connected with its sub-boxes. During the force calculation, each particle walks through the tree, starting from the top level L=0, until the terminal boxes (black dots) are reached.

While proceeding with the domain decomposition, we have a set of shorter and shorter cubes containing fewer and fewer particles. The partition arrests when a cube contains just one particle (*terminal cube*), void boxes are ignored. The global octal subdivision ends when all cubes are terminal cubes, and the algorithm is thus stopped. For each order L, non-void cubes are identified as clusters, the particles contained are recognized and center of mass $\vec{r}_C$, M and $\bar{\bar{Q}}$ are calculated. We have thus obtained a Tree-structure which starts from the root level L=0 and expands his arms towards higher L levels. Each branch-node represents a cube-cluster and it's connected with its sub-boxes, while the "leaves" represent the terminal cubes. Once the tree is built, the algorithm begins to evaluate the accelerations: each i-th particle is made interact with all the cubes by descending the tree untill it reaches the leaves. Starting from the order L=1, the distance $r \equiv |\vec{r_i} - \vec{r}_C|$ about the center of mass of each box is evaluated and compared with the side D_1. A cube-cluster is considered "far enough", to apply the quadrupole approximation, only if the so-called *Opening Criterium* is satisfied:

$$\frac{D_1}{r} < \theta \tag{3.6}$$

where θ represents a constant tolerance parameter called *Opening Angle* (typical values are $0.6 \div 1$). Equation 3.6 means that the Newtonian field generated by a cluster can be approximated only for distances larger than the order of the scale length D_1 of the cluster itself. In such case, we can update the acceleration $\vec{a}_i$ using 3.5b, neglecting all the particles internal to the box. On the contrary, if a cube does not satisfy the opening criterium, it will be opened and its internal cubes will be checked. The particle thus descends the tree moving towards order L=2 cubes and the algorithm compares again the mutual distance r with the side D_2. Again, whenever the opening criterium is satisfied, i.e. $\frac{D_2}{r} < \theta$, acceleration $\vec{a}_i$ is updated in quadrupole approximation, otherwise the boxes are further opened. The descent of the tree keeps on until the terminal boxes reached, in such case, the particle i makes a direct point-to-point interaction with the single particles contained.

In order to build the tree, we need an efficient way to map the points into the octal grid space, we do it by following a prescription adopted by Miocchi and Capuzzo-Dolcetta (2002) (see also Capuzzo-Dolcetta and Miocchi, 1998). Given a nonvoid cube of order L, the position of each particle contained is codified through a group of 3 bits corresponding to an 8-based number. The bits are straightforwardly associated to one of the eight (L+1)-order sub-cubes enclosed. In practice, to map a point we start from the root box L=0, we identify the 1st order sub-box where particle lies by establishing whether its coordinates x,y,z are higher or shorter than the respective coordinates of the root box center. In case a coordinate is higher, we set a related binary number to 1, otherwise, we set it to 0. From this latter sub-box, a further sequence of 3 bits identifies the 2nd order sub-box in which the particle is enclosed (and so forth). Such these bit sequences form a series which is easily stored in memory in such a way the program is able to know anytime straightforwardly whether a particle belongs or not to a certain box-cluster.

3.3 The lagrangian SPH approach for a gas system

3.3.1 Implementation of the basic Smoothed Particle Hydrodynamics scheme

Since their first applications performed by Lucy (1977) , and Gingold and Monaghan (1977), SPH algorithms have been used for a wide class of Astronomical problems involving fluid systems. Given an ideal (or viscous) fluid, SPH allows integrating the governing Eulerian equations(or, respectively, the Navier Stokes Equations) in a Lagrangian approach by schematizing the system with a set of moving particles. For an exhaustive explanation we remind the following references Monaghan and Lattanzio (1985), Monaghan (1988, 1992, 2005), Cossins (2010). Each particle represents the state of the fluid at a certain point, and its position evolves with time depending on the velocity field $\vec{v}(\vec{r}, t)$ of the fluid. Given a particle at a position $\vec{r_i}$, SPH allows to interpolate a generic quantity A_i (which may represent $\vec{v}(\vec{r_i}, t), T(\vec{r_i}, t), \rho(\vec{r_i}, t), P(\vec{r_i}, t)...$), and its further derivatives $\vec{\nabla} A_i$ and $\nabla^2 A_i$, over a set of particles lying within a limited extended neighbourhood. we can write:

$$A_i = \sum_j m_j A_j W\left(r_{ij}, h)\right) \tag{3.7a}$$

$$\vec{\nabla}_i A_i = \sum_j m_j A_j \vec{\nabla}_i W\left(r_{ij}, h)\right) \tag{3.7b}$$

where the mass m_j and A_j refer to a generic neighbour particle at the position $\vec{r_j}$, while $\vec{\nabla}_i \equiv (\frac{\partial}{\partial x_i}, \frac{\partial}{\partial y_i}, \frac{\partial}{\partial z_i})$ is the gradient operator with respect to the system frame of particle i. The summation domain is determined by the so called *Interpolation (or smoothing) Kernel* W: a suitable weighting function which depends just on the mutual distance $r_{ij} \equiv |\vec{r_i} - \vec{r_j}|$ and spreads over a finite radial extension proportional to the *Smoothing Lenght h.* So, for example, we can interpolate density ρ_i :

$$\rho_i = \sum_j m_j \cdot W(r_{ij}, h) \tag{3.8}$$

Following the SPH formalism, we can also interpolate the gradients of ρ and $\vec{v}$ with expressions in function of the gradient of W, we are then allowed to write an expression of the continuity equation for the generic particle i :

$$\frac{d\rho_i}{dt} = \sum_j m_j \; \vec{v}_{ij} \cdot \vec{\nabla}_i W(r_{ij}, h) \tag{3.9}$$

where $\vec{v}_{ij} \equiv \vec{v}_i - \vec{v}_j$ is the differential velocity vector; hereafter we will use A_{ij} referring to the generic variable $A_i - A_j$.
Kernel W is a radial, normalized and continuous distribution with continuous derivatives. The smoothing length h represents its radial spread. It can be easily shown (see for example Hernquist and Katz, 1989) that such these properties guarantee interpolating errors limited to the order of h^2 . In the early stages of SPH implementation, Gaussian-like kernels were used, here is an example:

$$W_{gauss}(r_{ij}, h) = \frac{1}{(\sqrt{\pi} h)^d} \cdot \exp(-q^2) \tag{3.10}$$

where q represent the ratio r_{ij}/h and d is the dimension number of the problem. However, functions with compact support are preferred. In our code, we use the so-called Cubic Spline function (introduced for the first time by Monaghan and Lattanzio, 1985), whose expression is reported below :

$$W_{3spline}(r_{ij}, h) = \frac{1}{\pi h^3} \begin{cases} 1 - \frac{3}{2}q^2 + \frac{3}{4}q^3 & , \text{ if } \quad 0 \leq q < 1 \\ \frac{1}{4}\left[2 - q\right]^3 & , \text{ if } \quad 1 \leq q \leq 2 \\ 0 & , \text{ if } \quad q > 2 \end{cases} \tag{3.11}$$

The function is normalized and radial and the limited extension of its support to $r_{ij} = 2h$ guarantees a satisfying interpolation (with errors scaling as $O(h^2)$) involving just a set of limited neighbor particles without introducing further error. Indeed, to reach a good efficiency, the interpolation should be always done by choosing a limited neighborhood. Unfortunately, the Gaussian kernels have infinite support, and thus a cutoff is needed. But, whatever cut-off radius is chosen, the Gaussian kernel and its derivatives are not null: this produces an additional noise associated with the bordering particles.

Equation 3.9 can be integrated in time and used in place of 3.8 to find the density, provided that a starting explicit value $\rho_i(t = 0)$ is given. On the contrary, we prefer to use directly the 3.8 calculating ρ from the particles positions. In the SPH scheme, the spatial distribution of particles marks the actual shape of the fluid. To perform a good interpolation, we need a sufficient number $N'$of neighbor particles, in a 3D problem, the number is $\approx 50 \div 60$ (see Monaghan, 1985). When we treat homogeneous fluids, such condition is easily satisfied provided we hose a constant value of h sufficiently large. Conversely, when there are huge gradients of density and/or we are in a non-stationary regime, the distribution of particles is not uniform, nor constant. In order to keep a sufficient N' for all the points, we must use a smoothing length h$\equiv h(\vec{r}, t)$ variable in space and time. Every particle must have its own h_i in such a way that the more the number density n_i, the less the interpolation kernel radius :

$$h_i = \delta \left(\frac{m_i}{\rho_i} \right)^{1/3} \propto n_i^{-1/3} \tag{3.12}$$

typically with the constant $\delta \in [1.2, 1.5]$. For such purpose, we use the following classical prescription (see for example Hernquist and Katz (1989), or Monaghan (2005)). For each particle, we start from an initial guess of h, and update it recursively until the number N' reaches an ideal value N_n fixed a priori. In practice, we start with an initial guess $h_{prev} = h_0$ and iterate a loop: each iteration the number of neighbor points is counted using h_{prev}, then we update the latter to a new value h_{new} according to the following formula:

$$h_{new} = h_{prev} \cdot \frac{1}{2} \left[1 + \left(\frac{N_0}{N'} \right)^{1/3} \right] \tag{3.13}$$

If the fluid was homogeneous, $h_{prev} \cdot (N_n/N')^{1/3}$ would provide immediately the correct value of smoothing length, without any further iteration. The added 1 lets the program perform an average with the old smoothing length, damping any excessive oscillation error due to inhomogeneities in the spatial distribution of particles. The iteration is stopped when a convergence is reached according to the criterium: $|N' - N_n| \leq M$, where M is a tolerance number, typically $M \geq 10$. Attwood, R. E. et al. (2007) investigated the acoustic oscillations of a gas polytrope around the equilibrium, by imposing a constant neighbor number N' and letting M vary. They found that the fluctuation of $N' \pm M$ introduced an additional numerical noise which broke the stability, giving rise to errors. As a result, the energy of the fundamental mode of oscillation was dissipated incorrectly and the kinetic energy was transferred to higher order modes. To prevent errors, a value of $M = 0$ should be chosen. It can be shown that the choice of h according to the criterium $N' \pm 0$ is statistically equivalent to solve, for all the particles, the $2N$-equations system described by 3.8 plus 3.12 and find the exact solutions of ρ_i and h_i, with $\delta \approx 0.31\ N^{1/3}$.

SPH formalism allows us also to evaluate the Pressure gradient $\vec{\nabla}_i P$ and thus to obtain straightforwardly an expression for the Lagrangian equation of fluid motion. Our investigations don't involve the molecular viscosity, hence we use the Eulerian equation:

$$\frac{d\vec{v}_i}{dt} = -\sum_j m_j \left(\frac{P_i}{\rho_i^2} + \frac{P_j}{\rho_j^2} \right) \cdot \vec{\nabla}_i W'(r_{ij}, h) \tag{3.14}$$

Without dissipations, we use the differential of the specific internal energy

$du = P\rho^{-2}d\rho$ to obtain an equation for the internal energy:

$$\frac{du_i}{dt} = \sum_j m_j \left(\frac{P_i}{\rho_i^2} + \frac{P_j}{\rho_j^2} \right) \vec{v}_{ij} \cdot \vec{\nabla}_i W'(r_{ij}, h) \tag{3.15}$$

In both 3.14 and 3.15 we use a particular form of the interpolation kernel $W'(r_{ij}, h) = \frac{1}{2}\left[W(r_{ij}, h_i) + W(r_{ij}, h_j)\right]$, to guarantee the symmetry of the Eulerian equations with respect to the exchange of particles i<—>j. 3.14 and 3.15 prevent the non conservation of linear and angular momentum due whether to density and pressure inhomogenities, or to space variation of Smoothing Lenght. It is straightforward to show that the rate of total amount of cinetic energy lost by the fluid, evaluated by summing $\sum_{i=1}^{N} m_i \vec{v}_i \frac{d\vec{v}_i}{dt}$, is equal to the total rate of thermal energy $\sum_{i=1}^{N} m_i \frac{du_i}{dt}$ gained by the fluid itself. Similarly, we have a conservation of the angular momentum(see Monaghan, 1989).

To close the system, a perfect gas needs the following adiabatic equation of state:

$$P_i = (\gamma - 1)\ \rho_i\ u_i \tag{3.16}$$

As mentioned in section 2.2, our peculiar investigation involves isothermal radial profiles for the protoplanetary disks, thus, we will use an equation of state containing an isothermal speed of sound:

$$P_i = \left(\frac{K_b}{m_\mu} T_i \right) \rho_i = c_{s\,i}^2 \rho_i \tag{3.17}$$

Finally, the particles positions depend directly from the velocity field:

$$\vec{r}_i = \frac{d\vec{v}_i}{dt} \tag{3.18}$$

3.3.2 Artificial viscosity

In high compression regions, such as shock wavefronts, two layers may interpenetrate generating unphysical effects. Additional artificial pressure terms are hence needed to evaluate correctly the particle motion. The origin of such issues is related to the physical mechanism of the shock waves. Actually, a shock wave front causes non-isoentropic variations of energy that standard equations 3.14 and 3.15 cannot handle. From a numerical point of view, in regions with a high $\vec{\nabla} \cdot \vec{v}$, the velocity field may be very irregular even among close particles. The errors in the evaluation of $\vec{v}$ may be amplified and numerical noises can arise, affecting the calculations of the particles positions and leading to a non-realistic overlap of two portions of fluid. Furthermore, the microscopical scale-lengths involved in a shock front are usually so short, in comparison with the smoothing scale h, that SPH resolution wouldn't allow us to reproduce them in details. In practice, a good solution adopted in literature is given by the introduction of a non-adiabatic artificial force term which, acting like a viscosity, damps the $\vec{v}$-noise. The kinetic energy lost is converted into thermal energy, emulating the physical effects of shock waves without dealing directly with the Rankine-Hugoniot equations. Early attempts to face this problem consisted in integrating the pressure with some damping terms proportional to $\vec{\nabla} \cdot \vec{v}$ and to $\left(\vec{\nabla} \cdot \vec{v}\right)^2$ (see Monaghan and Gingold, 1983, Nelson et al., 2000, for detailed references), without positive outcomes. In our code, we added an artificial term adopted the classical schematization of Monaghan (1989), who improved the previous formulations by introducing a conservative suitable *artificial viscosity* aimed at damping the velocities when the particles get close. With these prescriptions, the Eulerian equations assume the following expressions:

$$\frac{d\vec{v}_i}{dt} = -\sum_j m_j \left(\frac{P_i}{\rho_i^2} + \frac{P_j}{\rho_j^2} + \Pi_{ij}\right) \cdot \vec{\nabla}_i W'(r_{ij}, h) \tag{3.19}$$

$$\frac{du_i}{dt} = \sum_j m_j \left(\frac{P_i}{\rho_i^2} + \frac{P_j}{\rho_j^2} + \Pi_{ij}\right) \; \vec{v}_{ij} \cdot \vec{\nabla}_i W'(r_{ij}, h) \tag{3.20}$$

where a new viscous pressure term Π_{ij} has been introduced:

$$\Pi_{ij} = \begin{cases} \dfrac{-\alpha \bar{c} \mu_{ij} + \beta \mu_{ij}^2}{\bar{\rho_{ij}}} & , \text{ if } \quad \vec{v_{ij}} \cdot \vec{r_{ij}} < 0 \\ 0 & , \text{ if } \quad \vec{v_{ij}} \cdot \vec{r_{ij}} > 0 \end{cases} \tag{3.21}$$

$\mu_{ij} = \dfrac{h \vec{v_{ij}} \cdot \vec{r_{ij}}}{\vec{r_{ij}^2} + \eta^2 \bar{h}^2}$ is related to the velocity divergence between two particles, such as the quantity $\mu_{ij} \frac{m_i}{\rho_i}$ represents the infinitesimal local extimation of the velocity divergence and thus $\left(\vec{\nabla} \cdot \vec{v}\right)_i = \sum\limits_j \mu_{ij} \frac{m_i}{\rho_j}$. η is a suitable term to prevent singularities when particles get very close (we use a typical value of 0.1) while $\bar{h}$, $\bar{\rho}$ and $\bar{c}$ represent the average values $\frac{1}{2}(h_i + h_j)$, $\frac{1}{2}(\rho_i + \rho_j)$ and $\frac{1}{2}(c_i + c_j)$. Π_{ij} gives two main contributions. α is the so called *bulk* viscosity and is responsible to damp the unphisical velocity oscillations contributing with a net diffusive effect, while $\beta = 2\alpha$ is the *Von Neuman-Richtmyer* viscosity which contributes with a pressure term proportional to $\left(\vec{\nabla} \cdot \vec{v}\right)^2$. Since the Π_{ij} is symmetric, two particles exchange exactly two vector forces equal and opposite and thus equations 3.19 and 3.20, guarantee the conservation of total energy, linear momentum and angular momentum.

In this simple formulation, the artificial viscosity is activated all over the fluid;

nevertheless, there are two circumstances in which it should be switched off to prevent unphysical effects. Viscosity must be softened both in regions where shear dominates, and where $\vec{\nabla} \cdot \vec{v}$ is low. In a pure shear regime, the layers of a fluid shift longitudinally, along with $\vec{v}$, without causing any fluid compression. In terms of math, the velocity curl dominates over the velocity divergence. Nonetheless, if two of these layers moved at different velocities, two respective SPH particles i and j would get closer, hence the divergence term μ_{ij} would not vanish (as it would be expected in non-compressive fluids). As a result, we'd have a false compression and thus an unnecessary dissipation of kinetic energy. To overcome this problem, we multiply the viscosity term μ_{ij} by the switching coefficient introduced by Balsara (1995), and defined as follows:

$$f = \frac{|\vec{\nabla} \cdot \vec{v}|}{|\vec{\nabla} \cdot \vec{v}| + |\vec{\nabla} \times \vec{v}| + 10^{-4}\left(c_s h^{-1} + \omega_m\right)} \tag{3.22}$$

where we find a small perturbation proportional to c_s/h, useful to prevent singularities when particles are too close or there is a too low difference in velocities. Generally, such term may not work usefully in very inhomogeneous systems like circumstellar disks, where we may have a too low sound speed or too large h when gas is rarefied. Thus, unless we don't use lower and upper limits for c_s and h, we add the term $\omega_m = \sqrt{\frac{Gm}{h^3}} \propto \sqrt{G\rho}$ which depends on the particle mass. Balsara's switch is commonly applied in a symmetric form. First, for each particle i we interpolate the v-divergence and the v-curl :

$$\begin{cases} \left(\vec{\nabla} \cdot \vec{v}\right)_i = \rho_i^{-1} \sum\limits_j m_j \; \vec{v}_{ij} \cdot \vec{\nabla}_i W(r, h_i) \\ \left(\vec{\nabla} \times \vec{v}\right)_i = \rho_i^{-1} \sum\limits_j m_j \; \vec{v}_{ij} \times \vec{\nabla}_i W(r, h_i) \end{cases} \tag{3.23}$$

then, for each couple $i <-> j$ we multiply μ_{ij} for the average value $f_{ij} = \frac{1}{2}\left(f_i + f_j\right)$. Even though we are not in a shear regime, some problems may arise when we are far from high compression regions. In the classical formulation of Π_{ij}, α is a constant term, whose ideal value is 1. In such scheme, the viscosity acts in every region with the same effectiveness, while we would expect the artificial term to be efficient just where it is needed, i.e. close to the shock fronts. We need hence, for every particle, an individual α_i which varies with time, too. Morris and Monaghan (1997) added the following equation for the time variation of α:

$$\frac{d\alpha_i}{dt} = -\frac{(\alpha_i - \alpha_{min})}{\tau_\alpha} + S_i \tag{3.24}$$

where $S_i = \max(-(\vec{\nabla} \cdot \vec{v})_i, 0)$ represents a source term, it increases with the proximity to the shock fronts; α_{min} represents the minimum value of α. The 3.24 tells us that, starting from an initial α_0 between α_{min} and 1, the bulk viscosity approaches 1 when the divergence of the velocity is strong, while it decays to α_{min} in weak compression regime. $\tau_\alpha = \frac{h}{bc_s}$ (with $b < 1$) defines the time-scale of adjustement for α. It means that, once the fluid undergoes a compression, the viscosity changes value in a reaction time greater than the propagation of the informations (i.e. the sound waves) in the fluid over a resolution lenght h. It has been found that for very strong shock, even $\alpha > 1$ would be required; in our code we used a slightly modified prescription of Rosswog et al. (2000), who renormalized the source term to $S_i = \max(-(\vec{\nabla} \cdot \vec{v})_i, 0)(\alpha_{max} - \alpha_{min})$. In their investigation on merging of neutron stars, Rosswog et al. (2000) used $\alpha_{max} = 1.5$, $\alpha_{min} = 0.05$ and $b^{-1} = 5$. In the next chapter we will show how in a shock problem α can reach values even greater than 1.5; we use $\alpha_{max} = 2$, $\alpha_{min} = 0.1$ and $b^{-1} = 5$. These are the most common values adopted in literature to face a wide class of problems involving collapse, stars merging or protoplanetary disks (see, for instance, Rosswog and Price, 2007, Stamatellos et al., 2011, Hosono et al., 2016)

3.3.3 The Hamiltonian approach

When we are dealing with irregular systems, a variable smoothing length leads to a nonpysical evolution. Hernquist (1993) made a series of tests investigating the collision of two polytrophic systems and found that, even though a satisfying conservation of energy was reached, the SPH equations illustrated above didn't guarantee a good conservation of entropy, as was expected for particles far from the shocks. Such issue can be ascribed to the systematic update of h during the time integration. Writing, for each particle, an entropy function $A_i(s) = P\rho^{-\gamma}$, it can be shown that its time variation is not null when h is variable:

$$\frac{dA_i(s)}{dt} \propto \sum_j m_j \frac{\partial W}{\partial h_j} \frac{\partial h_j}{\partial t} \neq 0 \tag{3.25}$$

To overcome this problem, Springel and Hernquist (2002) derived a new form for the SPH relations directly from the *Euler-Lagrange equations*, in order to keep constant the total energy of the system. We can characterize a system of N SPH particles with $2N$ independent variables $(q_1...q_{2N}) \equiv (|\vec{r}_1|...|\vec{r}_N|, h_1...h_N)$: its lagrangian is $L = \frac{1}{2}\sum_{i=1}^{N} m_i|\vec{q}|^2 - \sum_i m_i u_i$. The condition on keeping constant the number N' of neighbours implies N constraint functions $\Phi_i(\vec{q}_i)$:

$$\frac{4\pi}{3}(2h_i)^3\rho_i = N'm_i \quad \rightarrow \quad \Phi_i(q) = \frac{4\pi}{3}(2h_i)^3\rho_i - N'm_i = 0 \tag{3.26}$$

Thus, by means of the Lagrange multipliers, we can build the function $L' = L + \sum_i \lambda_i \Phi_i(q)$ to which we apply the Euler-Lagrange equations to find the correct laws which minimize the action. Thus, for every particle i, we have the following two equations:

$$\frac{d}{dt}\frac{\partial L}{\partial \dot{r}_i} - \frac{\partial L}{\partial r_i} = \sum_{k=1}^{N} \lambda_k \frac{\partial \Phi_k}{\partial r_i} \tag{3.27a}$$

$$\frac{d}{dt}\frac{\partial L}{\partial \dot{h}_i} - \frac{\partial L}{\partial h_i} = \sum_{k=1}^{N} \lambda_k \frac{\partial \Phi_k}{\partial h_i} \tag{3.27b}$$

using the 3.27b to find λ_i, and substituting in the 3.27a we can obtain the equation of motion:

$$\begin{gathered}\frac{d\vec{v}_i}{dt} = -\sum_{j=1}^{N} m_j \left[\frac{P_i}{\rho_i^2 \Omega_i} \vec{\nabla}_i W_{ij}(r_{ij}, h_i) + \frac{P_j}{\rho_j^2 \Omega_j} \vec{\nabla}_i W_{ij}(r_{ij}, h_j) \right] \\ \Omega_i = 1 + \frac{h_i}{3\rho_i} \sum_j m_j \frac{\partial W_{ij}(h_i)}{\partial h_i}\end{gathered} \tag{3.28}$$

which is very similar to 3.14 apart the correction terms Ω_i which take into account the time-variation of h. 3.28 represents a realistic equation of motion, since it comes directly from the Lagrangian equations and indeed minimizes the action $\int L\ dt$. With the same formalism, a similar form of the equation of energy can be obtained, too. Let's calculate the Lagrangian time derivative $\frac{d\rho}{dt}$ by deriving the 3.8. By means of simple manipulations, it is straightforward to obtain:

$$\frac{d\rho_i}{dt} = \sum_j m_j \frac{\partial W_{ij}(h_i)}{\partial r_{ij}} \left(\frac{\partial r_{ij}}{\partial r_i} v_i + \frac{\partial r_{ij}}{\partial r_j} v_j \right) + \sum_j m_j \sum_k \frac{\partial W_{ij}(h_i)}{\partial h_k} \frac{\partial h_k}{\partial t}$$

and, rewriting $\frac{\partial h_k}{\partial t} = \sum_q \frac{\partial h_k}{\partial \rho_q} \frac{d\rho_q}{dt}$, and considering that $\frac{\partial r_{ij}}{\partial r_j} = -\frac{\partial r_{ij}}{\partial r_i}$, we obtain the correct expression for the continuity equation, very similar to the 3.9:

$$\frac{d\rho_i}{dt} = \frac{1}{\Omega_i} \sum_j m_j \vec{v_{ij}} \cdot \vec{\nabla}_i W_{ij}(h_i) \tag{3.29}$$

Now, as done for the 3.15, we can obtain the energy equation:

$$\frac{du_i}{dt} = \frac{P_i}{\rho_i^2} \frac{d\rho_i}{dt} = \frac{P_i}{\rho_i^2 \Omega_i} \sum_j m_j \vec{v_{ij}} \cdot \vec{\nabla}_i W_{ij}(h_i) \tag{3.30}$$

In both the equation above and in the 3.28, we need to put the additional viscosity terms, which assume the same form as discussed in the previous section.

3.4 Advanced technical features

3.4.1 Softened Newtonian interactions and further conservative terms

When we are dealing with a pressureless medium, in estimating gravitational forces between very close particles, several numerical errors can occur due to strong Newtonian terms. One of the classical solution to face this problem is given by softening the potential at short distances. For long distances, it gives back the classical Newtonian contribution, while for short distances it is smoothed out, and the related force fades to zero as particles get closer. Despite introducing some errors in the evaluation the particles trajectories, such scheme prevents singularities from which higher numerical errors may arise. Furthermore, it is necessary in case of a pure pressureless N-body system, since the particles lack a "hydrodynamical" repulsion. To soften the potential, a wide use of Plummer-sphere's radial potential function has been made (see, for instance, Evrard, 1988) :

$$\Phi \propto \frac{1}{(r^2+\epsilon^2)^{1/2}}$$

leading to a softened acceleration:

$$|\vec{a}| \propto \frac{r}{(r^2+\epsilon^2)^{3/2}} \tag{3.31}$$

With this approximation, a particle is not a point mass object anymore, but rather it behaves like a Plummer-like object whose mass is spread out over a "core" radius of the order of ϵ . This radius defines the resolution of the problem, below which gravitational force is being cushioned. ϵ represents a compromise between code accuracy in reproducing the real physical laws and computational costs: the less the radius, the more accurate is the code, the higher the CPU costs needed to handle strong interactions. The choice of the optimal softening is non-trivial and depends on the peculiar system we are dealing with, and it has to minimize the average mean square error (that is, the average squared difference between the real Newtonian force and the approximated force)(Romeo, 1998, Merritt, 1996). For common particles distributions like plummer spheres, the optimal radii in general scale as $\propto N^a$, with $a \leq 1$. Nevertheless, it is expected that, in order to do a realistic simulations without undervaluing the self-potential of a system, ϵ must be a fraction of the average inter-particle distance, and, in case of strong inhomogeneities, it must be a fraction of the mean local distance at the densest regions, i.e. $\epsilon < n_{max}^{-1} \propto N^{-1}$. Some problems arise: for distances greater than ϵ, the interaction restores its Newtonian form, but since the 3.31 still contains ϵ even at highest distances where it's not requested, we'll have some bias on the force estimation. On the contrary, we may choose a different class of softening function, with a compact support, with softening actions disturb the gravitational field of a particle within a limited range. Dehnen (2001), in a comparative study between several models of softening functions, remarked the need of a compact-supported function, to avoid the propagation of several numerical errors outwards. We opted for a radial function (described below) derived from the cubic spline function 3.11, the potential is softened within a radius 2ϵ.

Even for SPH systems, we need to soften the Newtonian force, despite with a different purpose than in the case of pressureless systems. For a gas, SPH particles tend to avoid the singularities: firstly, a gaseous system has a natural inclination to rarefy and to expand thanks to its internal energy; secondly, the artificial viscosity 3.21 prevents excessive compressions. The reason why we need to use softening function is that we are not dealing with point particles. In the SPH formalism, all the physical quantities are not relative to a single point but they rather spread over an effective resolution radius h, thus, even the mass is smoothed out, and the particle position represents just its barycenter. When two particles i and j are out of their smoothing length influence, elementary theorems of the gravitational potential tell us that they should interact with the usual Newtonian force $\propto\ m_i\ m_j\ r^{-2}$. On the other hand, if their mutual distance is less than one, or both, smoothing lengths, they "overlap" and the gravitational potential is smoothed out over their effective volumes $\frac{4\pi}{3}(2h)^3$. Since their first introduction to SPH, Gingold and Monaghan (1977) addressed such issue by describing a smoothed form for the gravitational force. They interpolated the potential $\Phi = -G\int \frac{\rho(\vec{r}')d\vec{r}'}{|\vec{r}-\vec{r}'|}$ by using the 3.8, for the density, and the Poisson equation $\nabla^2\Phi = -4\pi G\rho$, obtaining:

$$\vec{a}(\vec{r}) = -\vec{\nabla}_i\Phi_i = -Gm_i\sum_j\left[-\frac{4\pi}{\xi^2}\int_0^{\xi} W(r',h_i)r'^2dr'\right]\cdot\vec{\nabla}\xi$$

with $\xi = |\vec{r}-\vec{r_j}|$. In our code, we use the same SPH-smoothed Newtonian terms adopted by Hernquist and Katz (1989), who developed the expression above using the cubic spline kernel W. Thus, we have:

$$\begin{aligned}\Phi_{soft}(r,h) &= -m\ G\ f(r,h)\\ \vec{a}_{soft}(r,h) &= -m\ G\ \hat{r}\ g(r,h)\end{aligned}\tag{3.32}$$

where f and g are respectively the softened potential and the softened acceleration terms, such as $\lim\limits_{r>>h} f(r,h) = r^{-1}$ and $\lim\limits_{r>>h} g(r,h) = r^{-2}$. As shown in figure 3.3 they produce a softening for the potential and a dumping for the acceleration, whose absolute value approaches to zero as particles get closer, while for $r \geq h$ g and f restore the classical unsoftened values. So the intrinsic mechanism associated to the

SPH particles gives rise to a natural damping of the classical Newtonian terms. h defines the optimal softening length for self-gravitating gas, even though in their original work Hernquist and Katz (1989) used the 3.32 with a constant $\epsilon < h$ for all the particles. We reserve this latter approach just for non-gaseous particles, while for the gas, we soften the force by means of an adaptive variable h_i different from particle to particle.

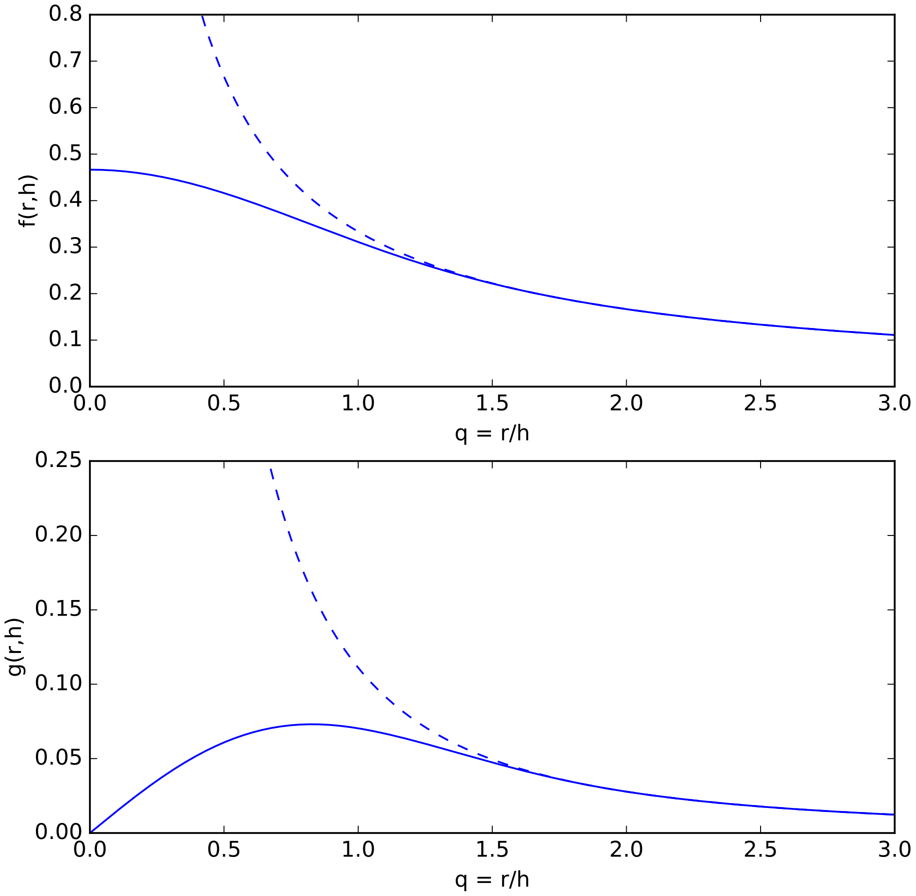

Figure 3.3. Softening functions for the gravitational potential and for the acceleration. Full lines represent $f(r,h)$ (top panel) and $g(r,h)$ (bottom panel). Dashed lines represent the corresponding classical newtonian terms, without softening.

Adaptive softening lengths have been used for the first time by Dehnen (2001), and represent nowadays a paradigm in modern SPH. Nevertheless, the use of an adaptive h does not guarantee the conservation of energy since h can vary with time, affecting the potential. Thus, we have a variable gravitational field and the potential energy varies abnormally with time, causing total energy not to be constant. This constitutes an error since actually the Hamiltonian, lacking explicit time-dependent terms, is constant in time. Price and Monaghan (2007), starting from the Lagrangian

$$L = \frac{1}{2}\sum_i m_i |\vec{r_i}|^2 - \sum_i m_i u_i - \sum_i m_i \Phi$$

applied the same variational principle who leads to 3.27a and 3.27b, this time deriving also the gravitational part of L:

$$L_{grav} = \sum_i m_i \Phi = -\frac{G}{2}\sum_i \sum_j \; m_i \; m_j \frac{\phi(r_{ij}, h_i) + \phi(r_{ij}, h_j)}{2}$$

Besides the pressure normalization Ω_i, a new gravitational correction term appears to the equation of motion:

$$\left[\frac{d\vec{v_i}}{dt}\right]_{corr} = -\frac{G}{2}\sum_j m_j \left(\frac{\zeta_i}{\Omega_i}\vec{\nabla}_i w_{ij}(h_i) + \frac{\zeta_j}{\Omega_j}\vec{\nabla}_i w_{ij}(h_j)\right)$$

with $\zeta_i = -\frac{h_i}{3\rho_i}\sum_j m_j \frac{\partial \Phi(r_{ij}, h_i)}{\partial h_i}$. Thus, the final SPH equation of motion and energy equation, provided with the artificial viscosity terms, are the following:

$$\begin{aligned}
\frac{d\vec{v_i}}{dt} = & -\sum_j G m_j \frac{1}{2}\left(\vec{a}_{soft}(r_{ij}, h_i) + \vec{a}_{soft}(r_{ij}, h_j)\right) \cdot \frac{\vec{r_{ij}}}{r_{ij}} \\
& -\sum_j G m_j \frac{1}{2}\left(\frac{\zeta_i}{\Omega_i}\vec{\nabla}_i W(h_i) + \frac{\zeta_j}{\Omega_j}\vec{\nabla}_i W(h_j)\right) \\
& +\sum_j m_j \left(\frac{P_i}{\rho_i^2 \Omega_i}\vec{\nabla}_i W(h_i) + \frac{P_j}{\rho_j^2 \Omega_j}\vec{\nabla}_i W(h_j)\right) \\
& + \sum_j \; m_j \Pi_{ij} \vec{\nabla}_i \frac{1}{2}\left[W(r_{ij}, h_i) + W(r_{ij}, h_j)\right]
\end{aligned} \tag{3.33a}$$

$$\begin{aligned}
\frac{du_i}{dt} = & \frac{P_i}{\rho_i^2 \Omega_i}\sum_j m_j \vec{v_{ij}} \cdot \vec{\nabla}_i W(h_i) \\
& + \sum_j \; m_j \Pi_{ij} \;\; \vec{v}_{ij} \cdot \vec{\nabla}_i \frac{1}{2}\left[W(r_{ij}, h_i) + W(r_{ij}, h_j)\right]
\end{aligned} \tag{3.33b}$$

where we can recognize the gravitational force to be written in a symmetric form. The pair-wise interaction between two generic particles i and j is driven by an average between two softening functions, evaluated according to the respective lengths h_i and h_j.

3.4.2 Additional point mass objects

As remarked in the first section (page 13), in our code is possible to treat N-body ensemble together with a small number N_{ob} of point-mass objects. An object could represent either a star or a planet and is uniquely defined by its mass and its phase coordinates, plus some optional features (see below). Objects are coupled with gas (or with pressureless particles) by means of a direct point-to-point interaction, without the mediation of the tree-scheme. Furthermore, as will be discussed in the next part, their motion is updated every iteration time without any individual time-step, and their mutual interaction follows the classical direct N^2 approach. Provided that N_{ob} is small (we use maximum 10 objects) in comparison with N (whose common values range between 10^3 and 10^6) the introduction of such particles does not affect significantly the calculous time. Especially for the peculiar purposes of our investigations (in this work we will use $N_{ob} \leq 2$) it practically has a null impact on the efficiency of the code.
Each point mass-particle can be provided with a peculiar softening length ϵ_{ob} and its force field is softened with the same functions 3.32. Consequently, the related equation of motion takes the following form:

$$\begin{aligned}\frac{d\vec{v}_{ob}}{dt} &= -\sum_j Gm_j \frac{1}{2}\left(\vec{a}_{soft}(\vec{r},\epsilon_{ob}) + \vec{a}_{soft}(\vec{r},h_j)\right)\cdot\frac{\vec{r}}{r} \\ &+\sum_k GM_k \frac{1}{2}\left(\vec{a}_{soft}(\vec{r},\epsilon_{ob}) + \vec{a}_{soft}(\vec{r},\epsilon_k)\right)\cdot\frac{\vec{r}}{r}\end{aligned} \tag{3.34}$$

where the first summation is made all of the gas particles with mass m_j, and contains the average of two accelerations, softened according to the gas smoothing length h_j and at the object softening length ϵ_{ob}. The second sum(available in case $N_{ob} > 1$) is made over the other object of mass M_k. It contains the average value of two Newtonian forces softened according to the respective length ϵ_{ob} and the generic ϵ_k. Of course, we upgrade the 3.33a by adding the following term :

$$-\sum_{k=1}^{N_{ob}} GM_k \tfrac{1}{2}\left(\vec{a}_{soft}(\vec{r}_{ik},\epsilon_k) + \vec{a}_{soft}(\vec{r}_{ik},h_i)\right)\cdot\frac{\vec{r}_{ik}}{r_{ik}}$$

where index k again refers to the point masses.

As for the gas-gas interaction, with object-gas coupling, we have the same problem of non-conservation of the total energy. The variation of h introduces further spurious noises into the Hamiltonian, which now contains also the gravitational terms related to stars and planets. We would need hence to use a variational approach in order to derive the new gravitational terms of L. Hubber et al. (2013) indeed fixed this issue and found additional corrective terms. As a result, equation 3.34 does not change, while in 3.33a only a little change is made in the terms ζ_i. Point-mass objects may be provided by a sink radius, too. In some cases, as will be shown for protoplanetary disks, this helps to avoid too large forces and with too expensive computational efforts. A softening potential is already able to prevent singularities, but massive objects (like stars) may accumulate matter at high pressures and densities, leading to very small timesteps and reducing the efficiency of the algorithm. The particles which approach the star within the sink radius are removed from the algorithm, and their mass is absorbed by the object.

3.4.3 Integration technique

To let the gas evolve, we adopt a 2nd order integration method, very similar to a classical 2nd order *Runge-Kutta* scheme but, at the same time, very close to a Leap Frog integrator: the well-known *Velocity-Verlet* method (see Andersen (1983), Allen and Tildesley (1989), chapter 3, for a detailed reference). The Verlet method is made of a trapezoidal scheme coupled with a predictor-corrector technique for the estimation of $\vec{v}$ and u.

Each time iteration, $\vec{a}$ and $\dot{u}$ are evaluated twice, in correspondance to the current step n and the next $n+1$. We use $\vec{a}^{[n]}$ and $\dot{u}^{[n]}$ to predict the velocity and the energy:

$$\begin{aligned} \vec{v^*}^{[n+1]} &= \vec{v}^{[n]} + \vec{a}^{[n]} \cdot \Delta t \\ u^{*[n+1]} &= u^{[n]} + \dot{u}^{[n]} \cdot \Delta t \end{aligned}$$

while the position is directly updated to the next step $n+1$, without any prediction:

$$\vec{r}^{[n+1]} = \vec{r}^{[n]} + \vec{v}^{[n]}\Delta t + \frac{1}{2}\vec{a}^{[n]}\Delta t^2 \tag{3.35}$$

With such new quantities, a new calculation is performed for $\vec{a}$ and $\dot{u}$ we thus have :

$$\begin{aligned} \vec{a^*}^{[n+1]} &= \vec{a}\left(\vec{r}^{[n+1]}, \vec{v^*}^{[n+1]}, u^{*[n+1]}\right) \\ \dot{u^*}^{[n+1]} &= \dot{u}\left(\vec{r}^{[n+1]}, \vec{v^*}^{[n+1]}, u^{*[n+1]}\right) \end{aligned}$$

which we can use to correct velocity and energy :

$$\begin{aligned}\vec{v}^{[n+1]} &= \vec{v}^{[n]} + \left(\vec{a}^{[n]} + \vec{a}^{*[n+1]}\right) \cdot \frac{\Delta t}{2} \\ u^{[n+1]} &= u^{[n]} + \left(\dot{u}^{[n]} + \dot{u}^{*[n+1]}\right) \cdot \frac{\Delta t}{2}\end{aligned} \tag{3.36}$$

It can be straightforwardly shown that, when acceleration does depend only on the positions, i.e. in a Newtonian problem without the involvement of the hydrodynamics, the Verlet method described above is equivalent to a standard 2nd order *Kick-Drift-Kick (KDK)* LeapFrog method. As a matter of fact, if the acceleration does not depend on the velocity field nor on the internal energy, the quantity $\vec{a^*}^{[n+1]}$ corresponds to the actual acceleration $\vec{a}^{[n+1]}$ related to the next step. The numerical method can thus be rewritten in the following way:

$$\begin{aligned}\vec{r}^{[n+1]} &= \vec{r}^{[n]} + \left(\vec{v}^{[n]} + \frac{1}{2}\vec{a}^{[n]}\Delta t\right)\Delta t = \vec{r}^{[n]} + \vec{v}^{[n+1/2]}\Delta t \\ \vec{v}^{[n+1]} &= \vec{v}^{[n]} + \frac{1}{2}\vec{a}^{[n]}\Delta t + \frac{1}{2}\vec{a}^{[n]}\Delta t = \vec{v}^{[n+1/2]} + \vec{a}^{[n]}\frac{\Delta t}{2}\end{aligned}$$

which is indeed the standard expression of a KDK Leap-Frog integrator that requires just one force calculation per time-step (see Hockney and Eastwood, 1988, Hut et al., 1995, Quinn et al., 1997, for leap-frog methods and further improvements). The main structure of such a scheme is very similar to the one adopted by the classical symplectic leap-frog algorithms, although it requires a force estimation twice per iteration. Nevertheless, the general Velocity-Verlet method applied to gas takes a more advantage with respect to the symplectic algorithm. Indeed, like a standard Runge Kutta method, velocity and positions are updated in correspondence to synchronized times, without the shift $\Delta t/2$. Such a feature provides a good flexibility in problems with non-uniform time-step and which involve the interaction of the gas with different components integrated with different methods, as in our cases. We can find applications of Velocity-Verlet methods in SPH schemes for example in Hubber et al. (2013) or in Hosono et al. (2016).

The additional point-mass objects don't constitute a diffuse medium, they are rather ballistic elements whose trajectories need to be calculated with a very high precision, in order to perform realistic simulations. For such purposes, we integrate the mutual Newtonian interaction between stars and planets with a 14th order Runge-Kutta method, recently developed by (Feagin, 2012) through the so-called *m-symmetry* formalism. The method consists in 35 force computations per timestep and, in analogy with the well-known 2nd and 4th order RK algorithms, it updates the velocities and the positions by suitable linear combinations of 35 different $\vec{Kr}$ and $\vec{Kv}$ coefficients. For a generic set of N_{ob} objects we want to integrate the following differential equations associated with a generic object i :

$$\frac{d\vec{r_i}}{dt} = \vec{v_i} \qquad \frac{d\vec{v_i}}{dt} = \vec{f_i}$$

we make a first estimation of the explicit derivatives at the iteration n:

$$\begin{aligned} \vec{Kv}_1^{(i)} &= \vec{f}(\vec{r}_1^{[n]}, \vec{r}_2^{[n]}, ..., \vec{r}_i^{[n]}, ..., \vec{r}_N^{[n]}) \\ \vec{Kr}_1^{(i)} &= \vec{v}_i^{[n]} \end{aligned}$$

which we use to estimate the further quantities to a second sub-step $n + c_2$:

$$\begin{aligned} \vec{Kv}_2^{(i)} &= \vec{f}(\vec{r}_1^{[n+c2]}, \vec{r}_2^{[n+c2]}, ..., \vec{r}_i^{[n+c2]}, ..., \vec{r}_N^{[n+c2]}) \\ \vec{Kr}_2^{(i)} &= \vec{v}_i^{[n]} + a_{21}\vec{Kv}_1^{(i)}\Delta t \end{aligned}$$

where $\vec{r}_i^{[n+c2]} = \vec{r}_i^{[n]} + a_{21}\vec{Kr}_1^{(i)}\Delta t$ represents the i-th particle position updated to an intermediate time $t + c_2\Delta t$. Then we start an iterative cycle of consecutive extimations of β-th terms:

$$\begin{aligned} \vec{Kv}_\beta^{(i)} &= \vec{f}(\vec{r}_1^{[n+c\beta]}, \vec{r}_2^{[n+c\beta]}, ..., \vec{r}_i^{[n+c\beta]}, ..., \vec{r}_N^{[n+c\beta]}) \\ \vec{Kr}_\beta^{(i)} &= \vec{r}_i^{[n]} + \sum_{\gamma=1}^{\beta-1} a_{\beta\gamma}\vec{Kv}_\gamma^{(i)}\ \Delta t \end{aligned} \tag{3.37}$$

with $\vec{r}_i^{[n+c\beta]} = \vec{r}_i^{[n]} + \sum_{\gamma=1}^{\beta-1} a_{\beta\gamma}\vec{Kr}_\gamma^{(i)}\Delta t$ the vector position of particle i at a generic intermediate time $t+c_\beta\Delta t$. Note that, since $\gamma < \beta$, every quantity depends explicitly on previous estimations. The coefficients $a_{\beta\gamma}$ are the elements of a 35x34 matrix, while b_β and c_β represent two arrays of 35 elements (see Appendix A for the detailed list of the elements). The matrix a requires the following restriction:

$$\sum_{\gamma=1}^{34} a_{\beta\gamma} = c_\beta \tag{3.38}$$

Since we are dealing with a full explicit method, a is triangular, and $a_{\beta\gamma} = 0$, for $\gamma > \beta$. In total, each star will have 35 velocity-coefficients $\vec{Kr}_\beta$ and 35 acceleration-coefficients $\vec{Kv}_\beta$, the resultant velocity and position at the next time step will be given by:

$$
\begin{aligned}
\vec{v}_i^{[n+1]} &= \vec{v}_i^{[n]} + \sum_{\beta=1}^{35} b_\beta \vec{Kv}_\beta^{(i)} \Delta t \\
\vec{r}_i^{[n+1]} &= \vec{r}_i^{[n]} + \sum_{\beta=1}^{35} b_\beta \vec{Kr}_\beta^{(i)} \Delta t
\end{aligned}
\tag{3.39}
$$

To calculate the time evolution of a mixed gas + stars system, we couple the Verlet and the RK integration methods as follows. At the starting iteration n, the gas particles feel the gravity field from the stars, the SPH mutual interactions and eventually its self-gravity. Their positions are thus updated according to the 3.36, furthermore $\vec{v^*}^{[n+1]}$ and $u^{*[n+1]}$ are predicted. At the same time, stars positions and velocities are first updated with the Runge-Kutta method, then, the explicit force contributions due to the SPH particles $\vec{a}_{part}^{[n]}$ are added to the 3.38. Stars and SPH particles are coupled by direct point-to-point interaction, without any approximation for the gravitational field. Finally, we correct the gas positions and velocity according to the 3.36, by recalculating the accelerations and the energy rates at the new stage $n+1$.

3.4.4 Time stepping

We chose the time-step Δt following a standard Courant-Friedrichs-Lewy criterion commonly adopted for SPH systems (see for example Monaghan, 1992,), and by putting some additional criteria. For each particle, an individual timestep Δt_i is determined by considering the minimum of the following two quantities:

$$
\begin{aligned}
\Delta t_{term} &= \min\left(\frac{C\ h}{c_s + h|\vec{\nabla}\cdot\vec{v}| + \varphi\left[\alpha c_s + \beta \max\limits_j(\mu_{ij})\right]}\ ,\ C_u \frac{u}{\dot{u}} \right) \\
\Delta t_{dyn} &= \min\left(C_a \sqrt{\frac{h}{a}}\ ,\ C_d \frac{v}{a} \right)
\end{aligned}
\tag{3.40}
$$

where C represents the classical courant factor (typical values used lies between 0.1 and 0.4, we usually choose 0.15). $C_a = 0.14$. $C_d << 1$ represents a coefficient which quantifies the relative $|\vec{v}|$ variation in an interval Δt (after a time integration, the kinetic energy variation ratio for each particle would be thus limited approximately to $\sim 2c_d$). We choose $C_d = 0.02$. c_s is the usual speed of sound, while φ is a coefficient, typically ranging from 0.6 to 1.2, we will adopt the latter value for all the works presented in this paper. As for the kinetic energy, in a single time-step, the variation of the thermal energy $u/\dot{u}$ is limited to a certain fraction $C_u = 0.04$.

For a non-hydrodynamical particle system, the individual timestep Δt is limited to Δt_{dyn} , with a constant softening radius ϵ in place of h. The same form of timestep is used for the mutual interaction between ballistic objects:

$$\Delta t_{dyn} = \min_{ob} C_{ob} \left(\sqrt{\frac{\epsilon_{ob}}{a}}, C_d \frac{v_{ob}}{a_{ob}} \right)$$

We use $C_{ob} = 0.15$.For a homogeneous medium, integration can be performed with a global timestep $\Delta t_{min} = \min_i \Delta t_i$, the smallest value calculated among all the particles and all the stars. But generally, the particles have different resolutions h_i and different accelerations which lead to a wide class of typical evolution time-scales. Thus, for some particles, the integration could be done with different Δt_i, avoiding the explicit force calculous every iteration, and saving some CPU time. We adopt a usual technique implemented in several N-body algorithms, like, for instance, in the classical TREE-SPH (Hernquist and Katz, 1989) or in the multi-GPU-parallelized N-body code HiGPUs (Capuzzo-Dolcetta et al., 2013). We assign to each point a time-step as a negative 2-power fraction of a maximum timescale $\Delta t_{max} = \max_i(\Delta t_i)$ (it can be a fixed parameter or it may change during a simulation). Particles are updated periodically according to their Δt, in such a way that, after an integration time Δt_{max}, all of them are synchronized. In our scheme, the stars and planets don't follow an individual time-step scheme and are integrated following the minimum timestep. Furthermore, even the particles sufficiently close to the stars are integrated according to Δt_{min}. Practically, we evaluate the distance of each particle from the stars and predict the distance at the following time iteration, too. If such values are smaller than $\kappa\epsilon_{ob}$ (with ą$constant \geq 2$), the particle timestep drops to Δt_{min}. As a matter of fact, for our practical purposes, a small number of the object is expected to be used ($N_{ob} <= 10$), thus, the 35-stage RK scheme turns out to require a relatively small CPU time (less than 1% with 10^4 gas particles).

In gas problems involving strong shocks, the use of individual timesteps may lead to strong errors. Even thought courant conditions are satisfied, the strong velocity and energy gradients may determine too strong differences in timestep even between close particles. Consequently, close particles may be integrated with excessively different time-scales. This may create too asymmetries in the their mutual interaction. causing unphysical discontinuities of velocity and pressure and consequently leading to errors. Following the idea of Saitoh and Makino (2009), for each couple of neighbour particles i and j, we limit the ratio of timesteps $\frac{\Delta t_i}{\Delta t_j} \leq A$. The investigators have shown that a good compromise is given by the choice of $A = 4$, which gives good results without affecting abruptly the efficiency of the code.

3.4.5 Shared memory parallelization

We parallelized the code to run with shared-memory architectures by using the standard OpenMP libraries. We implemented a parallelization both for the density evaluation routine and for $\vec{a}, \dot{u}$ calculation, distributing the operations made for different particle to different threads. In the latter routine, both the far gravitational forces and the close hydrodynamical interactions may cause, for two or more different particle, to update the same quantity during the same routine cycle. Thus, many so called *Data-Race* problems could arise: two or more threads may get access and update the same memory location at the same time, leading errors in storing the correct values. To overcome such issues, for each processor P, a private memory is allocated to memorize temporary quantities $\vec{a}_P$ and $\dot{u}_P$. After the main cycle of force evaluation, temporary array are summed index by index and finally stored to the memory :

$$\vec{a} = \sum_P \vec{a}_P \qquad ; \qquad \dot{u} = \sum_P \dot{u}_P$$

In total, $4N \cdot N_{th}$ real values are stored, being N_{th} the number of threads (they request a relatively small amount of ram memory: $32N_{th}$ Mbytes per million of particles, in double precision).

In figure 4.20 of the next chapter, we put in comparison the CPU-times needed by the serial vesion of our algorithm and its parallelized version. We evaluated the speedup in function of several processors number PN employed, performing an entire cycle of calculous, both for density routine and for accelerations routine. The tests show satisfying results for low PN while the efficiency degrades for $N_{th} \leq 4$: we reach a maximum speedup of 5.3 out of an ideal value of 8.

Chapter 4

Code testing and performance

4.1 Gaseous and pressureless systems

4.1.1 Plummer distribution of point-mass particles.

In this subsection we are going to show some tests performed to check the stability of the code. We placed a set of self gravitating pressureless particles in a plummer distribution (Plummer, 1911), such as, a radial number density:

$$n(r) \propto M \left(1 + \frac{r^2}{r_0^2}\right)^{-5/2}$$

in a local virial equilibrium, such as, for every particle, the total binding energy $E < 0$ follows the distribution $f(E) \propto E^{7/2}$ (Eddington, 1916). Units are the total mass of the sysem M, the gravitational constant G, and r_0. We placed an ensemble of $N = 10^5$ and conventionally choosing a cutoff radius $r_c \approx 18 r_0$ (the one containing 99.5% of the total mass of an ideal distribution from $r = 0$ to $r = \infty$. Particles had equal mass $m = N^{-1}$ and equal softening lenght ϵ, chosen as a fraction of the central mean interparticle distance: $\epsilon = \alpha_{soft} \cdot \left(\frac{m}{\rho_0}\right)^{1/3} = \alpha_{soft} \cdot \left(\frac{4\pi}{3N}\right)^{1/3}$ (with $\alpha_{soft} \in [0.2, 1]$).

Setting the plummer distribution in a dynamical equilibrium configuration, we integrated its time evolution for 50 mean crossing-times τ_c. Such parameter is defined as the initial ratio between the half mass radius $R_{1/2}$ and the mean dispersion velocity: $\tau_c \equiv \frac{R_{1/2}}{\sqrt{<v^2>}}$. Figure 4.1 shows the virial factor $\frac{2T}{|\Omega|}$ (expected to fluctuate in equilibrium around the mean value 1) in function of time, comparing four runs made by using different combinations of θ $(0.6; 1.0)$ and ϵ $(0.2; 0.5)$.

The four results illustrated in figure 4.1 do not show any relevant differences: virial ratio oscillates whithin a small fraction $< 1\%$. Especially the case with $\theta = 1$ and $\alpha_{soft} = 0.5$, which was expected to be the most approximative, turns out to be

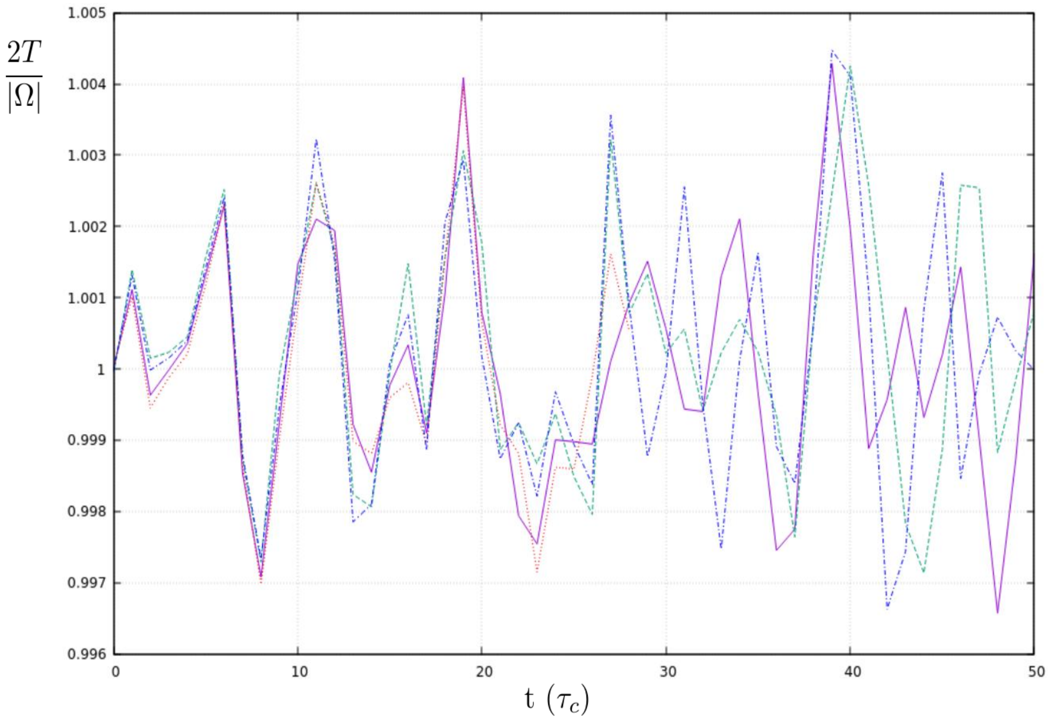

Figure 4.1. Plummer distribution of 10^5 equal-mass particles. Oscillation of virial factor in function of time, for 4 different configurations. Continuous line: $\theta = 0.6$, $\epsilon = 0.2$; dashed line: $\theta = 1.0$, $\epsilon = 0.2$; dotted line: $\theta = 0.6$, $\epsilon = 0.5$; dashed-dotted line: $\theta = 1.0$, $\epsilon = 0.5$. Time units: τ_c.

a good configuration. Furthermore, the radial mass distribution at the equilibrium state is preserved, as can be seen in figure 4.2, where we indicated the lagrangian radius values (respectively the radial values containing the 15%, 30%, 50% and 75% of the total mass) after 50 crossing times, for $\theta = 1$ and $\alpha_{soft} = 0.5$. Their values remains exactly the same with respect to the initial ones. It is worth to note that here we are not dealing with a classical regularized N-body code (a well-known example can be given by the N-body6 code; seeAarseth (1999) for references) and thus the newtonian potential is damped when the particles approach within a distance of the order of ϵ, giving raise to errors.

4.1.2 The 2 body problem

We are going to discuss now some questions related to the peculiar numerical method we adopted. Tipically, *Symplectic Leap-frog* methods are largely used in lagrangian problems involving gas. One reason is that they guarantee a satisfying long-time energy conservation, since the time evolution of the phase variables is performed by means of canonical transformations, which depend on a constant Hamiltonian. On

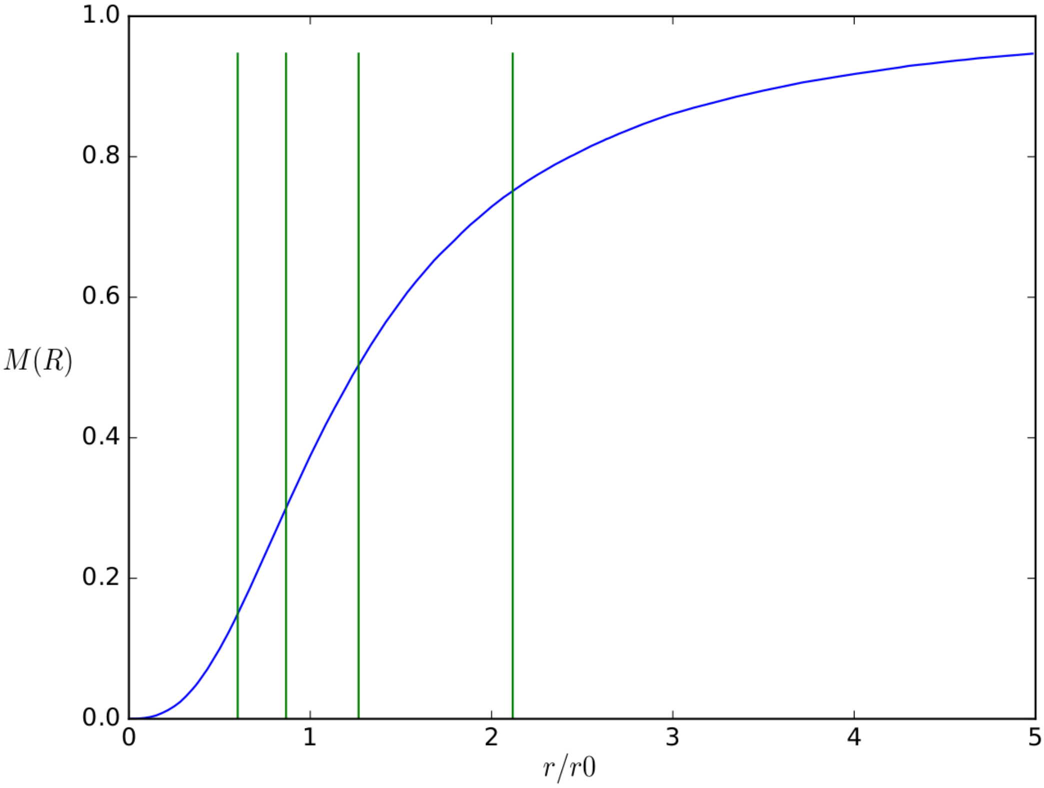

Figure 4.2. Cumulative radial mass distribution of a plummer-distributed system, after a 50-crossing-times evolution, defined as : $M(R) = 4\pi \int_0^R \rho(r)dr$. $\theta = 1$ and softening parameter $\alpha_{soft} = 0.5$. Vertical lines indicate the values of the Lagrangian radii R_{15}, R_{30}, R_{50}, R_{75}.

the other hand, they require just one acceleration calculous per timestep, providing a good efficiency (we remind Dehnen (2011), for an explanation of Leap-Frog and other methods for the resolution of gravitational N body problems). Nevertheless, in some peculiar circumstances, such schemes don't guarantee a perfect extimation of the particles trajectories. Furthermore, when we integrate with a non constant dt, both in space and time, the intrinsical structure of the Leap Frog (required to guarantee a 2nd order accuracy) is broken, and some sophisticated techniquest to restore the symmetry are required. This is a well known issue which Hut et al. (1995) and Quinn et al. (1997) tried to overcome by introducing some sophisticated improvements to the classical receipt of the Leapfrog. Two are the most suitable Leap Frog methods: the so called Drift-Kick-Drift(DKD) and the Kick-Drift-Kick(KDK). Figure 4.3 is taken from the well-known work of Springel (2005), related to the introduction of the Code *GADGET-2*, designed to treat gas evolution and peculiarly for Cosmological simulations. It compares the two symplectic methods showing a simple integration of the 2-body problem with high eccentricity orbits, in a variable time-step approach. Orbits are expected to be constant but, as it can be seen, leap-frog integrators accumulate significative errors after 200 orbits and the trajectories of the particles correspond no longer to the actual keplerian solution, despite the KDK provides better results than the DKD and the semimajor axis doesn't make any precession. Time-step is chosen according to the criterium $dt = \frac{\alpha'}{\sqrt{|\vec{a}|}}$, calibrating α' in such a way that there are $200 \div 250$ timesteps per orbital period.

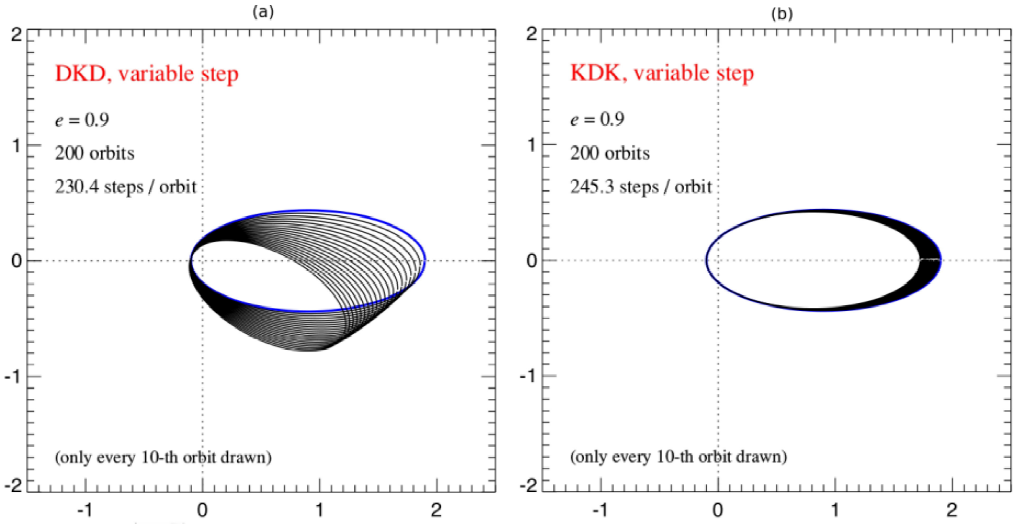

Figure 4.3. Advanced leap-frog method (KDK and DKD) applied to a strong 2-body problem. Picture taken from Springel (2005) (pp. 116).

We will show now an application of the RK2nd order to the same problem: we placed two equal-mass point particles (without softening radius i.e $\epsilon = 0$) in an elliptical relative motion, with orbital eccentricity $e = 0.9$.

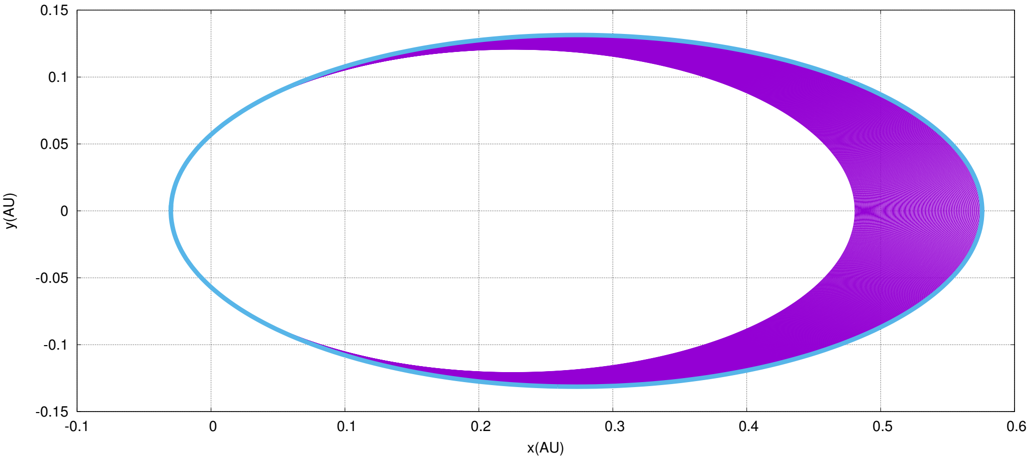

Figure 4.4. 2 body problem with the Runge-Kutta 2nd order integrator: relative elliptical orbit, eccentricity 0.9. Time-step criterium $dt \propto \sqrt{\frac{1}{|\vec{a}|}}$ Blue ellipse refers to the initial orbit, while cumulative trajectories after 200 initial orbital period, are plotted in purple.

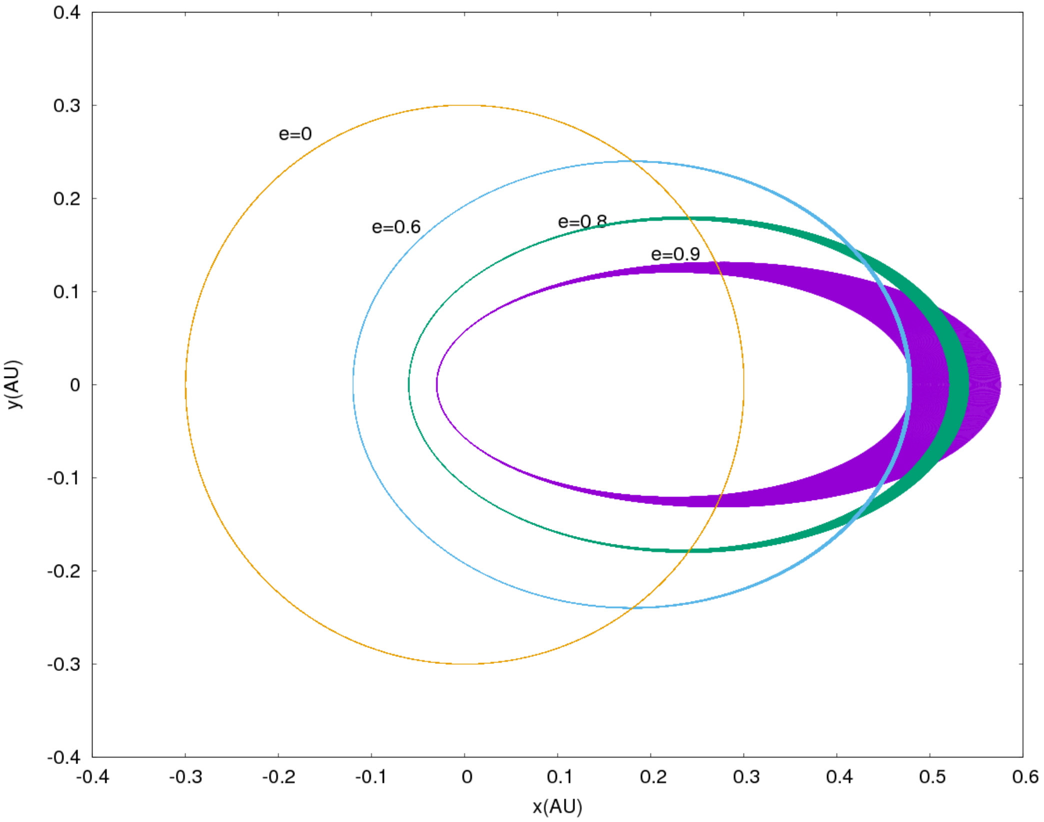

Figure 4.5. 2 body problem with the Runge-Kutta 2nd order integrator: same plot as 4.4, comparison between different runs with different eccentricities.

Figure 4.4 shows the relative trajectory, within an integration time of 200 initial orbital periods, with the same timestep accuracy as used for the leap-frogs: $dt \propto \frac{1}{\sqrt{|\vec{a}|}}$, 264 timestep per orbit. The RK2 method we adopted in our algorithm gives back errors comparable with KDK, furthermore, it is fully explicit and, as illustrated in the previous chapter 3.1, it needs extimation of the derivatives just for the current and the next time-step, without introducing asymmetries due to intermidiate steps. Figure 4.5 compares different configurations of the same 2-body problem integrated with the RK2, with different values of eccentricities. Despite the strong case of $e = 0.9$, for $e <= 0.8$ we have a few deviation of the orbits from the keplerian law, with a reduction of the semimajor axis of less than 5%. The time-step criterium adopted for such examples represents a suitable choice as far as we are dealing with pressureless particles, with zero or constant gravitational softening length. For SPH particles, dynamical timestep-criterium follows the rule $dt \propto \frac{h}{|\vec{a}|}$ (as can be found in Monaghan, 1992, Springel, 2005, Wetzstein et al., 2009, for instance). Since the smoothing length h scales approximatively as the local mean interparticle distance, one can write $dt \propto \frac{r}{|\vec{a}|}$.

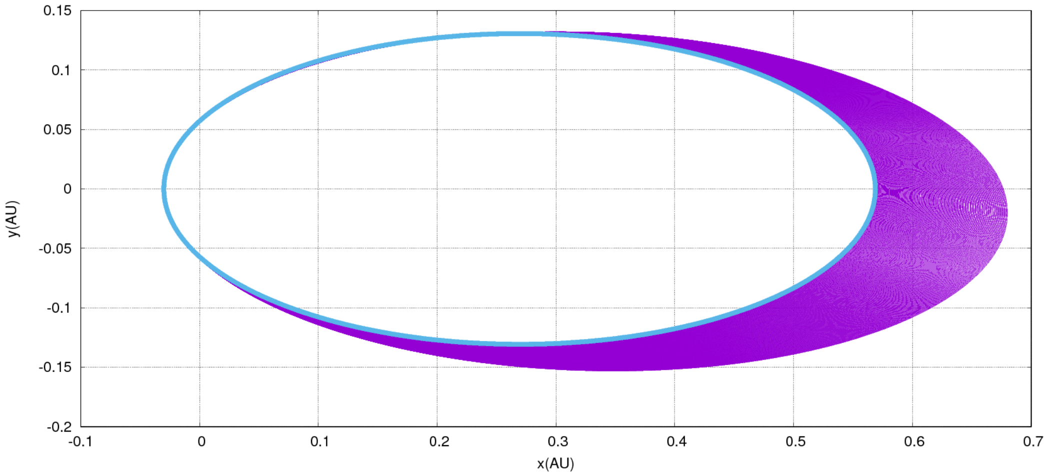

Figure 4.6. 2 body problem with the Runge-Kutta 2nd order integrator: relative elliptical orbit, eccentricity 0.9 . Time-step criterium: $dt \propto \sqrt{\frac{r}{|\vec{a}|}}$. Blue ellipse refers to the initial orbit, while cumulative trajectories after 200 initial orbital period, are plotted in purple.

Integrating the 2-body problem according to the latter criterium, we may have a clearer idea about the code accuracy with gas systems. Figue 4.6 and 4.7 shows the relative orbits of two bodies with in the same configuration as illustrated in 4.4 and 4.5, but with a time-step scaling as $\approx \frac{r}{|\vec{a}|}$. Differently from the previous situation, after 200 periods, for $e > 0$ we have a sligh precession of the semimayor axis, while for $e = 0$ the circular orbits mantain their shape. The main purposes

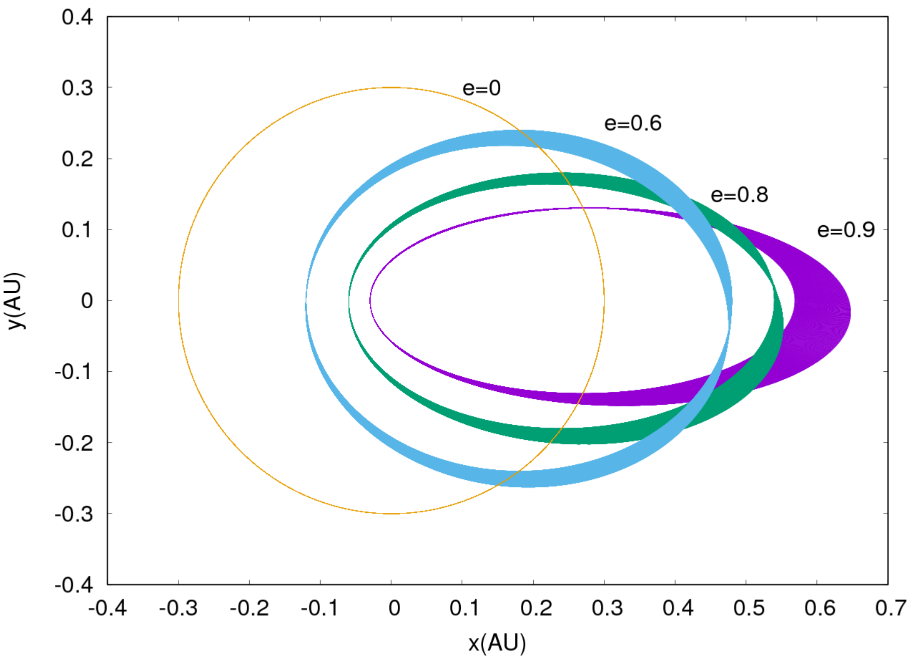

Figure 4.7. Integration of the 2-body problem with the timestep criterium $dt \propto \sqrt{\frac{r}{|\vec{a}|}}$. For $e = 0, e = 0.6, e = 0.8, e = 0.9$, we have integrated the orbit with a number of timesteps dt per orbital period respectively 199, 215, 238, 278.

of the tests introduced so far consisted in giving an idea of the accuracy of the Runge-Kutta 2nd order method to face dynamical problems, in comparison with the leap-frog. Nevertheless, the inability of such schemes to preserve energy after systematic accumulations of error does not affect pretty much the accuracy of the code in handling gas or in general collisionless systems. In fact, as remarked by Springel (2005), in collisionless systems or gaseous systems we don't have the same situation as illustrated in the previous examples, the gas particles rather make very few close orbits during a typical dynamical time. Furthermore, the errors are distributed among a wide neighbourhood of particle without affecting the position or the velocity of a single point.

4.1.3 The accuracy of the 14-th order Runge kutta method.

Differently from the case of non collisional systems, the close interactions among stars and/or planets, for instance the keplerian orbits of a binary system star + star or star + planet, may be integrated as accurately as possible. As remarked in the previous section, the exact determination of the ballistic trajectories of stars and planets need to be determined with a very small error, in order to make realistic investigations.

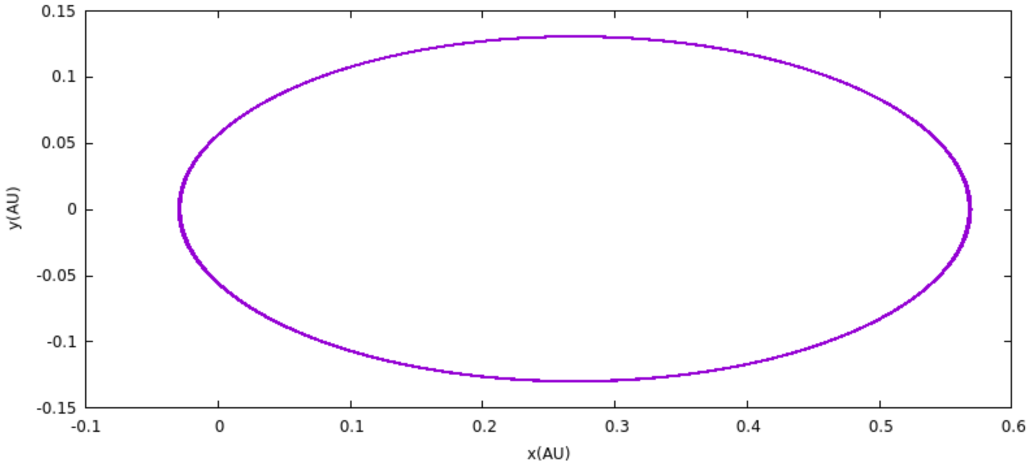

Figure 4.8. 2 body problem integrated with the 14th order RK method. Overall relative position of two equal-mass bodies, during an integration time of 10^5 orbital periods. The curve matches a perfect eccentric ellipse within an error of $\approx 10^{-7}\%$.

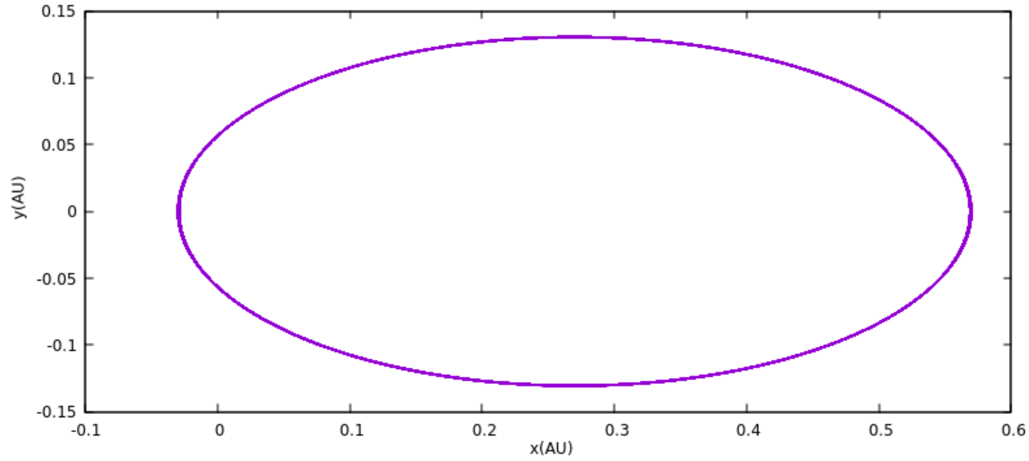

Figure 4.9. Same as Figure 4.8, but with a mass ratio of 10^6 between the two bodies. Integration requested the 40 % of interation more than the previous run.

Here we show an example of high eccentric keplerian motion integrated with the Runge-Kutta-14th order method, applied to two equal massive stars, for an integration time of 10^5 orbital periods. The time-step criterium $dt \propto |\vec{a}|^{-1/2}$ has been used, with 245 timesteps per orbital period. As for the examples shown above, the relative position coordinates of the two objects $x = x_1 - x_2$ and $y = y_1 - y_2$, are plotted in Figure 4.8, for all the time intervall of integration. Differently from the previous case, the trajectories remains the same and the elliptical orbit remains stable. Periastron and Aphastron have a relative variation (defined, as usual, as the variation with respect the initial value, divided by the initial value) of the order of 10^{-9}, while energy varies of less than 5×10^{-7} %. A similar test, using the same eccentricity, is illustrated in figure 4.9, despite the two objects have now a huge mass ratio $M_1/M_2 = 10^6$. There are no relevant differences in terms of accuracy, with respect to the previous test, the only difference lies in the number of iteration necessary to integrate for a single orbital period; it increases of about 40% .

4.1.4 Sedov-Taylor blast wave solution

We now show an application to the blast waves explosions, to test the accuracy of the artificial viscosity in handling with strong shock waves. Given a homogeneous medium with constant density ρ_0 and null pressure, if an ammount of energy E_0 is injected at a certain point r_0, an explosion occurs and a radial symmetric shock wave then propagates outwards. L.I.Sedov (1959) investigated such problem and found a simple analytical law for the time evolution of the shock front:

$$r_s(t) = \left(\frac{E_0}{\rho_0 \cdot a}\right)^{1/5} \cdot t^{2/5} \tag{4.1}$$

where r_s is the radial position of the front, relative to the point of the explosion r_0, while a is a function of the adiabatic constant γ (it is close to 0.5 for $\gamma = 5/3$, and it approaches 1 for $\gamma = 7/5$). Furthermore, the fluid density, pressure and velocity right behind the shock front ($r <= r_s$) have the following radial profile:

$$\begin{aligned} \rho(r,t) &= \frac{\gamma+1}{\gamma-1}\rho_0 \quad G_\gamma\left(\frac{r}{r_s}\right) \\ P(r,t) &= \frac{8\rho_0}{25\,(\gamma+1)}\frac{r^2}{t^2} \quad W_\gamma\left(\frac{r}{r_s}\right) \\ v(r,t) &= \frac{4}{5\,(\gamma+1)}\frac{r}{t} \quad U_\gamma\left(\frac{r}{r_s}\right) \end{aligned} \tag{4.2}$$

being G_γ, W_γ and U_γ some non analytical functions of the relative radial coordinate r/r_s .

Similarly as many previous works (see for example Rosswog and Price (2007) or Tasker et al. (2008)), we set the initial conditions for a homogeneous and static medium ($\rho_0 = 1$, $v = 0$) by placing 10^6 equal-mass particles in a cubic lattice structure, confined in a squared box with x,y, and z coordinates ranging, each one, from -1 to 1. γ was set to 5/3, and the explosion was simulated by giving an amount of energy $E_0 = 1$ to the origin of the system. Space, density, and energy units are set to 1, in such a way that a single particle has a mass of 8×10^{-6} and time units are automatically set to 1. Actually, in an SPH framework, we are not able to reproduce a point explosion with an SPH system, i.e. we are not allowed to concentrate E_0 to a single point, since the spatial resolutions characterizing the physical variables are determined by the kernel support. Hence, we neededed to inject the energy in a small region with the same scale as $2h$. We thus gave, at a time t_*, the energy E_0 to those particles enclosed in a sphere having radius $R = 2h$. Figure 4.10 shows the time evolution of the system along the x,y, plane, considering a slice with thickness 0.05 and passing to the axis origin. Figures 4.11,4.12,4.13, 4.14 and 4.15 shows the radial profile of the density, pressure, internal energy, SPH viscosity α, and smoothing lenght, compared with their analitical expected solution, at t = 0.2. Figure 4.16 illustrates the average values of radial $\rho(r, t')$ and $P(r, t')$ peofiles at t=0.2. Despite the position of the front follows the expected law, the density does not reach the maximum value expected, in this case $\frac{\gamma+1}{\gamma-1}\rho_0 = 4$. Due to the smoothing kernel, the density spreads out and follow a different distribution with respect to the analytical one. Consequently, the shock front is enlarged of the order of the local smoothing lenght h, rather than following a vertical discontinuity.

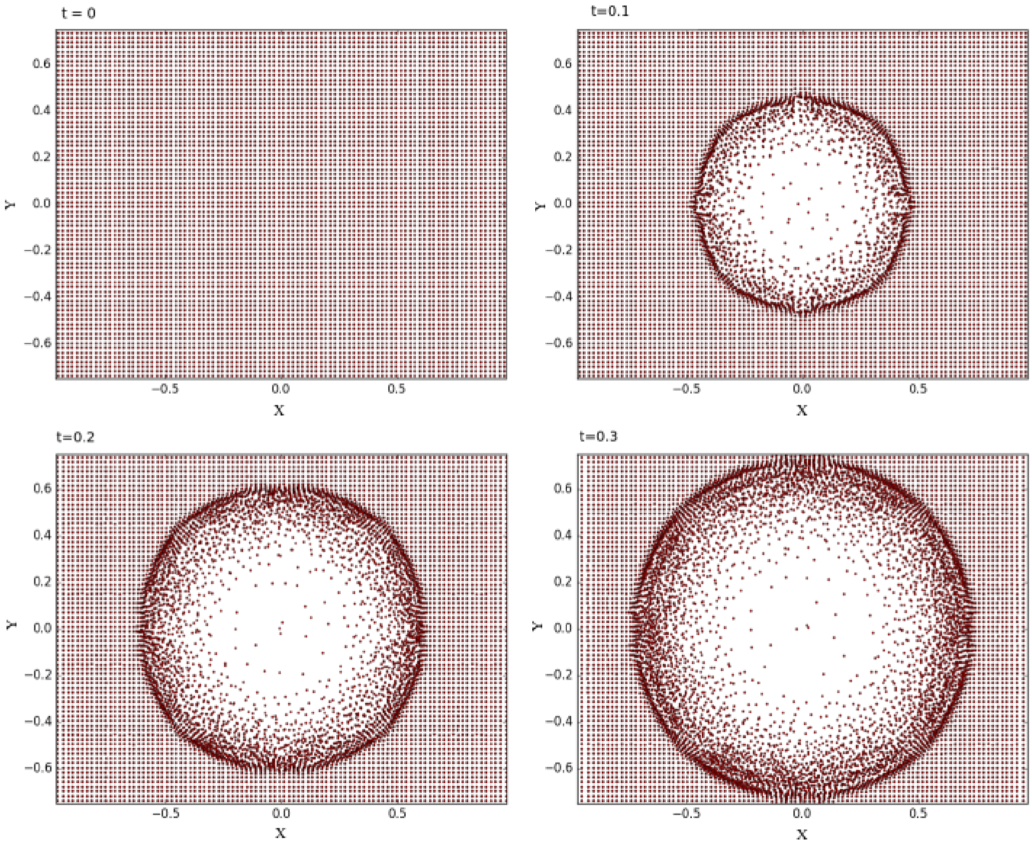

Figure 4.10. Sedov-Taylor blast wave test: Particle position projected on x,y plane, from z=-0.05 to z=0.05, at different times.

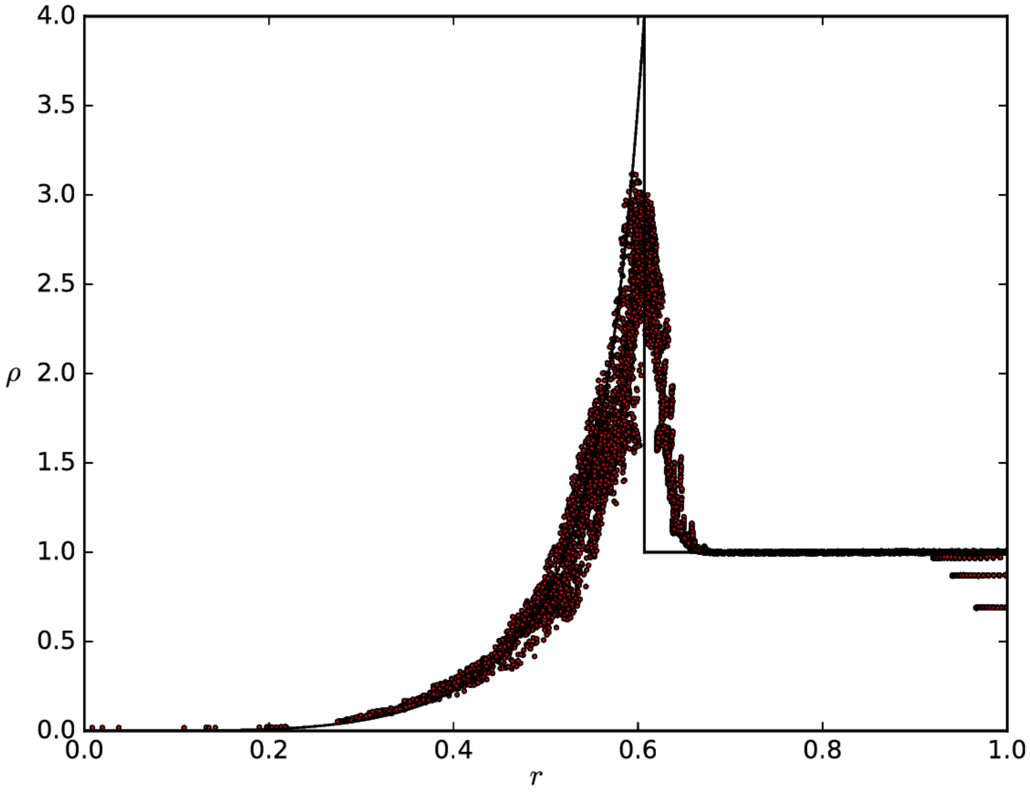

Figure 4.11. Sedov-Taylor blast wave test: Particles density in function of the radial distance from the explosion point. t=0.2 . Red dots represent the numerical result of the test, black continuous line is the expected theoretical solution.

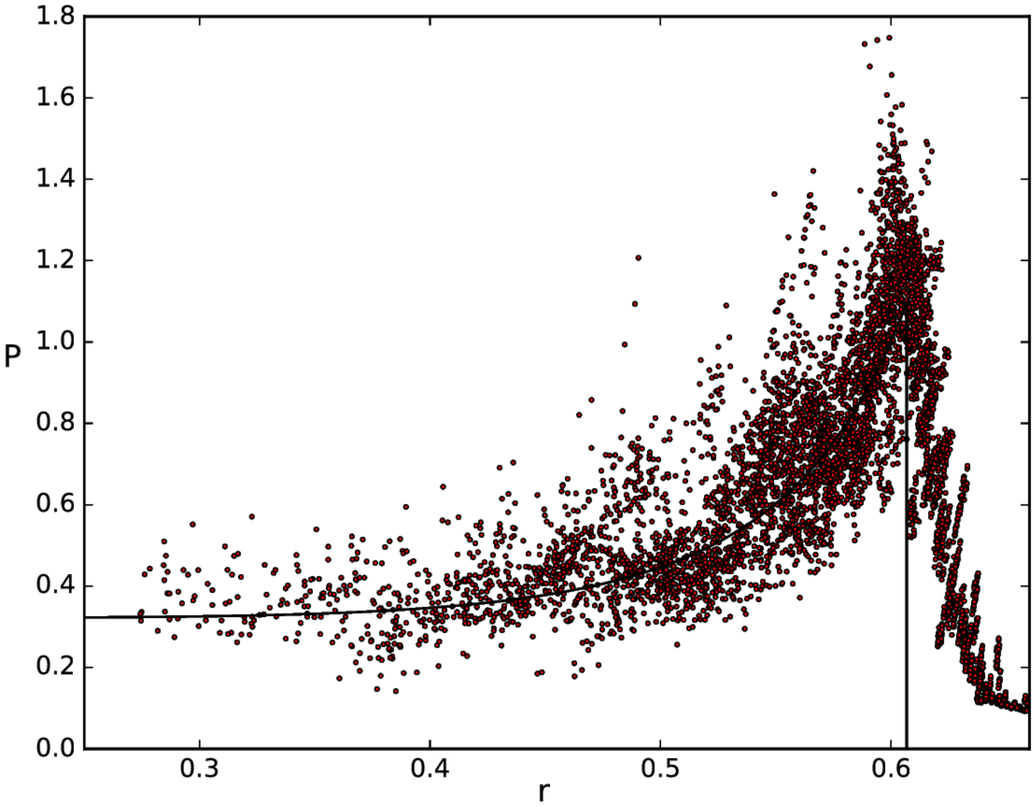

Figure 4.12. Sedov-Taylor blast wave test: Particles Pressure in function of the radial distance from the explosion point. t=0.2 . Red dots represent the numerical result of the test, black continuous line is the expected theoretical solution.

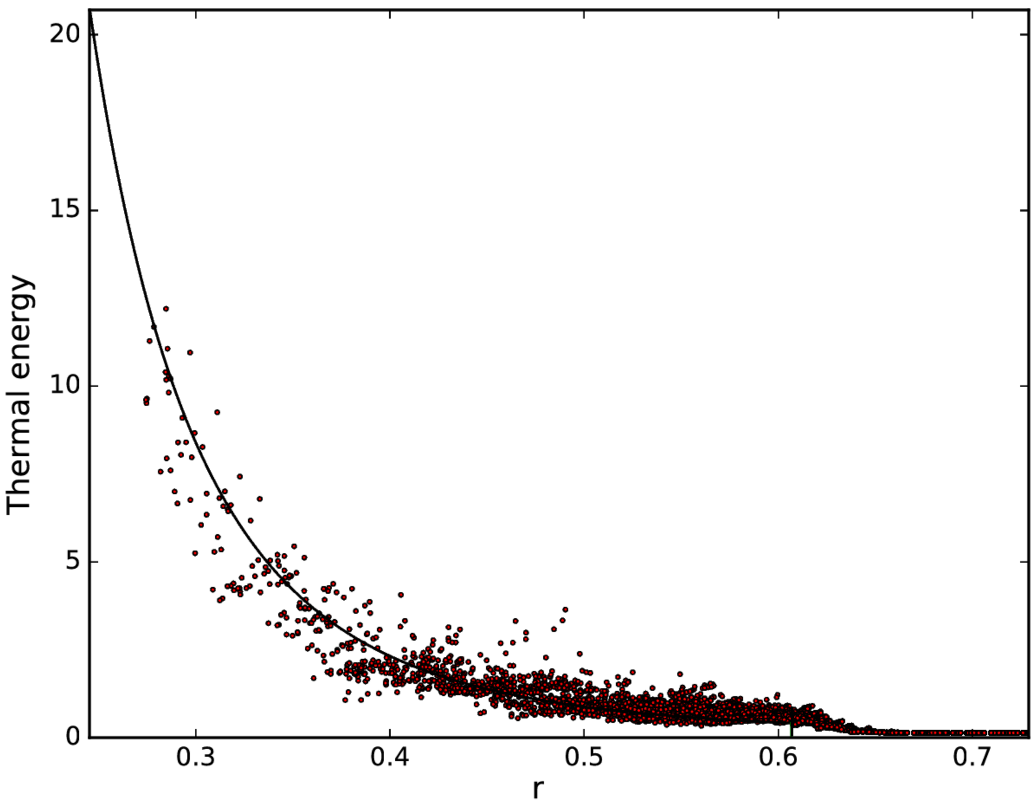

Figure 4.13. Sedov-Taylor blast wave test: Particles internal Energy in function of the radial distance from the explosion point. t=0.2 . Red dots represent the numerical result of the test, black continuous line is the expected theoretical solution.

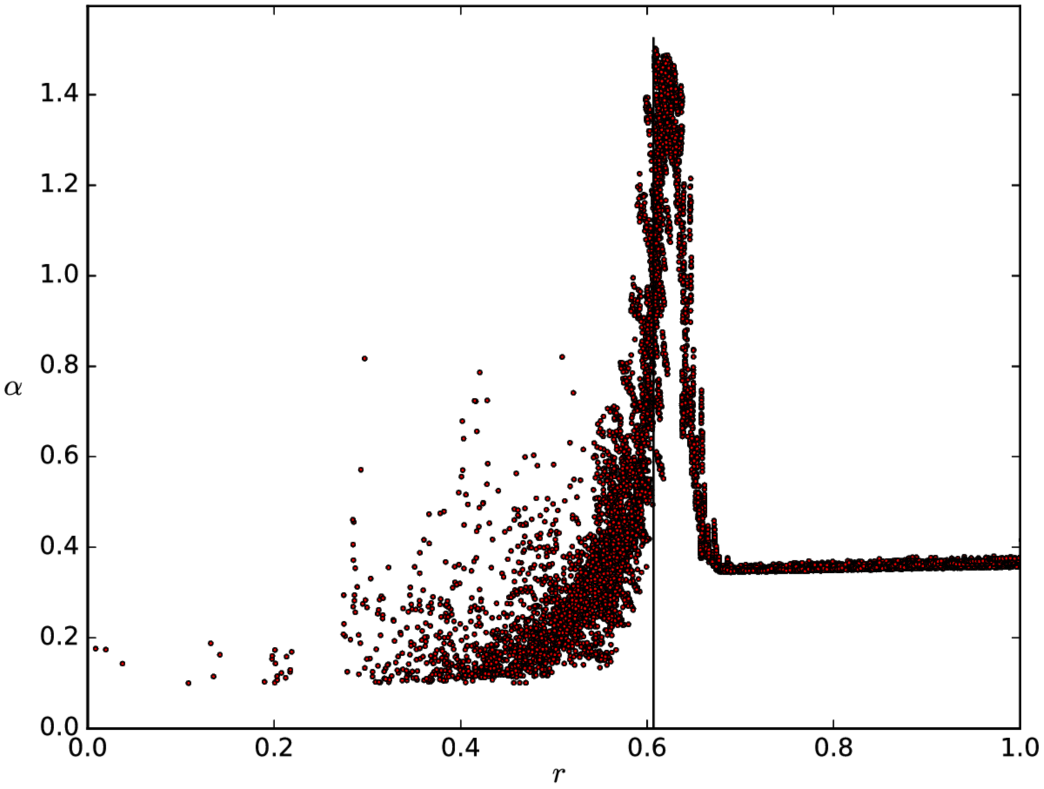

Figure 4.14. Sedov-Taylor blast wave test: numerical result of the SPH viscosity coefficient α in function of the radial distance from the explosion point. t=0.2. The vertical black line indicates the abscissa of $r_s(t = 0.2)$.

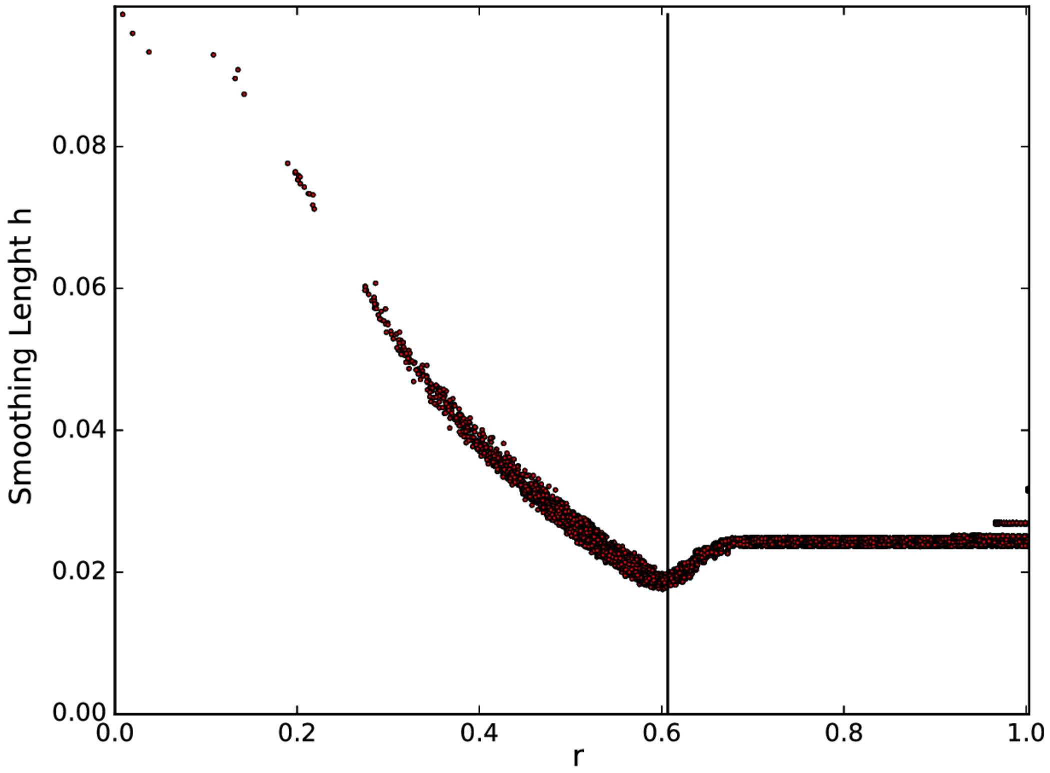

Figure 4.15. Sedov-Taylor blast wave test: numerical result of the smoothing length h in function of the radial distance from the explosion point. t=0.2. The vertical black line indicates the abscissa of $r_s(t = 0.2)$.

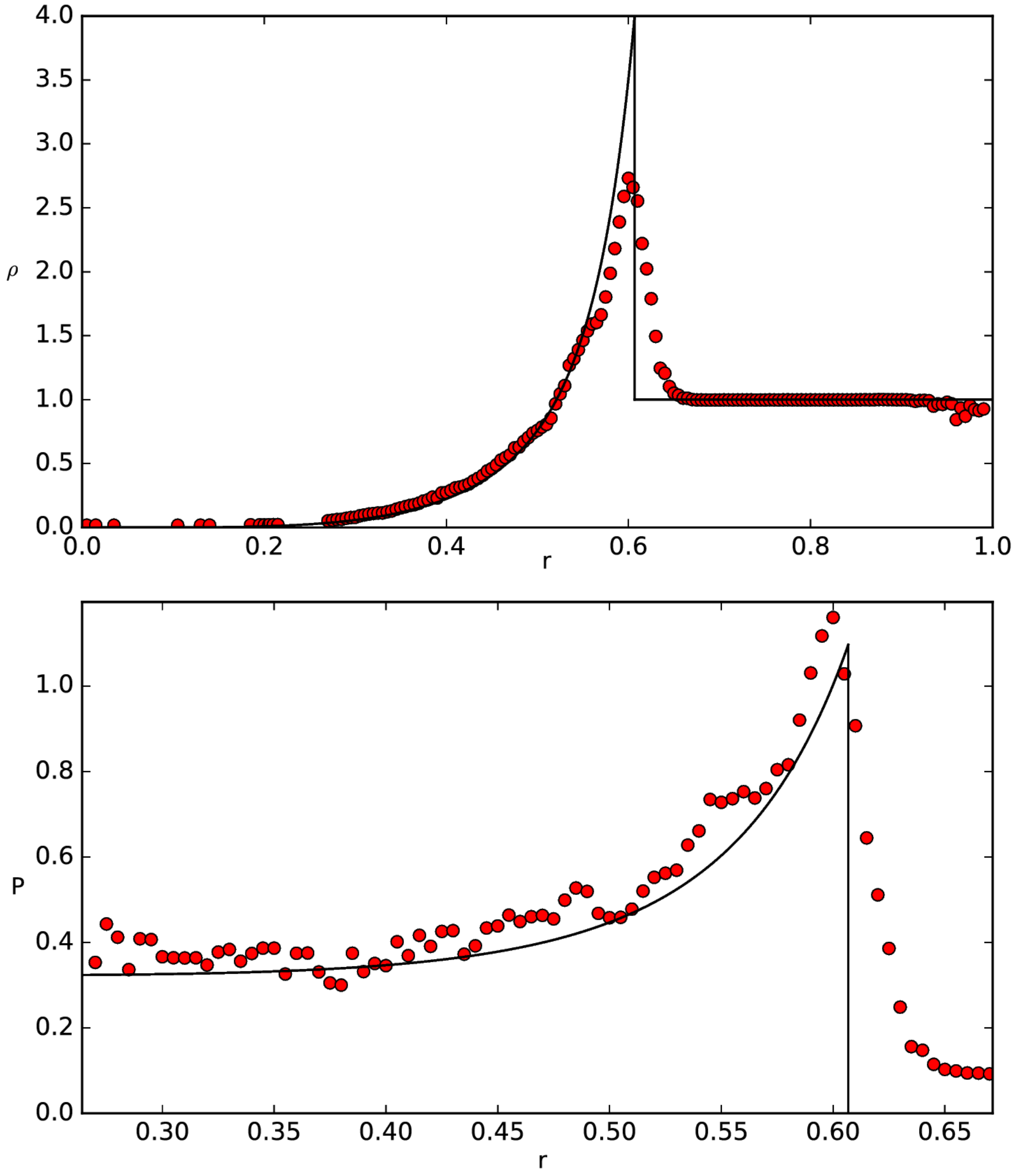

Figure 4.16. Sedov-taylor blast wave solution at t=0.2. On the top: average radial density in function of r. On the bottom panel: average pressure radial profile. Full line represents the analytical solution. Dots refer to the numerical results.

4.2 Code scalability and shared memory parallelization

We performed several tests in order to verify the scalability of our program, both with uniform-density systems and with non homogeneous distributions of matter (Plummer distributions). Tests have been made with a multi-threading Intel i7-4710HQ architecture with 8MB of cache memory. In figure 4.17, the total cpu-time (in seconds) needed for a single force evaluation is plotted in function of particle number N, performed on an homogeneous sphere. In horizontal axis, $N \cdot \log N$ is represented, normalized to a reference value $10^4 \cdot \log 10^4$. A value of $\theta = 0.6$ was used for the tree code scheme. Red dots represent the total CPU-time needed to compute the acceleration of a gas, the field is evaluated by descending the tree once and calculating both the hydrodynamics and the gravitational contributions. Before the acceleration routine, SPH spends an extra amount of time for neighbourhood searching and for the density evaluation. During the neighbourhood searching phase, depending on the dynamics and complexity of the system, as well as on the initial smothing lenght, each particle may require several iterations before obtaining the convergence, following the prescription 3.13. For homogeneous sphere and plummer sphere we found that, after a preliminary adjustement phase, the average number of iterations per particle was close to 1, and the total time taken by the density routine was linear in N. Taking into account density routine and acceleration routine, the overall time-machine per single step is plotted in the same figure (red triangles). Making a work profiling, through fully separating the workload of the gravitational calculus from the effort needed to make SPH evaluations, would be an impossible task. Indeed, for the sake of efficiency, hydrodynamics interactions are calculated at the same time with the long range particle-cube interactions, performing just a single tree descent. Furthermore, the two operations are not indipendent and interfere with each other because it may happen that far cubes (which the tree-code would approximate with quadrupole) fall within the smoothing length. In this case the algorithm makes a direct particle-particle coupling even for gravity, forgetting about the pure tree-code scheme. Thus, it is not possible to build an exact work profiling for the algorithm by simply separating the time interval taken by tree gravity part from the one taken by hydrodynamics calculations. Thus, we can only extimate the algorithm efficiency by testing on a pressureless system without using any softening lenght ϵ, or simply by using gas and setting h to zero. In figure 4.17, blue dots show the performances obtained for a simple gravitational field extimation, their behaviour is expected to be linear.

Based on the results of figure 4.17 , table 4.1 shows the work profiling percentage of the total time taken by a single force step. Pure tree code time, as explained before, has been obtained by doing simulation in which smoothing lenght h was set to zero. Subtracting the latter time quantity from the cpu-time taken to calculate force by "turning on" SPH, one obtains the hydrodynamical overhead for the acceleration routines. Furthermore, we take into account the percentage of time requested by the iterative neighbourhood searching cycles, which is shown too. Time values shown in 4.1 contains tree-building costs too, whose expected behaviour is proportional to

N	10^4	$5 \cdot 10^4$	10^5	$5 \cdot 10^5$	10^6	$2 \cdot 10^6$
Pure tree code.	37.0	38.7	34.6	41.7	45.4	48.3
SPH overhead.	26.5	32.4	35.8	29.9	26.4	24.4
Neighbour searching.	31.7	25.4	26.7	25.7	25.3	24.5
Tree building.	3.8	2.4	1.9	1.7	1.8	1.7
Other operations.	<1	<1	<1	<1	<1	<1

Table 4.1. Work profiling for a uniform sphere, $\theta = 0.6, N' = 50$: percentage of workload needed by bare tree gravitational routines, SPH overwork, neighbourhood searching, tree mapping and other operations; results for several values of particles number N are shown.

$N \cdot \log N$. Nevertheless, they give a small contribution to the overall time. It is worth to remark that, despite some fluctuation for low N numbers, the percentage of extra effort, needed through introducing SPH operations, decreases with the increasing of N. On the other hand, the iterative searching algorithm takes a time proportional to N. Nevertheless, inside the tree descent subroutines, the addition of SPH softened force evaluation along with the particle-cluster coupling, both with hydrodynamical terms extimation, requests a considerable amount of extra time machine.

This difference is not univocal and depends on the shape and density distribution of the system considered. Similarly to the previous graph, figure 4.18 illustrates the code performance for a plummer sphere distribution built with core radius $R_0 = 0.5$ and cutoff radius $R_C = 2.5$, with $\theta = 0.6$. Despite the gravitational tree code requests a cpu time $\approx N \cdot \log N$, the performance of the algorithm, at the same N, gets worse with respect to the previous model (a comparison is illustrated by figure 4.19). This is due to the fact that in Plummer system we have higher density contrast with respect to the case of homogeneous sphere. Thus, the algorithm has to deal with more subdivisions levels L, which are responsible for the logarithmic factor that governs the behaviour of the calculus time. On the other hand, SPH overwork time does not increase substantially (apart some fluctuations), because each particle needs just a local amount of informations given by a fixed number of close particles, neglecting the points above the smoothing kernel support. The combination of these two behaviours leads to the reduction of the ratios between hydrodynamical efforts and gravitational workload (see table 4.2 related to the distribution of workload for the plummer profile).

Figure 4.21 compares the performance of the code, for plummer model, for

N	10^4	$5 \cdot 10^4$	10^5	$5 \cdot 10^5$	10^6	$2 \cdot 10^6$
Pure tree code.	49,8	45,1	45,7	52,5	55,4	57,2
SPH overhead.	21,5	30,7	29,5	22,1	19,8	19,3
Neighbour searching.	24,8	21,1	22,1	22,8	22,1	20,9
Tree building.	3.0	2.1	1.7	1.5	1.7	1.6
Other operations.	<1	<1	<1	<1	<1	<1

Table 4.2. Work profiling for a plummer profile, $\theta = 0.6, N' = 50:$ as in table 4.1 percentage of workload needed by bare tree gravitational routines, SPH overwork, neighbourhood searching, tree mapping and other operations; results for several values of particles number N are shown.

$\theta = 0.25$ N	10^4	$5 \cdot 10^4$	10^5	$5 \cdot 10^5$	10^6	$2 \cdot 10^6$
Pure tree code.	85.8	87.7	88.4	90.2	93.7	93.0
SPH overhead.	5.0	6.1	5.9	5.3	1.9	2.9
Neighbour searching.	7.4	4.7	4.4	3.3	3.1	2.9
Tree building.	0.9	0.4	0.3	0.2	0.2	0.2
Other operations.	<1	<1	<1	<1	<1	<1
$\theta = 0.4$						
Pure tree code.	71.4	73.0	74.5	78.8	76.9	83.5
SPH overhead.	10.2	12.3	11.1	9.1	11.0	4.8
Neighbour searching.	15.6	12.5	12.4	10.4	10.3	9.9
Tree building.	1.9	1.3	1.0	0.7	0.8	0.8
Other operations.	<1	<1	<1	<1	<1	<1

Table 4.3. Work profiling for a plummer profile, for low values of opening angles $\theta = 0.25$ and $\theta = 0.4; N' = 50:$ as in previous tables, percentage of workload needed by bare tree gravitational routines, SPH overwork, neighbourhood searching, tree mapping and other operations; results for several values of particles number N are shown.

$\theta = 0.8$ N	10^4	$5 \cdot 10^4$	10^5	$5 \cdot 10^5$	10^6	$2 \cdot 10^6$
Pure tree code.	32.2	26.2	27.7	31.1	33.3	34.8
SPH overhead.	30.7	43.9	42.5	36.4	34.3	33.5
Neighbour searching.	32.2	26.4	26.7	29.6	29.3	28.6
Tree building.	3.8	2.5	2.2	2.0	2.1	2.1
Other operations.	<1	<1	<1	<1	<1	<1

$\theta = 1.0$						
Pure tree code.	21.1	18.8	16.2	18.6	19.0	21.6
SPH overhead.	32.1	48.8	50.5	44.9	45.6	42.8
Neighbour searching.	42.1	28.4	30.0	33.4	32.2	32.2
Tree building.	3.7	3.0	2.3	2.1	2.2	2.3
Other operations.	<1	<1	<1	<1	<1	<1

Table 4.4. Work profiling for a plummer profile, for high values of opening angles $\theta = 0.8$ and $\theta = 1.0; N' = 50:$ as in previous tables, percentage of workload needed by bare tree gravitational routines, SPH overwork, neighbourhood searching, tree mapping and other operations; results for several values of particles number N are shown.

different opening angles θ. Triangles represent the whole cpu-times for an acceleration estimation both with hydrodynamical force and with preliminary ρ calculation, while dots represent the pure gravitational code. The more the opening angle, the less the amount of operations done by the routines: cubes are coupled with particles even for shorther mutual distances, thus more direct particle-particle interactions are neglected. With lower opening angles, linearity is still followed for $\theta = 0.4$, while for $\theta = 0.25$ we have a deviation. Clearly, in the limit of $\theta \to 0$, the algorithm tends to reproduce the behaviour of a pure N body code, with calculus time proportional to N^2. With higher θ, code performance gets higher and higher for the bare gravitational computation, but when we consider full SPH efforts, the situation changes and the time needed for calculus does not decrease deeply. This is due to the fact that, as was explained before, algorithm is forced to make direct interaction with particles lying in the kernel dominium, even at those distances at which pure gravitational algorithm would use quadrupole approximation. Thus, SPH algorithm puts a lower limit to the code performance. On the other hand, when we use sufficiently high values of θ, the code uses quadrupole approximation only for cubes not included in the kernel dominium, so the closest particle undergo direct interaction, wheter we use a mere self-gravitational evaluation or gravitational plus hydrodynamical computations. This is the reason why the percentage of hydrodynamical workload decreases whith higher θ (table 4.3 and table 4.4 summarise the ratio distribution of work at various opening angles, related to the plummer system). Furthermore, times taken by the density subroutine are indipendent from the choise of the opening angle because they act locally, but theyr ratios (as shown in tables 4.3, 4.4) decreases with θ, because gravitational efforts became more and more dominant. Linear behaviour of neighbourhood searching routines is illustrated in figure 4.20 (results for plummers profile are shown).

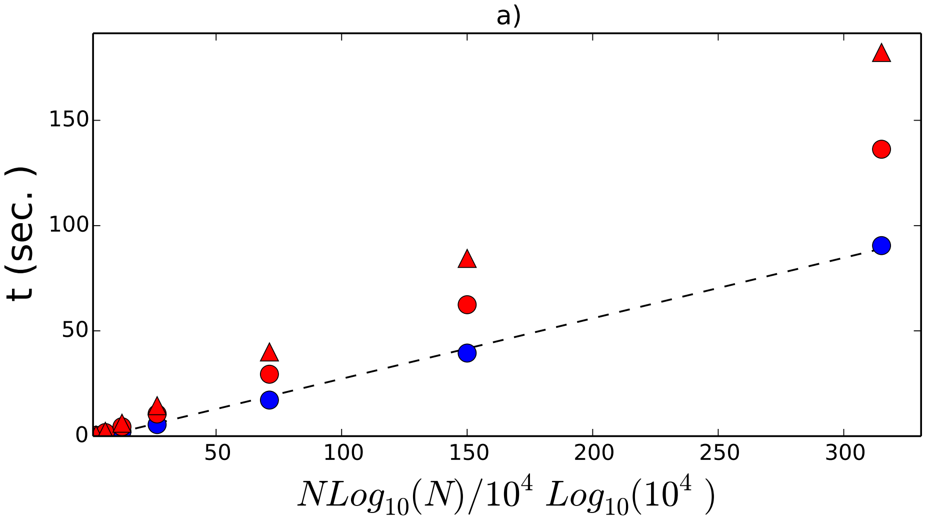

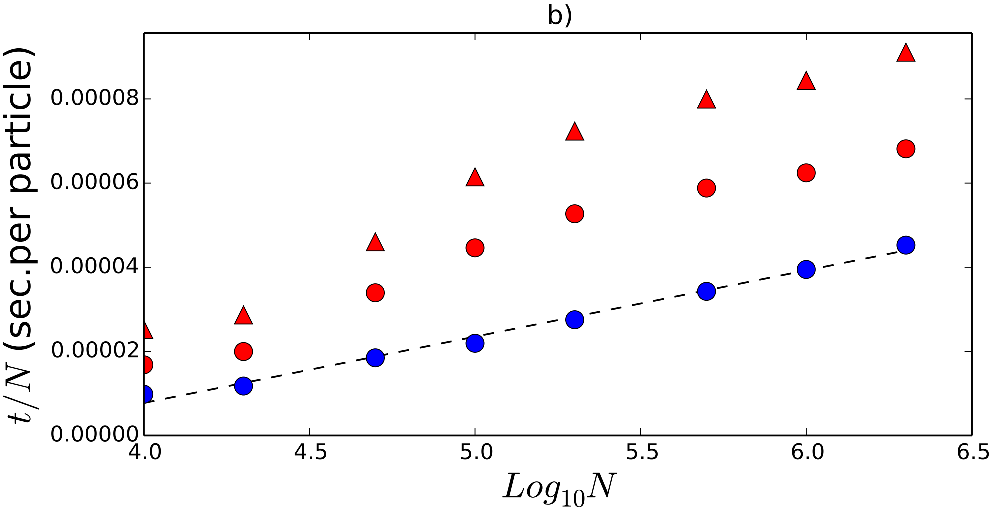

Figure 4.17. (fig. a) CPU Tree descent time in function of $N \log N$ - normalized to $N_0 \log N_0$; $N_0 = 10^4$ - for a uniform sphere. $\theta = 0.6$. Comparison among pure self-gravity evaluation (blue dots), gravitational plus hydrodynamical calculations(red dots), overhead due to neighbourhood searching with 1 iteration per particle (triangles).(fig. b) Same results expressed in time(seconds) per particle - $\log N$

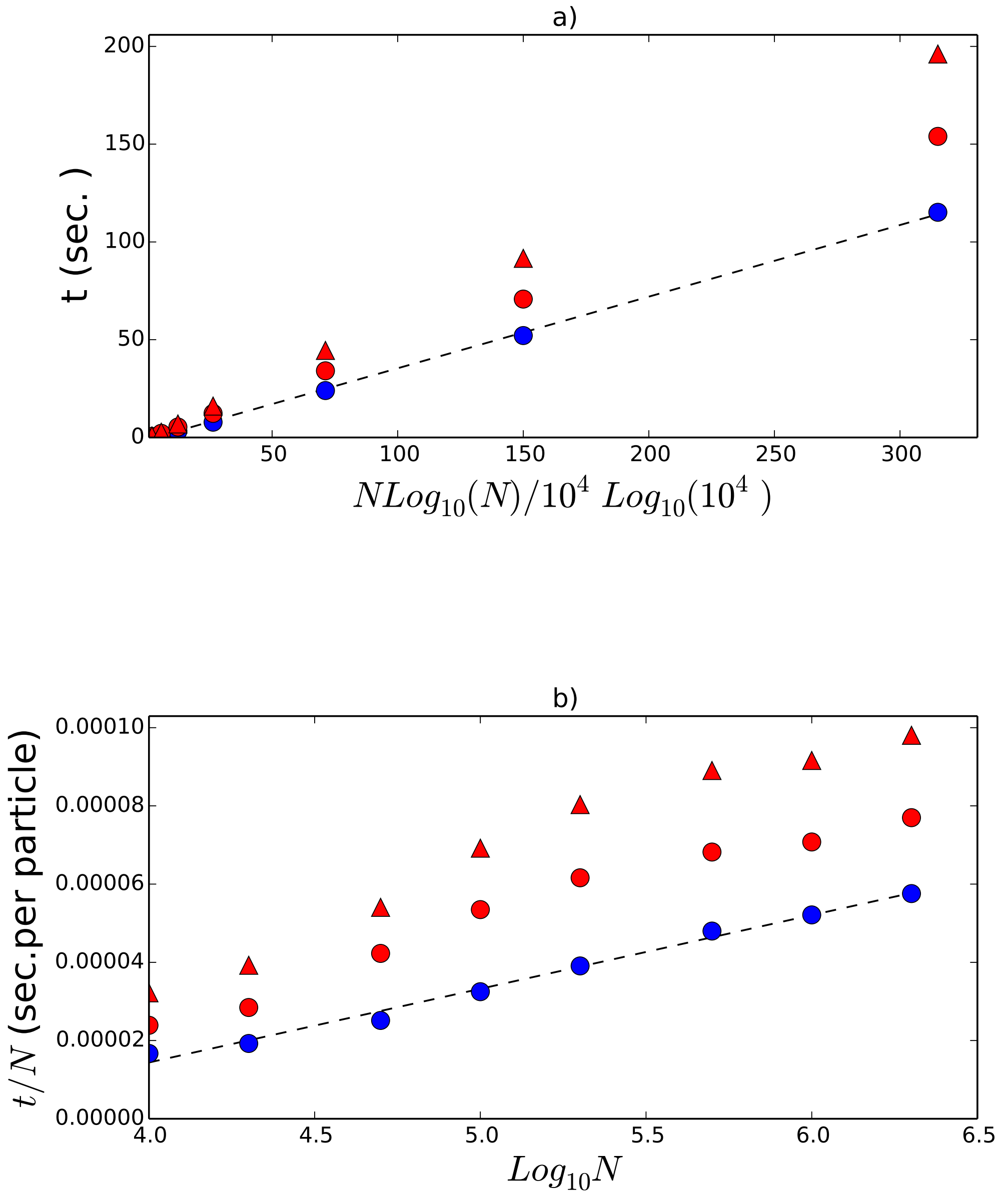

Figure 4.18. Plummer profile; $\theta = 0.6$. (fig. a) CPU Tree descent time in function of $N \cdot \log N$ - normalized to $N_0 \cdot \log N$; $N_0 = 10^4$ - . Comparison among pure self-gravity evaluation (blue dots), gravitational plus hydrodynamical calculations(red dots), overhead due to neighbourhood searching with 1 iteration per particle (triangles). (fig. b) Same results expressed in time(sec.) per particle - $\log N$

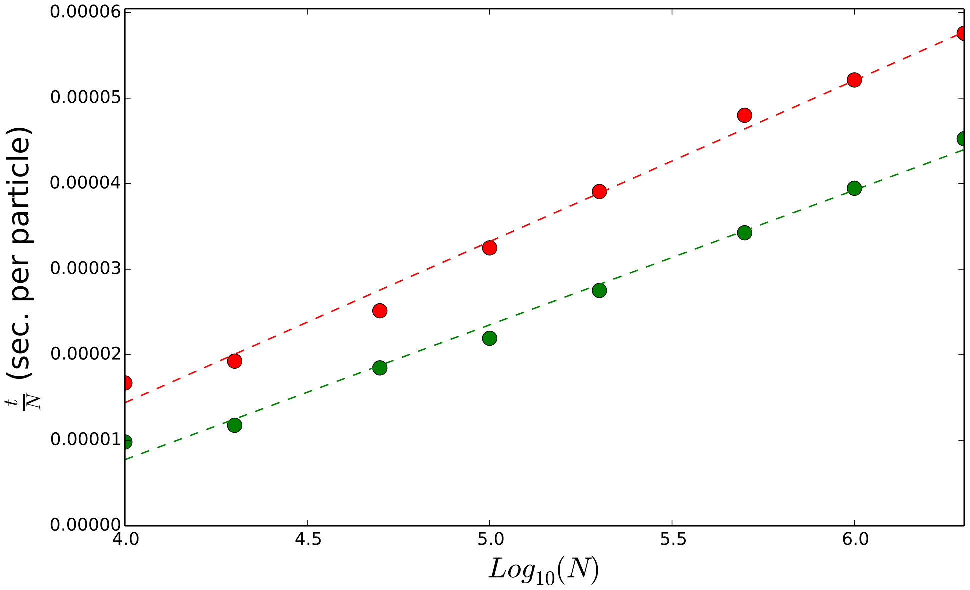

Figure 4.19. Tree gravitational code performance: comparison between uniform sphere(green dots) and Plummer profile(red dots). $\theta = 0.6$, units: seconds per particle v.s. $\log N$

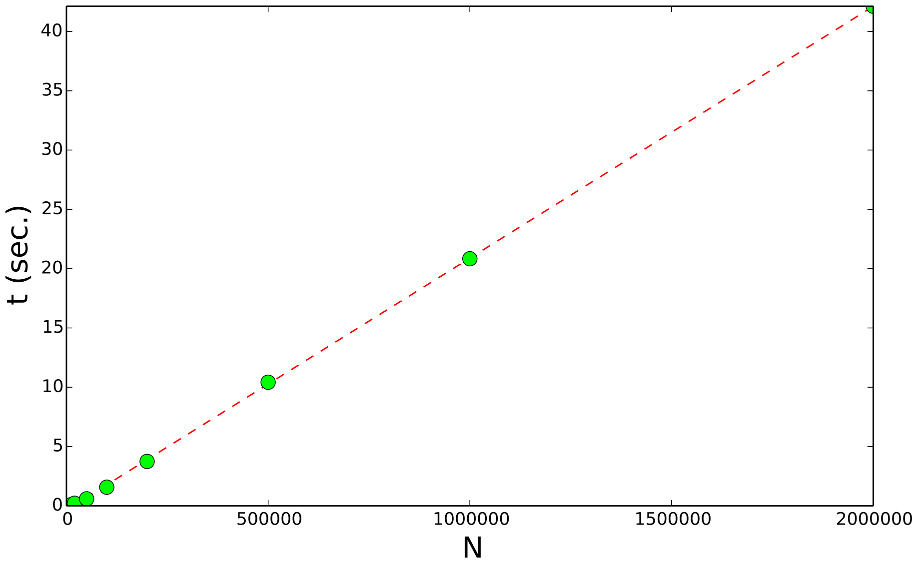

Figure 4.20. Linear behaviour of CPU-time for neighbour searching routine (Plummer profile)

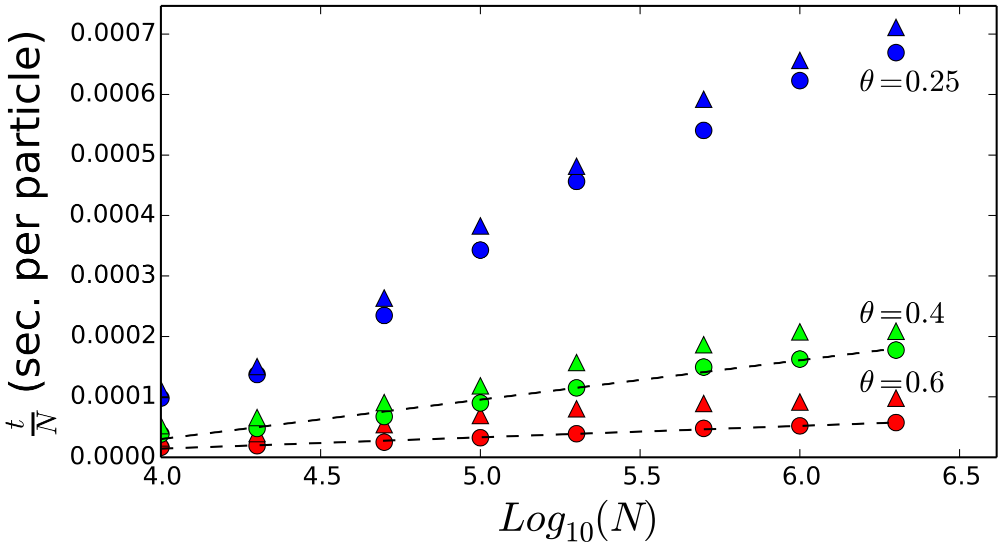

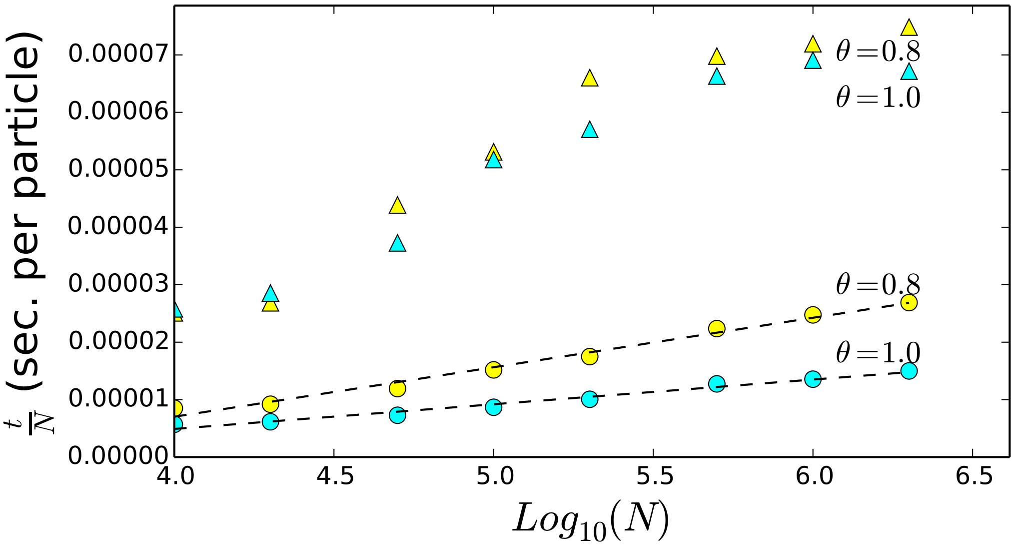

Figure 4.21. Plummer sphere, code performance at various θ, calculus time per particle vs. $\log N$). Tree gravitational algorithm(dots) and full SPH algorithm (triangles)

Chapter 5

Evolution of circumstellar disks

Here we show some investigations on protoplanetary disks in equilibrium around one star, illustrating also some general prescriptions adopted to build disks to be used in a wide class of context. Here we introduce two main application which characterizes our work activity: secular dissipation of protoplanetary disks in a pseudo-equilibrium state around a star, and perturbation of disks by passing-by star. The latter constitutes a first parametric approach of a complex problem: the evolution of disks in star clusters, it involves the treatement of hybrid Gas + Nbody systems.

5.1 SPH schematization of the *Shakura-Sunyaev* viscosity

As discussed in section 2.2, in a Keplerian disk the turbulence dissipates the kinetic energy emualating the effects of a pseudo-viscosity. To take such effect into account we would need some dissipative term compatible with the eulerian equations, i.e. different from the classical Navier Stokes molecular dissipation force. The SPH artificial viscosity 3.21 is well suited to face such issue. Meglicki et al. (1993) found that the SPH viscosity coefficient α provides a viscous acceleration with an effective kinematic viscosity ν :

$$\frac{d\vec{v}}{dt}|_{visc} = \nu\vec{\nabla}\cdot\vec{S} \propto \frac{\alpha\ h}{2\rho}\{\vec{\nabla}(c_s\rho\vec{S}) + \vec{\nabla}(c_s\rho\vec{\nabla}\cdot\vec{v})\}$$

containing a shear viscosity as first term, and a bulk viscosity as second addend; S represents a momentum transport tensor with components $S_{[ij]} = \frac{\partial v_{[i]}}{\partial x_{[j]}} + \frac{\partial v_{[j]}}{\partial x_{[i]}}$. The constant of proportionality is a function of the number of dimensions d considered and the smoothing kernel. Provided we use a cubic spline function(3.11) we can show that the effective kinematic viscosity in the SPH formalism assumes the following form:

$$\nu = \delta_v \alpha c_s h \tag{5.1}$$

with δ_v an appropriate coefficient of proportionality dependent on the dimension of the problem. In several works (as in Artymowicz and Lubow (1994), or Nelson et al. (1998)) a special prescription is used for the viscosity, acting no more only for approachin particles, but also for points which move out (with $\vec{r}_{ij} \cdot \vec{v}_{ij} > 0$). Hence, it tourns out that $\delta_v = \frac{1}{2(d+2)} = \frac{1}{10}$ for 3D systems. On the other hand, adopting the classical SPH approach with α switched on just for particles moving in, Meglicki et al. (1993) showed that the kinematic viscosity decreases by a factor $\frac{1}{2}$ (see also Meru and Bate, 2012, for a deep explanation). Using the 2.6, we obtain an expression of the Shakura-Sunyaev viscosity coefficient:

$$\alpha_{SS} = \delta_v \alpha \frac{h}{H} \tag{5.2}$$

To investigate 3-dimensional disks in equilibrium around a star, we adopted the approach mentioned above and turned on the viscosity whatever $\vec{r}_{ij} \cdot \vec{v}_{ij}$ is positive or negative, thus we have a kinematic effective viscosity of the form $\nu = \frac{1}{10}\alpha_{SS}H$. This peculiar modification of the SPH viscosity formalism provides a more realistic prediction of the effect given by a kinematic viscosity since it acts under compressions or under gas expansions, but is valid as far as we don't deal with strong velocity gradients, i.e. shock waves for instance. Indeed, the classical Morris and Monaghan (1997) amplification law (3.24) would generate high dissipative forces, expected only for approaching particles. Nevertheless, circumstellar disks, in perfect equilibrium or in a perturbed state, are not expected to undergo such huge compressions to let strong shock waves arise.Thus, we would not need the Morris-Monaghan terms to amplify α. Lodato and Price (2010), for example, in investigating the evolutions of warps in thin disks around binary stars, used a similar prescriprion for the SPH viscosity by turning off the Morris-Monaghan term and keeping a constant low value of $\alpha << 1$, active for both compressions and expansions. Typical values used for the viscosity coefficient are $0.05 \div 0.1$, we use $\alpha = 0.1$ in our models.

5.2 General disk setup and dissipation timescales

Here we show some test related to the long-term viscous evolution of gaseous disks in a radially isothermal equilibrium around one star. In order to build disks in equilibrium, we must set a thermo-kinetic configuration such as the dynamic and the pressure of ther gas keep the disk stable under gravitational perturbations. Several numerical works (see for example Mayer et al., 2002, Boss, 1998, 2003) worked out some extimation of the gravitational collapse timescales in a protoplanetary disk, being of the same order of its dynamical time. They have showns that, under certain conditions, matter can undergo instabilities and eventually condense forming clumps in $10^3 \div 10^4$ yr, far less than the typical viscous timescales (2.7). The equilibrium condition for a disk is given by the well-known Toomre's criterium:

$$Q = \frac{c_s \Omega_e}{\pi G \Sigma} > Q' \tag{5.3}$$

where Ω_e represents the epicyclic frequency, approximatively eqivalent to Ω_k for keplerian disks (see Binney and Tremaine, 1987, Toomre, 1964, for a detailed explanation). The Toomre's factor is a general coefficient which quantifies the predominance of the thermal and dynamical actions over the gravity: the more the gravitational collapse timescale, the more the Q factor. Several numerical investigations showed that the treshold Q' for the stability under gravitational collapse is about 1.5 for thin and light disks (with mass far less than the mass of the central star). In case of massive radially isothermal disks (with a disk to mass ratio $\approx 0.1 \div 1$) it has been found, for Q close to 1.5, a collapse and consequent formation of spirals which rapidly lead to destruction of the whole disk and a satisfying equilibrium condition with $Q \geq 2.2$ (see Pickett et al., 1998, 2000). We tested the secular dissipation of 3D SPH models of disks with $M_d = 0.01 M_\odot$ around $1 M_\odot$ star and, as discussed in paraghaph 2.2, we set up the gas particles in a cylindrical axisymmetric distribution (r, θ, z), such that the disk midplane lies in the (X,Y) plane, with the star placed at the origin. As illustrated by the equation 2.4, we adopted the Hayashi's fitted profile, typical of the Minimul Solar Mass Nebula, i.e. build the gas distribution according to the surface density $\Sigma \propto r^{-3/2}$. This means that SPH particles have been placed, with a montecarlo approach, according to the following number density:

$$n(r, \theta, z) \propto \rho(r, \theta, z) \propto \frac{\Sigma(r)}{H} \exp\left(-\frac{z^2}{2H^2}\right) \propto r^{-39/14} \exp\left(-\frac{z^2}{2H^2}\right)$$

Starting from the same basic configuration, we built tree different model of disks (hereafter we will refer to them as $D100$, $D200$, $D300$) by choosing different internal and external cut-off radius r_{int} and r_{disk}, with a constant ratio $\frac{r_{int}}{r_{disk}} = 0.1$. So, for the tree models we choosed respectively $r_{int} = 10AU$, $r_{int} = 20AU$. Figure 5.1(panel a) shows the initial configuration of the $D100$ disk , projected along the midplane. Figures 5.2 and 5.3 refer to the simulations $D200$ and $D300$.

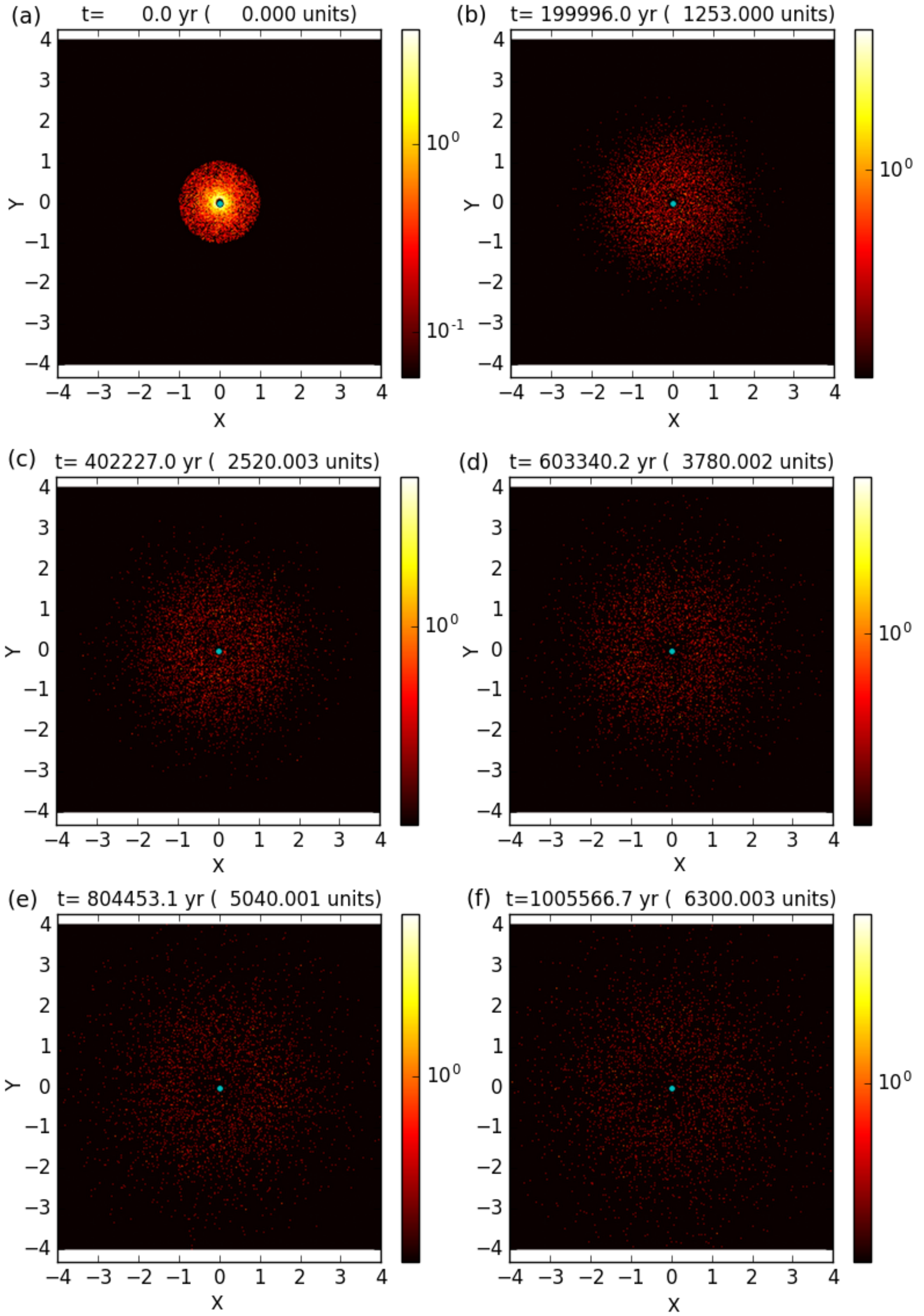

Figure 5.1. Run $D100$. Colour surface gas density map Σ projected on the midplane, evolution sequence from the initial conditions (panel a) to $6 \times 10^5 yr$ (panel e). N = 10^4. Units: 100 AU. Density map units = 885 $g \cdot cm^{-2}$.

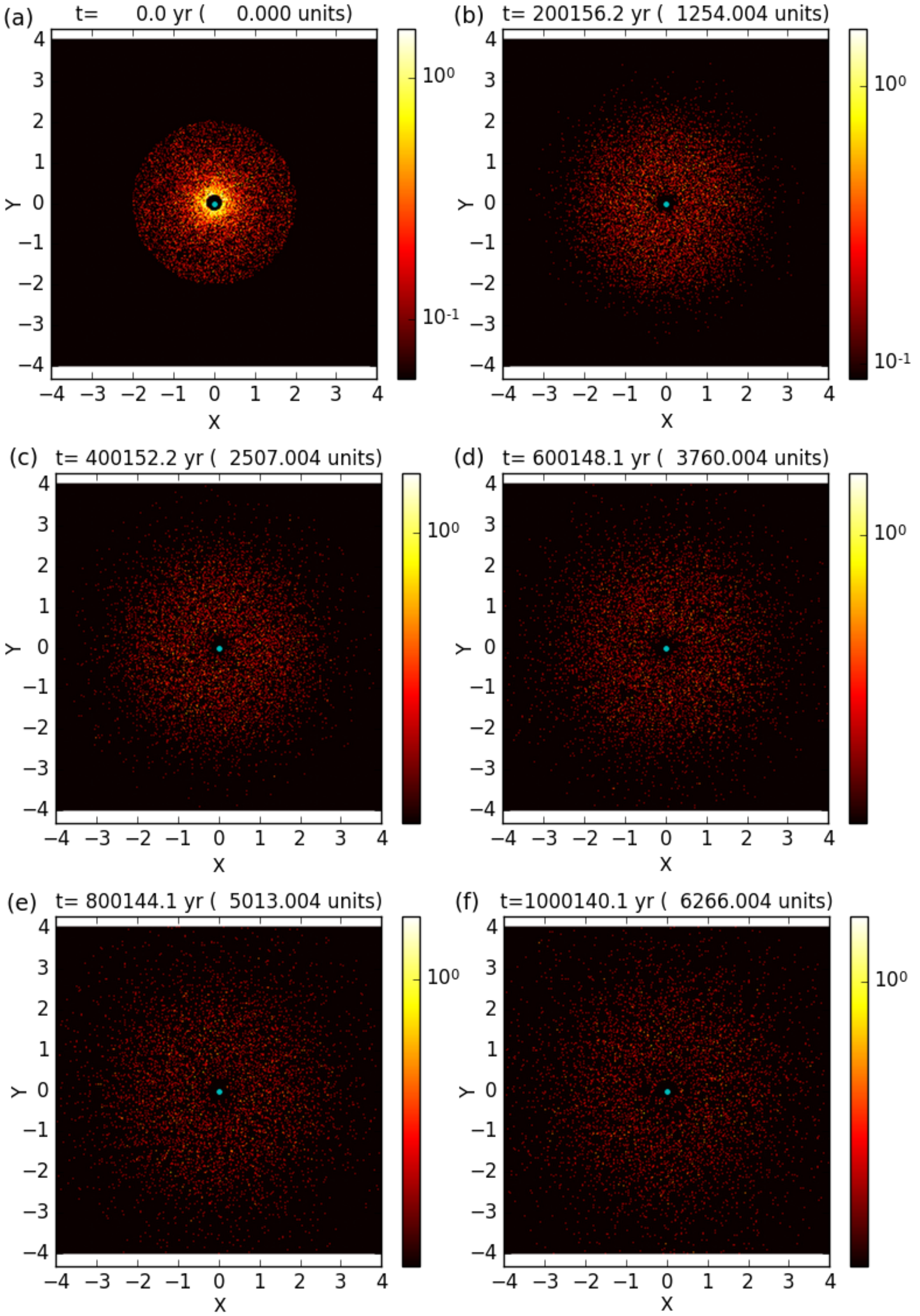

Figure 5.2. Run *D*200. Colour surface gas density map Σ projected on the midplane, evolution sequence from the initial conditions (panel a) to $6 \times 10^5 yr$ (panel e). N = 10^4. Units: 100 AU. Density map units = 885 $g \cdot cm^{-2}$.

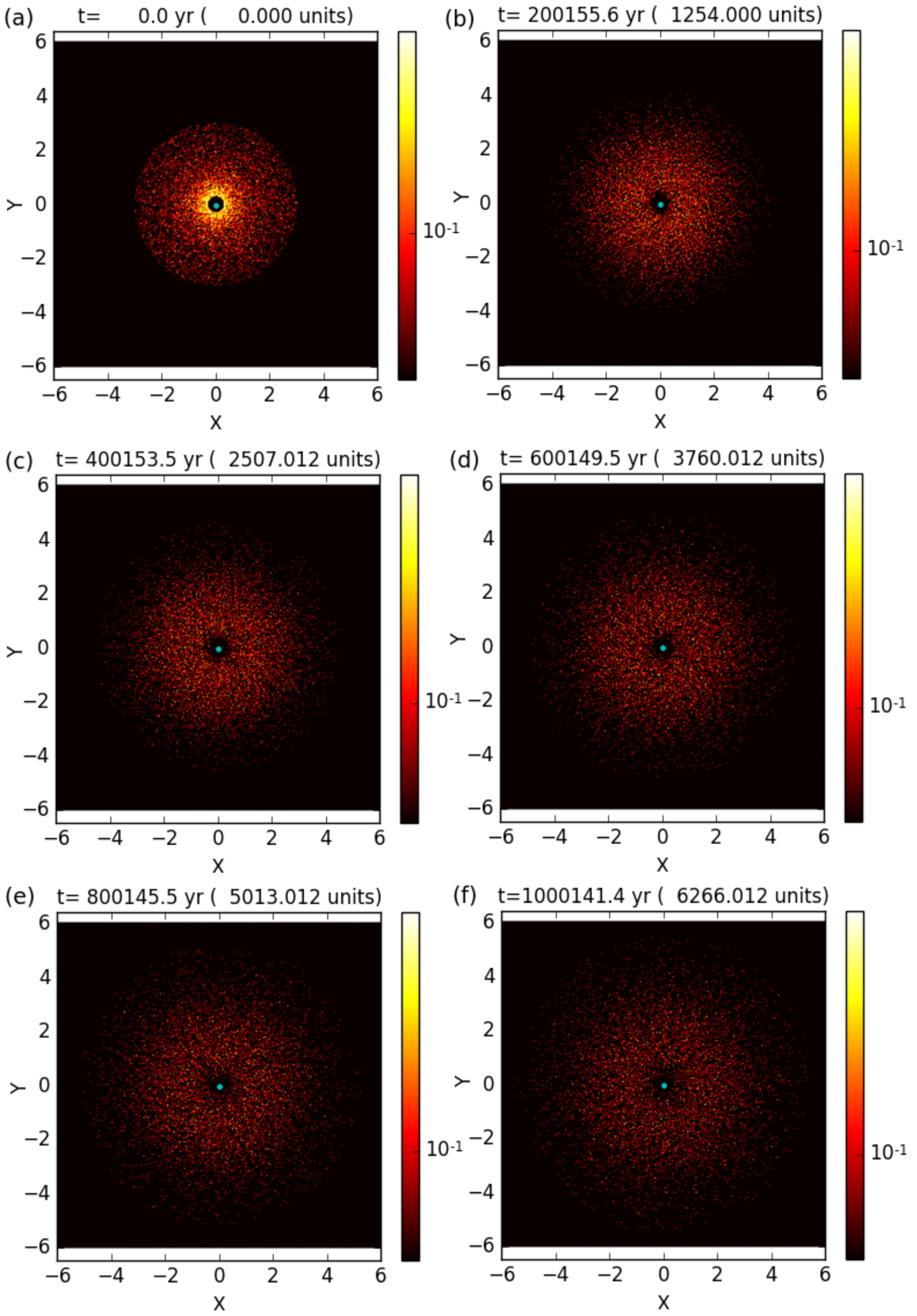

Figure 5.3. Run $D300$. Colour surface gas density map Σ projected on the midplane, evolution sequence from the initial conditions (panel a) to $6 \times 10^5 yr$ (panel e). N = 10^4. Units: 100 AU. Density map units = 885 $g \cdot cm^{-2}$.

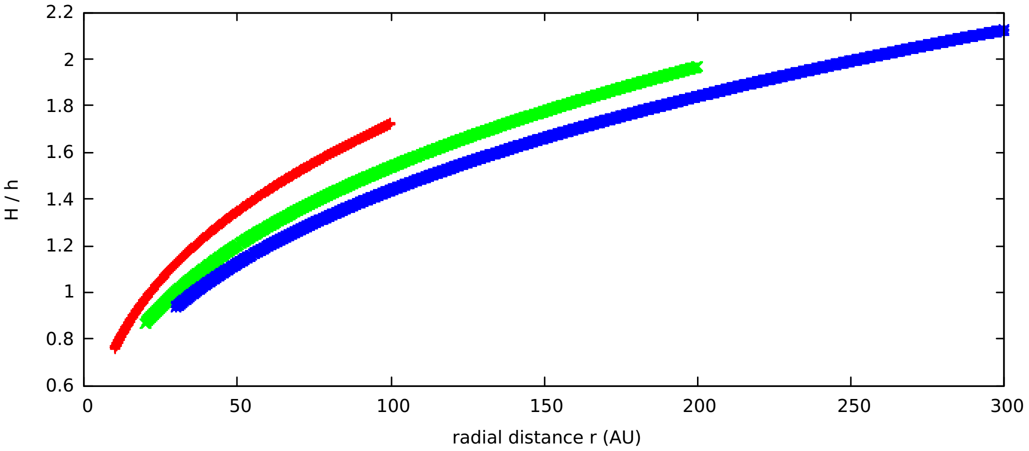

Figure 5.4. Expected ratios $\frac{H}{h}$ in function of r, for the three models of disks. D100 (red line), D200(green line), D300(blue line). Ratios below 1 are barely vertically resolved.

For each configuration, a sink radius for the central star was set: $r_{sink} = r_{int}$. For all the disks, the temperature has the following radial profile :

$$T = T_0 \left(\frac{r}{r_0}\right)^{-q} \tag{5.4}$$

with $q = -3/7$, $r_0 = 10$ AU and $T_0 = 100K$ calibrated to guarantee $Q >> 1.5$. We used, for each disk, a number of 10^4 particles. This choice, despite doesn't allow us to investigate in details on the internal structure of the disks, constitutes a sufficient approach to understand the global evolution of the system in terms of accretion rate, and it is usually a sufficient quantity to investigate on the equilibrium of such systems around stars. It can be shown that (see Lodato and Pringle (2007) and Lodato and Price (2010)) disks with a scale heigth to smoothing length ratio $H/h \geq 1.7$ are sufficiently resolved in 3 dimensions. Our disks, as shown in figure 5.4, have expected ratio even equal to unit, which means that they are barely resolved in the vertical direction. $D100$, $D200$ and $D300$ are expected to evolve with different timescales, as the kinematic viscosity, and thus α_{SS}, are functions of the scale heigth and the speed of sound. According to the simple schematization discussed in 2.2, equation 2.7 gives, we can evaluate, for our models, the typical viscous timescales which are constrained by the values in correspondence to the internal and external disk radii. Using an SPH artificial viscosity $\alpha = 0.1$, for $D100$ we have $\tau_\nu \in [9.2 \times 10^4, 1.8 \times 10^6]yr$. For the other two models $D200$ and $D300$, we have respectively $\tau_\nu \in [2 \times 10^5 yr, 3.8 \times 10^6 yr]$ and $\tau_\nu \in [3.2 \times 10^5, 6.1 \times 10^6 yr]$.

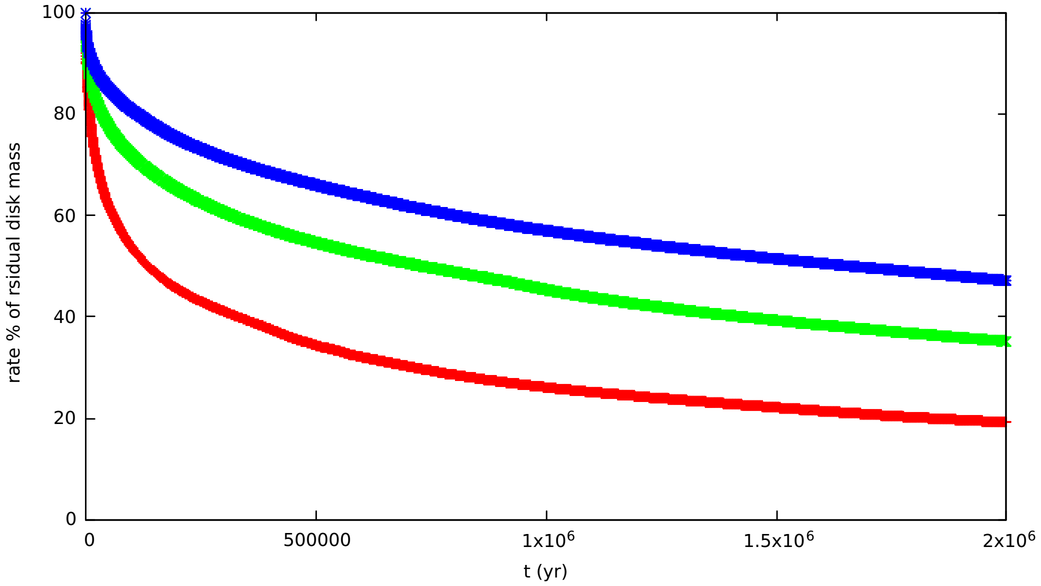

Figure 5.5. Residual percentage of disk mass (with respect to the initial value) in function of time, for models D100 (red line), D200(green line), D300(blue line).

One of the most suitable parameter to quantify the viscous evolution of disks is given by the inward flux of matter. Thus, the disk mass captured by the star during the evolution is a relevant quantity. We let evolve the systems for at least $2 \cdot 10^6$ yr; the Figure 5.5 shows the rate % of the disk mass which still revolves around the star. As it was expected, larger disks evolve slower and the central star accretes less mass and, after the first Myr, only the smallest disk has lost a considerable quantity of mass, far more than 50%.

The viscous evolution of disks is done in a simple way and the viscosity should be taken

In recent works on hydrodynamical protoplaentary disks, the isothermal profile has been modelled according to the 5.4 but with a different $q = 1.5$ (Lodato and Pringle, 2007, Martin et al., 2014, Rosotti et al., 2014, Lubow and Martin, 2016). At the base of such choice there are just numerical purposes, it's straightforward to show that, with a profile $T \propto r^{-3/2}$, H becames proportional to the smoothing length $h \propto r^{3/4}$. Hence the resolution factor H/h, together with α_{SS} turn to be constant all over the disk.

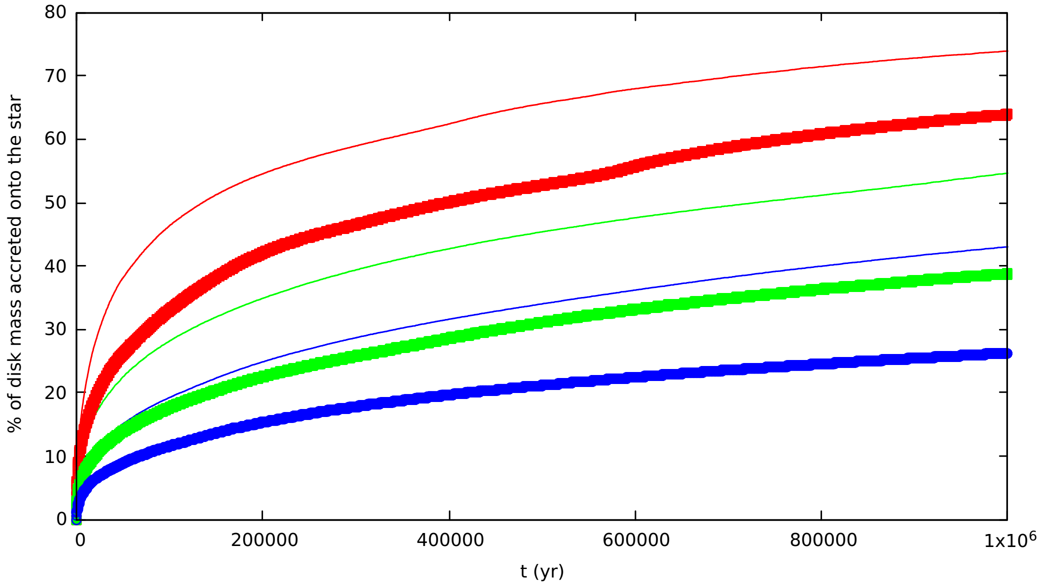

Figure 5.6. Disk mass accreted onto the star(with respect to the initial value) in function of time, for the same three models, with the modify isothermal profile, such as $c_s \propto r^{-3/4}$ (thick lines). Comparison with the original disks with $c_s \propto r^{-3/14}$(thin lines). Same color corresponds to the same radius R_{disk}. D100 (red line), D200(green line), D300(blue line).

Despite the idea to have a univocal definition of α_{ss} and an homogeneous resolution for a disk is fascinating, it may result unrealistic, for several reasons. Firstly, both the observations and the classical modellizations, as discussed in the chapter 2, suggest an isothermal profile with q close to 0.5 rather than 1.5, and a mere motivation based on numerical convenience sounds a poor argument. Secondly, α_{SS} should be rather than constant because the efficiency and the mechanism of the turbulence phenomena depend both on several environment conditions which may vary along r. Thirdly, but not less important, the different slope in the thermal profile may influence substantially the disk evolution, i.e. its survival timescale, a crucial parameter which can establish whether a proto-planet, once it has been formed by means of the slow-process of core accretion, is still embedded in a living disk and thus may capture gas. Figure 5.6 shows the rate % of disk mass accreted into the central star, referred to the same three models presented above, but with a slight modification in the thermal profile. We indeed set the temperature law as $T \propto r^{-3/2}$. The graph shows a different evolution with respect to the previous disks(thick lines), and a weaker accretion: the central star capture matter at shorter rates.

5.3 Disks perturbed by passing-by stars

As mentioned in the chapter 2, one of the most interesting mechanics of evolution of protoplanetary disks is due to the gravitational perturbation induced by other stars. If the star-disk system is embedded in a cluster, it may undergo large perturbations, as far as the other stars approach with sufficiently short distances. Despite a semi-analytical treatment of the disks is the dominant approach in the literature, a first full 3D hydrodynamical investigation on such process can be found in the work of Rosotti et al. (2014). Here, the dynamical evolution of 100 stars, 10 of which surrounded by a gaseous disk, was coupled with the gas hydrodynamics, in an hybrid SPH+direct-Nbody framework.

An important application for our code is addressed to face such problem, starting from a simple parametric approach. Following the model mentioned in the previous section, our code aims at investigating a simple model composed by a star plus a circumstellar gaseous disk in equilibrium against Jeans instabilities (i.e. $Q >> 1.5$). Such system is enriched by a second passing-by star(hereafter indicated as $S2$) which perturbs the equilibrium of the system and, as it would be expected, may accelerate the disk dissipation processes by enhancing the rate of flux of matter towards the first star (hereafter $S1$). A vicious approximation, necessary for our model, is applied to $S2$: the second star star doesn't emit radiation, and the thermodynamics of the gas is influenced just by the first star, following the standard isothermal law 5.4. For our purposes, we have built a basic starting condition, which mainly consist in a star $S1$ with mass $M_1 = 1M_\odot$, and the same disk $D100$ illustrated in the previous section. The disk, with $0.01M_\odot$, thus revolves in a keplerian equilibrium and starts its secular dissipative evolution. After an initial evolution of $2000 \div 3000yr$, $S1$ is approached by a second star $S2$, with mass $M_2 = M_1$, with an impact parameter and an initial velocity (approximately at infinite), parametrized respectively as b_s and $v_\infty \approx v_0$. The initial conditions for the system have been set placing the two stars with a mutual distance $\vec{r}_{12}(t = 0) = (b_s, d, 0)$, with $d >> r_{disk}$ and a relative velocity $\vec{v}_{12}(t = 0) = (-v_0, 0, 0)$, the trajectories of $S2$ and $S1$ are hence parallel to the disk midplane. Star $S2$ has a sink radius of 5 AU, equal to its softening radius. Our investigation consisted peculiarly in studying the intensity of the dynamical perturbations undergone by $S1$, and the effects on the accretion processes, for different scenarios, obtained modulating b_s and v_0. Generally we found that, with the same value of v_0, the strength of the perturbation is influenced by the impact parameter. Figure 5.7 illustrates the accretion of the disk mass onto the two stars in function of time, by analogy with the ratios found for isolated disks in the previous section, at fixed $v_0 = -1.5km \cdot s^{-1}$, for several values of b_s, ranging from 150 AU to 300 AU.

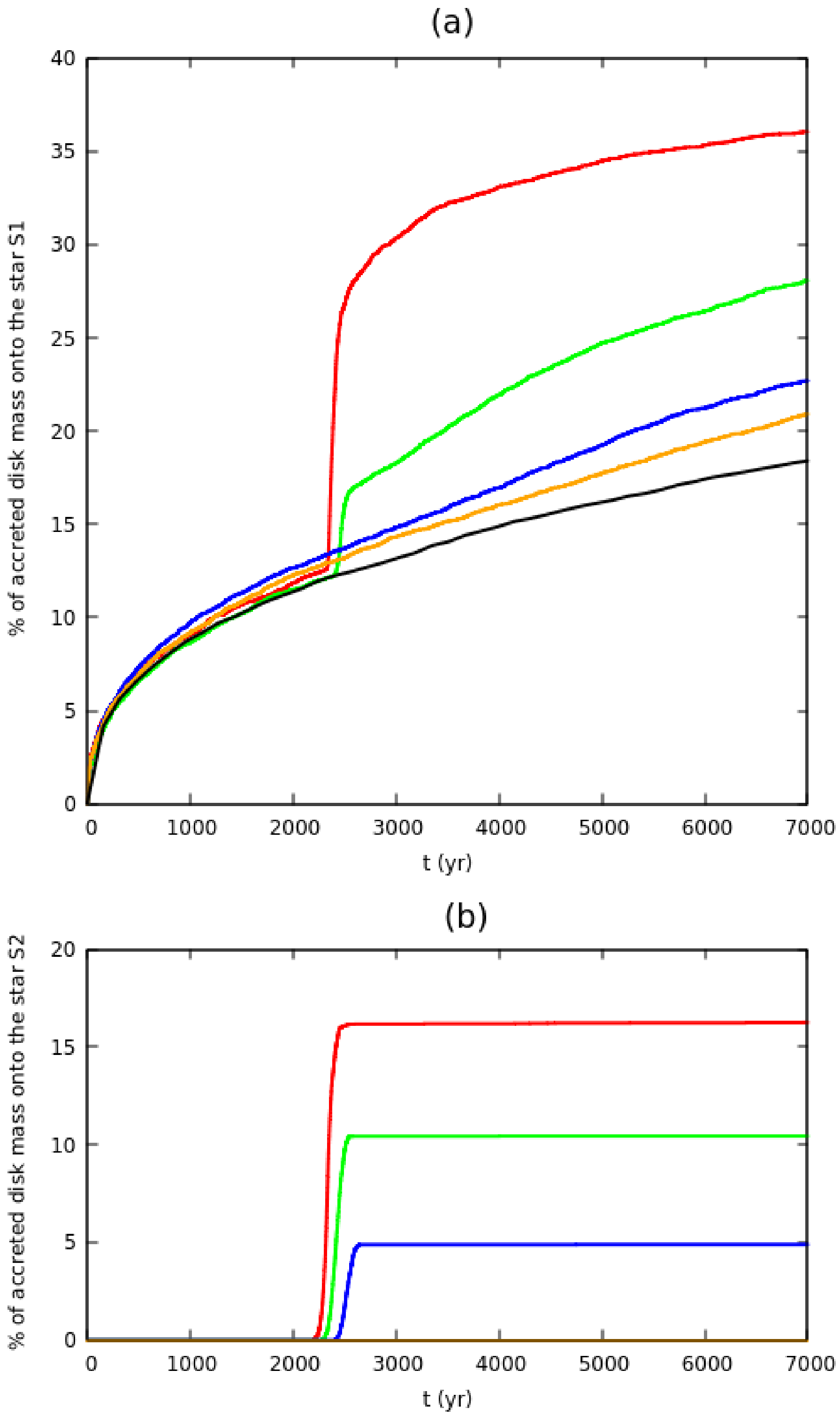

Figure 5.7. Disk mass rate % accreted onto the star $S1$ (top panel) and $S2$(bottom panel), after a close encounter with 2. Different curves represent different models with different impact parameters. $v_0 = -1.5\ km\ s^{-1} = cost$. red curve: ($b_s = 150AU$); green curve: ($b_s = 200AU$); blue curve ($b_s = 250AU$); orange curve ($b_s = 300AU$). The black line (panel a) represents the disk evolution in an isolated system, without any perturbation.

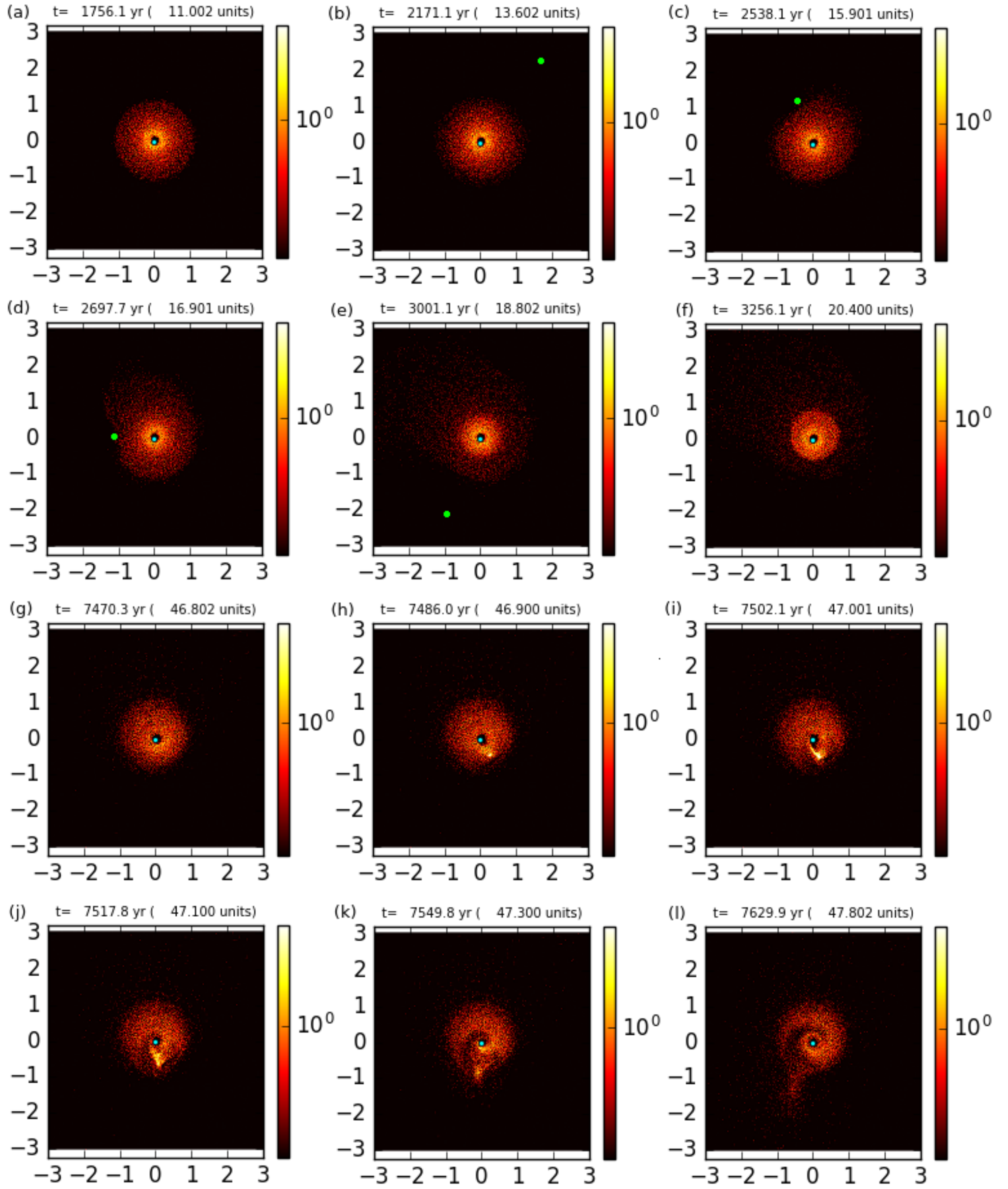

Figure 5.8. Fly-by sequence, related to the FB300 (parameters $b_s = 300AU, v_0 = -1.5kms^-1$). $S2$(green dot) approaches $S1$. Panels from (a) to (f) show the sequence of stars approach, while panels from (g) to (l) show an unphysical phenomenon of explosion: bad shock wave capturing leads to numerical errors. Units for x and y axes = 100 AU. Units for the Density map = 885 $g \cdot cm^{-2}$.

As the graphs show, the gravitational perturbations given by the second star cause an increasing of the flux of matter on $S1$, determining a strong discontinuity in the accretion mass curves. The less b_s, the stronger the perturbation, the stronger is the jump. As it was expected, closer fly-bys causes stronger perturbations, and the inward accretion of matter has a discontinuity during the fly-by time. The rate of inward accretion is restored after the fly-by, as the $S2$ goes far away from $S1$. Figure

5.8, related to the run performed with $b_s = 300AU, v_0 = -1.5kms^-1$, shows a fly-by sequence, starting from a phase in which the disk is in equilibrium. The density map is centered in the coordinates of $S1$, projected on the X,Y plane. As $S2$ approaches $S1$ whithin a distance of the order of r_{disk}, the protoplanetary disk is warped and, after the fly-by, the external layers of gas are expelled outwards and, as a result, the disk is been truncated. During a later phase, the gas expelled falls down again towards $S1$. Then, as can be seen in the second half of panels of figure 5.8, as the gas keeps on falling down, strong increasing of density arises, followed by an umphysical explosion which ejects material from the inner layers of the disk and breaks its' symmetry. As remarked above, the general treatement of the disk viscosity implies the use of a constant and low value for α. Furthermore, since the Morris-Monaghan scheme (3.24) is switched off, there is a lack of a suitable treatement of the shock waves during strong compressions. The latter circumstance, usually never happen during the evolution of a disk, provided that the fluctuations of its density field are low. Such condition could be missed during very close star interactions: the strong dynamical perturbations generated by the passing by star may change abruptly the dynamical equilibrium of the disk, letting layers of matter to merge and leading to strong shock phenomena. In shock waves are not treated properly, several errors could arise, causing a bad extimation of the particles positions and of the velocity field. We need a method to use the coefficient α only when compression occurs, as the classical SPH prescription states, together with the α-disk formalism. For these purposes, in our algorithm we adopted such hybrid scheme for the artificial viscosity:

$$\Pi_{ij} = \begin{cases} \dfrac{-\alpha\bar{c}\mu_{ij} + 2\alpha\mu_{ij}^2}{\bar{\rho_{ij}}} & , \text{ if } \quad \vec{v_{ij}} \cdot \vec{r_{ij}} < 0 \\ \dfrac{-\alpha_{min}\ \bar{c}\mu_{ij} + 2\alpha_{min}\ \mu_{ij}^2}{\bar{\rho_{ij}}} & \text{if } \quad \vec{v_{ij}} \cdot \vec{r_{ij}} > 0 \end{cases} \tag{5.5}$$

The viscosity pressure term now is identical to the 3.21 when two particles approach, the coefficient α is then updated with the usual methods described in section 3.3.2. Thus, even in a disk, when compressions occur, the magnitude of the viscosity increases and shock waves may be captured, while α falls down to the minimum α_{min} (see the 3.24) in case the strength of the velocity divergence is low. On the other hand, when we have a positive value of $\vec{v_{ij}} \cdot \vec{r_{ij}}$, we use the Shakura-Sunyaev prescription and turn on the viscosity just setting a constant value of $\alpha = \alpha_{min}$. As a result, the gas behaves like an α-disk in low perturbed states, with a low viscosity coefficient active both in compression and in dilatation regymes, while it increase it's viscosity just in case a strong merging of particles occurs.

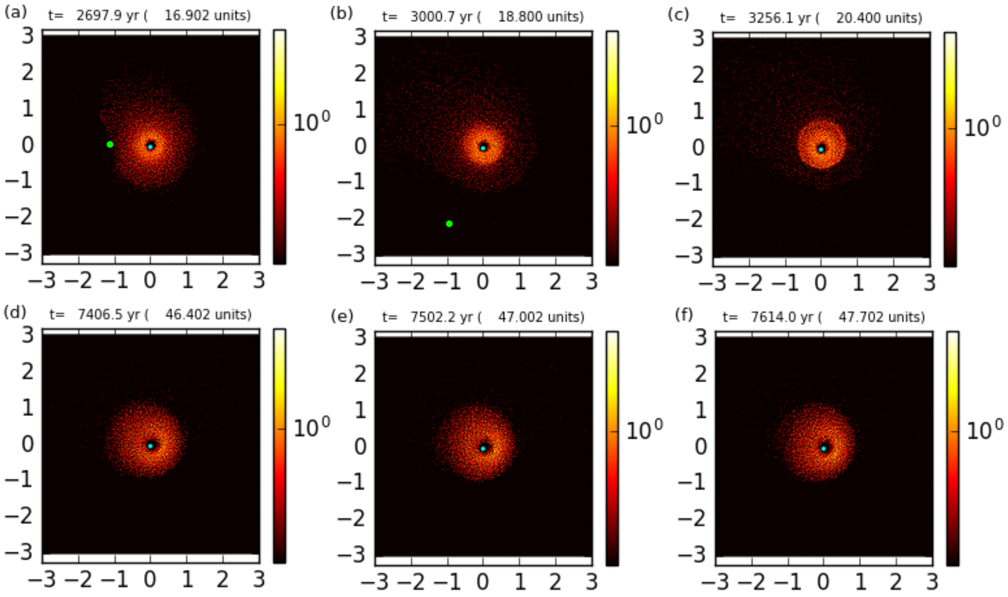

Figure 5.9. Fly-by sequence, related to the new simulation FB300 with Morris-Monaghan scheme included for the viscosity. $S2$(green dot) approaches $S1$(blue dot). Panels from (a) to (c) show the fly-by, while panels from (d) to (f) show the new disk configuration after the fly-by and during the gas infalling (in the same time lapse as the sequence (g)...(l) of figure 5.8. Units for x and y axis: 100 AU. Density map units = 885 $g \cdot cm^{-2}$.

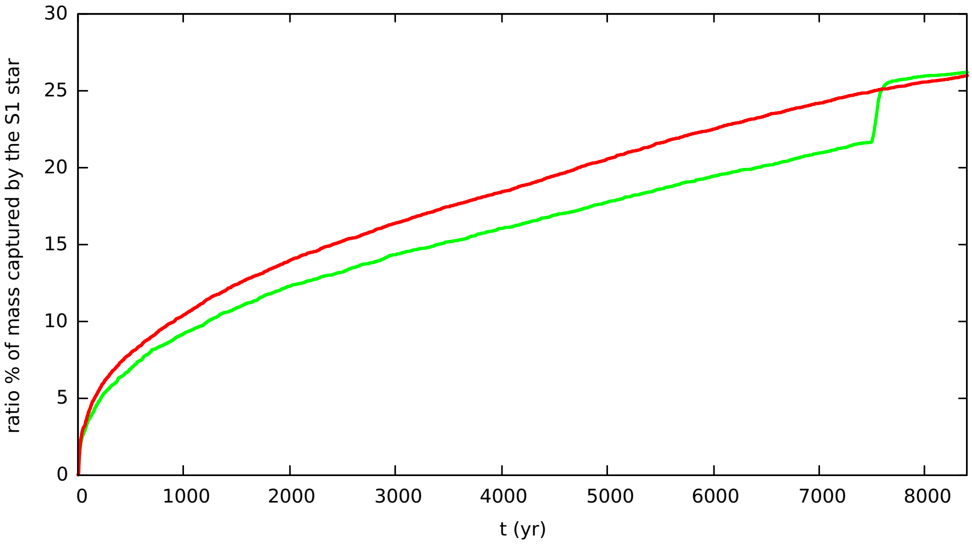

Figure 5.10. Mass accretion in Simulation FB300. Comparison between the two cases of pure α-disk (green line) and hybrid α-disk with artificial viscosity for shock capturing is included (red line).

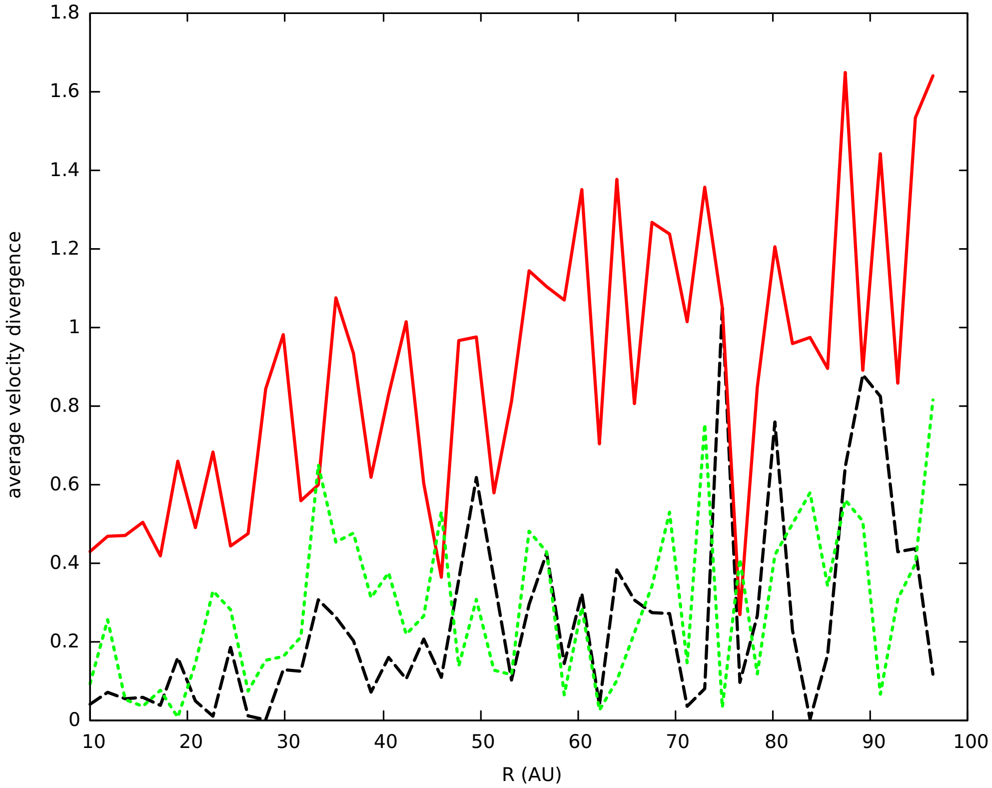

Figure 5.11. Gaseous disk in run FB300 with viscosity correction scheme: azimuthally average relative velocity divergence $\frac{|\vec{\nabla}\cdot\vec{v}|}{|\vec{v}|}$ in function of the radial distance from the star S1. Black dotted curve represents the initial profile. The red full line refers to t= 3000 yr, during the fly-by. Green dashed curve represents the average profile at t=7500 yr, after that the two stars are not close any more (i.e. $|\vec{r}| >> b_s$).

We restarted the test FB300 adopting the new scheme, results are illustrated in figure 5.9 and 5.10. The shock waves now are threated in a proper way and numerical error due to excessive particle overlaps are prevented, as can be seen by the frames related to the same time lapses as the previous simulation. No occasional explosions occur and,after the fly-by, the infalling gas induces non-axisymmetric warps to the outer layers of the disk. Figure 5.11 shows a radial profile for the disk velocity gradient, averaged azimuthally with respect to the radial distance from the central star $S1$. From the graph we can understand that the most important contribution given by the SPH artificial viscosity for the shock waves treatement, arises during the lapse of fly-by (t$\approx$ $3000yr$). On the other hand, while at the beginning of the simulations, when the disk is still in an umperturbed equilibrium, and at $\approx$ $7500yr$, after the fly-by when the star S2 is far away from S1 (i.e the mutual distance $|\vec{r}| >> b_s$), $\frac{|\vec{\nabla}\cdot\vec{v}|}{|\vec{v}|}$ assumes low values.

The Figure 5.12, in the same way as 5.10 made for a single run, shows the mass ratio resulted from the four FB150, FB200, FB250, FB300 made with the new α

prescription. The results are compared with the previous curves in graph 5.7 (panel a). As it can be seen, the less the b_s, the stronger is the different made by the shock waves, and the more prominent is the role of the Morris-Monaghan prescription for a variable α.

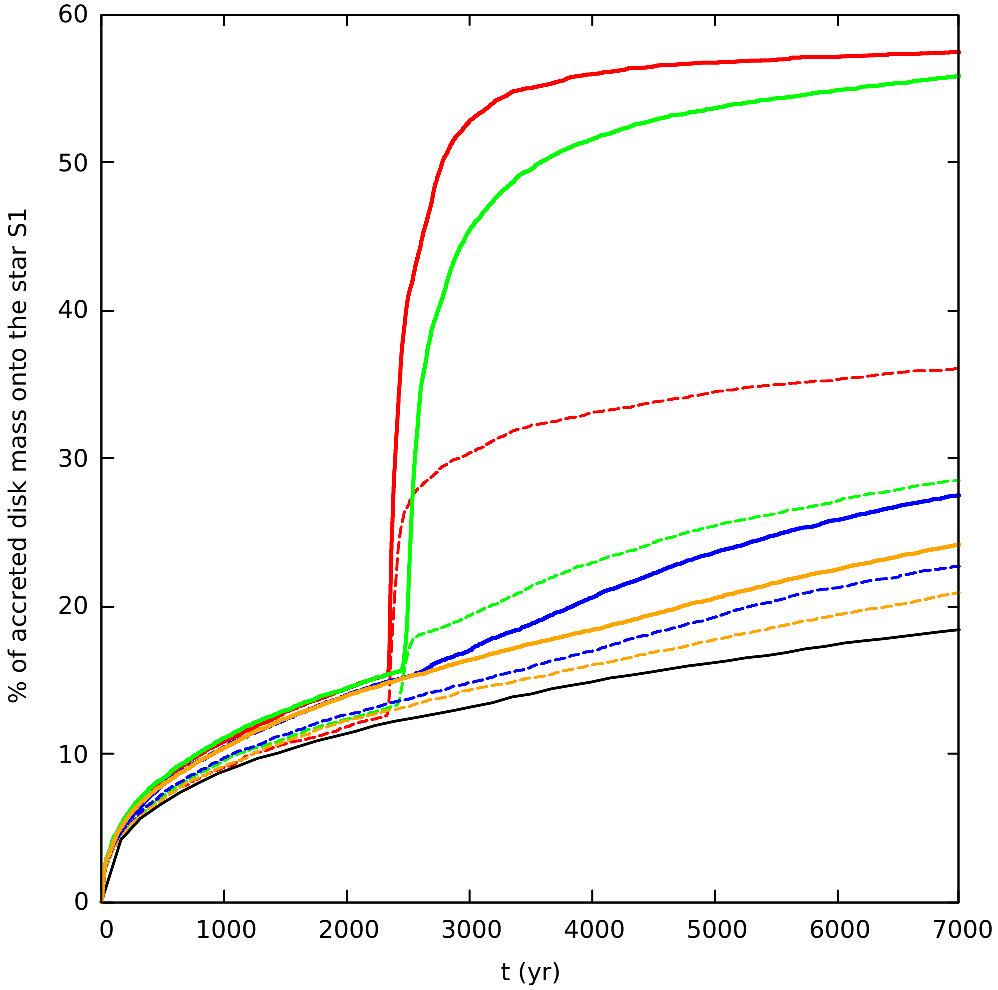

Figure 5.12. Accretion mass ratios to the star S1. General comparison between old runs with simple *alpha*-disk model(dashed lines), and new runs with hybrid prescriptions for the artificial viscosity(dotted line). FB150(red curves), FB200(green curves), FB250(blue curves), FB300(orange curves).

Chapter 6

Conclusions and remarks for the future.

The investigation of protoplanetary disks in complex contexts as open clusters represent a very modern outer reach for the planetology. Understanding the role of complex multi star-systems for the evolution of primordial gaseous disks may give some important answers for the birth of our Solar System, too.

The investigation of such problems involves different systems, with different time-scales, giving rise to several numerical issues.

We have so far developed an SPH-tree based Algorithm with the aim of treating complex system, involving self-gravitating gas and coupling it with an ensemble of ballistic objects. We have tested and used the Code, provided with a set of numerical instruments to integrate the Eulerian Equation of a perfect fluid in a conservative manner. We have investigated the modern problem of close encounters between stars in a complex environment involving protoplanetary disks. For very close encounters (with impact parameter of the order of the disk radius) we have realized that the standard α-disk prescription, introduced by Shakura and Sunyaev in 1973 to model the secular evolution of a protoplanetary disk in a pseudo-equilibrium state around one star, fails because it cannot handle properly the shock waves, and thus needs to be completed with some other suitable schemes.

So far, this work represents the first step, aiming at investigating deeply the complex evolutionary processes involved in the multi-star systems, involving the treatment of the binary stars, too. We aim, for the future, at integrating the code with several suitable instruments in order to treat the interaction between gas and dust, and the propagation of the radiation through matter.

Appendix A

Runge Kutta explicit 14-th order method: technical details

Below we list the non-null elements of the arrays $a_{\beta\gamma}$, b_{β}, c_{β}, introduced in section 3.4.3 (see equations 3.37, 3.38, 3.39).

For the matrix a we have:

a(2,1) = 0.11111111111111111111

a(3,1) = -0.83333333333333333333

a(3,2) = 1.38888888888888888888

a(4,1) = 0.20833333333333333333

a(4,3) = 0.625

a(5,1) = 0.19333333333333333333

a(5,3) = 0.22

a(5,4) = -0.08

a(6,1) = 0.1

a(6,4) = 0.4

a(6,5) = 0.5

a(7,1) = 0.10348456163667977667

a(7,4) = 0.12206888730640722589

a(7,5) = 0.48257449033124662247

a(7,6) = -0.03814096000156069997

a(8,1) = 0.12438052665409441288

a(8,5) = 0.226120282197584301422

a(8,6) = 0.01378858876180808806

a(8,7) = -0.06722101339966844974

a(9,1) = 0.09369190656596738155

a(9,6) = -0.006134068434505109872

a(9,7) = 0.216019825625503063708

a(9,8) = 0.423695063515761937337

a(10,1) = 0.083847981240905266461

a(10,6) = -0.011794936710097381431

a(10,7) = -0.247299020568812652339

a(10,8) = 0.0978080858367729012259

a(10,9) = 0.2175906892434206313600

a(11,1) = 0.06152553597694282279

a(11,6) =0.00592232780324503308

a(11,7) = 0.470326159963841112217

a(11,8) = 0.299688863848679000853

a(11,9) =-0.247656877593994914689

a(11,10) =0.110895029771437682893

a(12,1) =0.0419700073362782579861

a(12,6) =-0.00317987696266205093

a(12,7) =0.8063977149061920772608

a(12,8) =0.0975983126412388979093

a(12,9) =0.7785755781583989090275

a(12,10) =0.204890423831599428189

a(12,11) =-1.56261579627468188307
a(13,1) =0.04377267822337301635 74
a(13,9) = 0.00624365027520195208 7
a(13,10) =0.20004309710957731499 4
a(13,11) =-0.00805328367804983036
a(13,12) =0.02115175280673965219 1
a(14,1) =0.02834992503635145630 95
a(14,9) =0.00249163204855817407 53
a(14,10) =0.02301387878545931496 3
a(14,11) =-0.00322155956692977098
a(14,12) =0.00988442549447664668 9
a(14,13) =-0.02130107713288873513
a(15,1) =.34351189429024300104943
a(15,9) = 0.21045191202362738560 9
a(15,10) =1.03427452057230411936 4
a(15,11) =0.00600303645864422487 0
a(15,12) =0.85593812509961953757 8
a(15,13) =-0.97723500503676681087
a(15,14) =-0.66002698047929469461
a(16,1) =-0.01435740016721680695 3
a(16,9) =-0.03662532700490399702 9
a(16,10) =0.03502549756362136819 7
a(16,11) =0.03609460163621135089 3
a(16,12) =-0.02652199675536811063
a(16,13) =0.04456990113056981196 3
a(16,14) =0.12434309333135824328 6
a(16,15) =0.00413829693239480694 4
a(17,1) =0.35603240442512029097 56
a(17,9) =-0.45019275894756259596 6
a(17,10) =0.43052790708371089862 6
a(17,11) =0.51197302901102223766 8
a(17,12) =0.90830363888640426039 0
a(17,13) =-1.23921093371933931757
a(17,14) =-0.64904866167176146514
a(17,15) =0.25170890458681929221 0
a(17,16) =0.77990647034558639881 0
a(18,1) =0.01309356874065130664 06
a(18,13) =-0.00009320530679851139
a(18,14) =0.05053743342622993596 4
a(18,15) =0.00000080447034194448 7
a(18,16) =0.00059172602949417119 0
a(18,17) =-0.00000040161472215455
a(19,1) =0.02079264844660530125 41
a(19,13) =0.00058269591880008591 5
a(19,14) =-0.00801700732358815939
a(19,15) =0.00000403847643847136 9
a(19,16) =0.08546099980555061442 2
a(19,17) =-0.00000204486480935804
a(19,18) =0.10532857882443189339 9
a(20,1) =1.40153449795736021415 44
a(20,13) =-0.23025200098422126161
a(20,14) =-7.21106840466912905659
a(20,15) =0.00372901560694836335 2
a(20,16) =-4.71415495727125020678
a(20,17) =-0.00176367657545349242
a(20,18) =7.64130548038698765563 0
a(20,19) =3.50602043659751834989 8
a(21,1)=11.951465069412068679 93
a(21,13)=7.7948093210817596878 3
a(21,14)=-56.450139386732579252
a(21,15)=0.0912376306930644901 3
a(21,16)=-12.733627992543488620
a(21,17)=-0.0396895921904719712
a(21,18)=54.439214188357088699 6
a(21,19)=-3.6441163792156923684
a(21,20)=-0.8045032499105099108
a(22,1)=-148.80942650710048842 7
a(22,13)=-91.729527829125648435
a(22,14)=707.65614497159835983 4
a(22,15)=-1.1056361185748244090
a(22,16)=176.13459188381137258 7
a(22,17)=0.4913848242148806622 6
a(22,18)=-684.27800044981494435
a(22,19)=27.991060499839825898 4
a(22,20)=13.193971003028233344 3
a(22,21)=1.2512878128398044545 0

a(23,1)=-9.67307946948196763644
a(23,13)=-4.4699015085850553144
a(23,14)=45.5127128690952681968
a(23,15)=-0.0713085086183826912
a(23,16)=11.2273614068412741582
a(23,17)=0.12624437671762272451
a(23,18)=-43.543933954948331360
a(23,19)=0.78717430754305897839
a(23,20)=0.53226469674468421566
a(23,21)=0.42242273399632532601
a(23,22)=0.08591312495030671073
a(24,1)=-10.0664032447054702403
a(24,9)=-0.03662532700490399702
a(24,10)=0.03502549756362136819
a(24,11)=0.03609460163621135089
a(24,12)=-0.0265219967553681106
a(24,13)=-6.2708897218146414359
a(24,14)=48.2079237442562989090
a(24,15)=-0.0694471689136165640
a(24,16)=12.6810690204850295698
a(24,17)=0.01196711689683237548
a(24,18)=-46.724976499248240800
a(24,19)=1.33029613326626711314
a(24,20)=1.00766787503398298353
a(24,21)=0.02095120519336650916
a(24,22)=0.02101347063312641773
a(24,23)=0.00952196014417121794
a(25,1)=-409.478081677743708772
a(25,9)=0.210451912023627385609
a(25,10)=1.03427452057230411936
a(25,11)=0.00600303645864422487
a(25,12)=0.85593812509961953757
a(25,13)=-250.51699854744786049
a(25,14)=1946.42466652388427766
a(25,15)=-3.0450388210231036550
a(25,16)=490.626379528281713521
a(25,17)=1.56647589531270907115
a(25,18)=-1881.9742899401117336
a(25,19)=75.2592224724847175278
a(25,20)=34.5734356980331067622
a(25,21)=3.21147679440968961435
a(25,22)=-0.4604080417384143913
a(25,23)=-0.0870718339841810522
a(25,24)=-7.3935181415830306756
a(26,1)=3.433474758535508789210
a(26,9)=0.002491632048558174075
a(26,10)=0.02301387878545931496
a(26,11)=-0.0032215595669297709
a(26,12)=0.00988442549447664668
a(26,13)=2.16252799377922507788
a(26,14)=-16.269986454645742132
a(26,15)=-0.1285345021205245528
a(26,16)=-8.9891504266650425308
a(26,17)=-0.0034859536323202533
a(26,18)=15.7936194113339807536
a(26,19)=-0.5744033309140950656
a(26,20)=-0.3456020390213932966
a(26,21)=-0.0066224149020658509
a(26,22)=-0.0077778812924220416
a(26,23)=-0.0035608419240227491
a(26,24)=4.79282506449930799649
a(26,25)=0.15372546487306857784
a(27,1)=32.30385208719854423269
a(27,6)=-0.00317987696266205093
a(27,7)=0.806397714906192077260
a(27,8)=0.097598312641238897909
a(27,9)=0.778575578158398909027
a(27,10)=0.20489042383159942818
a(27,11)=-1.5626157962746818830
a(27,13)=16.3429891882310570648
a(27,14)=-154.54455529354362123
a(27,15)=1.56971088703334872692
a(27,16)=3.27685545087248131321
a(27,17)=-0.0503489245193653176
a(27,18)=153.321151858041665070
a(27,19)=7.17568186327720495846

a(27,20)=-2.9403674867530048194
a(27,21)=-0.0665845946076803144
a(27,22)=-0.0462346054990843661
a(27,23)=-0.0204198733585679401
a(27,24)=-53.352310643873585051
a(27,25)=-1.3554871471507865497
a(27,26)=-1.5719627580123275188
a(28,1)=-16.645146748634151287 2
a(28,6)=0.0059223278032450330 80
a(28,7)=0.4703261599638411122
a(28,8)=0.2996888638486790008
a(28,9)=-0.247656877593994914
a(28,10)=0.110895029771437682
a(28,12)=-0.4917190438462291470
a(28,13)=-11.474315442728949696
a(28,14)=80.2593166576230272541
a(28,15)=-0.384132303980042847
a(28,16)=7.2814766746810758347 1
a(28,17)=-0.1326993846122483795
a(28,18)=-81.079983252573072667
a(28,19)=-1.2503749283562063952
a(28,20)=2.5926359496954368102 3
a(28,21)=-0.3014402983464045398
a(28,22)=0.2213844607898323374 5
a(28,23)=0.0827577274771892931 9
a(28,24)=18.996066204061152046 4
a(28,25)=0.2692319464096396856 2
a(28,26)=1.6267482744706653746 2
a(28,27)=0.4917190438462291470 7
a(29,1)=0.0838479812409052664 61
a(29,6)=-0.0117949367100973814 3
a(29,7)=-0.2472990205688126523 3
a(29,8)=0.0978080858367729012 25
a(29,9)=0.2175906892434206313 60
a(29,11)=0.1375856067633252248 6
a(29,12)=0.0439870229715046685 0
a(29,14)=-0.5137008137681933419
a(29,15)=0.8263556911513155086 4
a(29,16)=25.701813971981183262 5
a(29,24)=-25.701813971981183262
a(29,25)=-0.8263556911513155086
a(29,26)=0.5137008137681933419 5
a(29,27)=-0.0439870229715046685
a(29,28)=-0.1375856067633252248
a(30,1)=0.1243805266540944128 81
a(30,5)=0.2261202821975843014 22
a(30,6)=0.0137885887618080880 60
a(30,7)=-0.0672210133996684449 7
a(30,10)=-0.8562389750854283547
a(30,11)=-1.9633752286685890892
a(30,12)=-0.2323328227241194012
a(30,14)=4.3066071908645334946 1
a(30,15)=-2.9272296324946548265
a(30,16)=-82.313166639785894445
a(30,24)=82.313166639785894445 4
a(30,25)=2.9272296324946548265 9
a(30,26)=-4.3066071908645334946
a(30,27)=0.2323328227241194012 3
a(30,28)=1.9633752286685890892 8
a(30,29)=0.8562389750854283547 5
a(31,1)=0.1034845616366797766 72
a(31,4)=0.1220688873064072225 89
a(31,5)=0.4825744903312466224 75
a(31,6)=-0.0381409600015606999 7
a(31,8)=-0.5504995253108023241 3
a(31,10)=-0.7119158115851892278
a(31,11)=-0.5841296056715513404
a(31,14)=2.1104630812586493211
a(31,15)=-0.0837494736739572 1
a(31,16)=5.1002149907232091 40
a(31,24)=-5.100214990723209 14
a(31,25)=0.0837494736739572 13
a(31,26)=-2.1104630812586493 2
a(31,28)=0.5841296056715513 40
a(31,29)=0.7119158115851892 27
a(31,30)=0.5504995253108023 24

a(32,1)=0.19333333333333333333
a(32,3)=0.22
a(32,4)=-0.08
a(32,7)=0.10999342558072470391
a(32,8)=-0.25429704807627016 13
a(32,10)=0.86557077711669425 4
a(32,11)=3.32416449114093083 1
a(32,14)=-12.0102223315977933
a(32,15)=0.47660146624249323 9
a(32,16)=-29.0243011221036390
a(32,24)=29.02430112210363905
a(32,25)=-0.47660146624249323
a(32,26)=12.01022233159779338
a(32,28)=-3.324164491140930
a(32,29)=-0.865570777116694
a(32,30)=0.2542970480762701
a(32,31)=-0.109993425580724
a(33,1)=-0.8333333333333333
a(33,2)=1.38888888888888888
a(33,5)=-0.75
a(33,7)=-0.49252954371802630
a(33,31)=0.49252954371802630
a(33,32)=0.75
a(34,1)=0.11111111111111111111
a(34,3)=-0.22222222222222222
a(34,33)=0.22222222222222222
a(35,1)=0.28583514038897155 8
a(35,2)=0.29166666666666666
a(35,3)=0.21875

a(35,5)=0.1640625
a(35,7)=0.21819435494555665 8
a(35,8)=0.18039289847869776 6
a(35,10)=0.20571383940484501
a(35,11)=0.24271579158177023
a(35,12)=0.24646578081362930
a(35,13)=0-3.449919407908908
a(35,14)=0.22887556216003608
a(35,15)=0.28329059970215141
a(35,16)=3.21085125837766640
a(35,17)=-0.2235387773648456
a(35,18)=-0.7071211572044190
a(35,19)=3.21123345150287080
a(35,20)=1.40954348309669766
a(35,21)=-0.1513620534437426
a(35,22)=0.37235057452701427
a(35,23)=0.25297874640636133
a(35,24)=-3.2108512583776664
a(35,25)=-0.2832905997021514
a(35,26)=-0.2288755621600360
a(35,27)=-0.2464657808136293
a(35,28)=-0.2427157915817702
a(35,29)=-0.2057138394048450
a(35,30)=-0.1803928984786977
a(35,31)=-0.2181943549455566
a(35,32)=-0.1640625
a(35,33)=-0.21875
a(35,34)=-0.2916666666666666

Non-null elements of the array b :

b(1) = 0.0178571428571428
b(2) = 0.005859375
b(3) = 0.01171875
b(5) = 0.017578125 b(7) = 0.0234375
b(8) = 0.029296875
b(10) = 0.03515625
b(11) = 0.041015625

b(12) = 0.046875
b(14) = 0.052734375
b(15) = 0.05859375
b(16) = 0.064453125
b(18) = 0.1053521135717530
b(19) = 0.170561346241752
b(20) = 0.2062293973293519

b(21) = 0.2062293973293519
b(22) = 0.17056134624175218
b(23) = 0.10535211357175301
b(24) = -0.064453125
b(25) = -0.05859375
b(26) = -0.052734375
b(27) = -0.046875
b(28) = -0.041015625
b(29) = -0.03515625
b(30) = -0.029296875 b(31) = -0.0234375
b(32) = -0.017578125
b(33) = -0.01171875
b(34) = -0.005859375
b(35) = 0.0178571428571428

Non-null elements of the array c :

c(1) = 0
c(2) = 1/9
c(3) = 5/9
c(4) = 5/6
c(5) = 1/3
c(6) = 1
c(7) = 0.669986979272772921
c(8) = 0.297068384213818357
c(9) = 0.727272727272727273
c(10) = 0.140152799042188765
c(11) = 0.700701039770150738
c(12) = 0.363636363636363637
c(13) = 0.263157894736842106
c(14) = 0.0392172246650270860
c(15) = 0.812917502928376762
c(16) = 0.166666666666666667
c(17) = 0.9
c(18) = 0.0641299257451966692
c(19) = 0.204149909283428849
c(20) = 0.395350391048760565
c(21) = 0.604649608951239434
c(22) = 0.795850090716571151
c(23) = 0.935870074254803308
c(24) = 0.166666666666666667
c(25) = 0.812917502928376762
c(26) = 0.039217224665027085
c(27) = 0.363636363636363636
c(28) = 0.700701039770150737
c(29) = 0.140152799042188765
c(30) = 0.297068384213818357
c(31) = 0.669986979272772921
c(32) = 1/3
c(33) = 5/9
c(34) = 1/9
c(35) = 1

Bibliography

S. J. Aarseth. From NBODY1 to NBODY6: The Growth of an Industry. *Publications of the ASP*, 111:1333–1346, Nov. 1999. doi: 10.1086/316455.

M. P. Allen and D. J. Tildesley. *Computer Simulation of Liquids*. Clarendon Press, New York, NY, USA, 1989. ISBN 0-19-855645-4.

ALMA Partnership, C. L. Brogan, L. M. Pérez, T. R. Hunter, W. R. F. Dent, A. S. Hales, R. E. Hills, S. Corder, E. B. Fomalont, C. Vlahakis, Y. Asaki, D. Barkats, A. Hirota, J. A. Hodge, C. M. V. Impellizzeri, R. Kneissl, E. Liuzzo, R. Lucas, N. Marcelino, S. Matsushita, K. Nakanishi, N. Phillips, A. M. S. Richards, I. Toledo, R. Aladro, D. Broguiere, J. R. Cortes, P. C. Cortes, D. Espada, F. Galarza, D. Garcia-Appadoo, L. Guzman-Ramirez, E. M. Humphreys, T. Jung, S. Kameno, R. A. Laing, S. Leon, G. Marconi, A. Mignano, B. Nikolic, L.-A. Nyman, M. Radiszcz, A. Remijan, J. A. Rodón, T. Sawada, S. Takahashi, R. P. J. Tilanus, B. Vila Vilaro, L. C. Watson, T. Wiklind, E. Akiyama, E. Chapillon, I. de Gregorio-Monsalvo, J. Di Francesco, F. Gueth, A. Kawamura, C.-F. Lee, Q. Nguyen Luong, J. Mangum, V. Pietu, P. Sanhueza, K. Saigo, S. Takakuwa, C. Ubach, T. van Kempen, A. Wootten, A. Castro-Carrizo, H. Francke, J. Gallardo, J. Garcia, S. Gonzalez, T. Hill, T. Kaminski, Y. Kurono, H.-Y. Liu, C. Lopez, F. Morales, K. Plarre, G. Schieven, L. Testi, L. Videla, E. Villard, P. Andreani, J. E. Hibbard, and K. Tatematsu. The 2014 ALMA Long Baseline Campaign: First Results from High Angular Resolution Observations toward the HL Tau Region. *Astrophysical Journal, Letters*, 808:L3, July 2015. doi: 10.1088/2041-8205/808/1/L3.

H. C. Andersen. Rattle: A ”Velocity” Version of the Shake Algorithm for Molecular Dynamics Calculations. *Journal of Computational Physics*, 52:24–34, Oct. 1983. doi: 10.1016/0021-9991(83)90014-1.

P. Artymowicz and S. H. Lubow. Dynamics of binary-disk interaction. 1: Resonances and disk gap sizes. *Astrophysical Journal*, 421:651–667, Feb. 1994. doi: 10.1086/173679.

Attwood, R. E., Goodwin, S. P., and Whitworth, A. P. Adaptive smoothing lengths in sph. *Astronomy and Astrophysics*, 464(2):447–450, 2007. doi: 10.1051/0004-6361:20066606. URL `https://doi.org/10.1051/0004-6361:20066606`.

S. A. Balbus and J. F. Hawley. Instability, turbulence, and enhanced transport in accretion disks. *Rev. Mod. Phys.*, 70:1–53, Jan 1998. doi: 10.1103/RevModPhys.70.1. URL `https://link.aps.org/doi/10.1103/RevModPhys.70.1`.

D. S. Balsara. von Neumann stability analysis of smooth particle hydrodynamics–suggestions for optimal algorithms. *Journal of Computational Physics*, 121:357–372, 1995. doi: 10.1016/S0021-9991(95)90221-X.

J. Barnes and P. Hut. A hierarchical O(N log N) force-calculation algorithm. *Nature*, 324:446–449, Dec. 1986. doi: 10.1038/324446a0.

J. E. Barnes. *The Use of Supercomputers in Stellar Dynamics: Proceedings of a Workshop Held at the Institute for Advanced Study Princeton, USA, June 2–4, 1986*, chapter An efficient N-body algorithm for a fine-grain parallel computer, pages 175–180. Springer Berlin Heidelberg, Berlin, Heidelberg, 1986. ISBN 978-3-540-47361-9. doi: 10.1007/BFb0116409. URL `http://dx.doi.org/10.1007/BFb0116409`.

Bhandare, Asmita, Breslau, Andreas, and Pfalzner, Susanne. Effects of inclined star-disk encounter on protoplanetary disk size. *Astronomy and Astrophysics*, 594:A53, 2016. doi: 10.1051/0004-6361/201628086. URL `https://doi.org/10.1051/0004-6361/201628086`.

J. Binney and S. Tremaine. *Galactic dynamics*. Princeton University Press, Princeton, NJ, 1987.

A. P. Boss. Giant planet formation by gravitational instability. *Science*, 276:1836–1839, 1997. doi: 10.1126/science.276.5320.1836.

A. P. Boss. Evolution of the Solar Nebula. IV. Giant Gaseous Protoplanet Formation. *Astrophysical Journal*, 503:923–937, Aug. 1998. doi: 10.1086/306036.

A. P. Boss. Rapid Formation of Outer Giant Planets by Disk Instability. *Astrophysical Journal*, 599:577–581, Dec. 2003. doi: 10.1086/379163.

A. Brandenburg, A. Nordlund, R. F. Stein, and U. Torkelsson. Dynamo-generated Turbulence and Large-Scale Magnetic Fields in a Keplerian Shear Flow. *Astrophysical Journal*, 446:741, June 1995. doi: 10.1086/175831.

R. L. Brown, W. Wild, and C. Cunningham. ALMA - the Atacama large millimeter array. *Advances in Space Research*, 34:555–559, Jan. 2004. doi: 10.1016/j.asr.2003.03.028.

R. Capuzzo-Dolcetta and P. Miocchi. A comparison between the fast multipole algorithm and the tree-code to evaluate gravitational forces in 3-D. *Journal of Computational Physics*, 143:29–48, June 1998. doi: 10.1006/jcph.1998.5949.

R. Capuzzo-Dolcetta, M. Spera, and D. Punzo. A fully parallel, high precision, n-body code running on hybrid computing platforms. *Journal of Computational Physics*, 236:580 – 593, 2013. ISSN 0021-9991. doi: http://doi.org/10.1016/j.jcp.2012.11.013. URL `http://www.sciencedirect.com/science/article/pii/S0021999112006900`.

P. J. Cossins. *Smoothed Particle Hydrodynamics*. PhD thesis, PhD Thesis, 2010, July 2010.

P. D'Alessio, N. Calvet, L. Hartmann, S. Lizano, and J. Cantó. Accretion Disks around Young Objects. II. Tests of Well-mixed Models with ISM Dust. *Astrophysical Journal*, 527:893–909, Dec. 1999. doi: 10.1086/308103.

J. I. Dehnen, W.and Read. N-body simulations of gravitational dynamics. *The European Physical Journal Plus*, 126(5):55, May 2011. ISSN 2190-5444. doi: 10.1140/epjp/i2011-11055-3. URL `https://doi.org/10.1140/epjp/i2011-11055-3`.

W. Dehnen. Towards optimal softening in three-dimensional N-body codes - I. Minimizing the force error. *Monthly Notices of the RAS*, 324:273–291, June 2001. doi: 10.1046/j.1365-8711.2001.04237.x.

C. P. Dullemond, D. Hollenbach, I. Kamp, and P. D'Alessio. Models of the Structure and Evolution of Protoplanetary Disks. *Protostars and Planets V*, pages 555–572, 2007.

A. S. Eddington. The distribution of stars in globular clusters. *Monthly Notices of the RAS*, 76:572–585, May 1916. doi: 10.1093/mnras/76.7.572.

A. E. Evrard. Beyond N-body - 3D cosmological gas dynamics. *Monthly Notices of the RAS*, 235:911–934, Dec. 1988. doi: 10.1093/mnras/235.3.911.

T. Feagin. High-order explicit runge-kutta methods using m-symmetry. *Neural, Parallel and Scientific Computations*, 20:437–458, 09 2012.

P. J. V. Garcia. *Physical Processes in Circumstellar Disks around Young Stars*. The University of Chicago Press, May 2011.

R. A. Gingold and J. J. Monaghan. Smoothed particle hydrodynamics - Theory and application to non-spherical stars. *Monthly Notices of the RAS*, 181:375–389, Nov. 1977. doi: 10.1093/mnras/181.3.375.

Y. Hasegawa and T. Takeuchi. Viscous instability triggered by layered accretion in protoplanetary disks. *The Astrophysical Journal*, 815(2):99, 2015. URL `http://stacks.iop.org/0004-637X/815/i=2/a=99`.

C. Hayashi. Structure of the solar nebula, growth and decay of magnetic fields and effects of magnetic and turbulent viscosities on the nebula. *Progress of Theoretical Physics Supplement*, 70:35–53, 1981. doi: 10.1143/PTPS.70.35. URL `+http://dx.doi.org/10.1143/PTPS.70.35`.

L. Hernquist. Performance characteristics of tree codes. *Astrophysical Journal, Supplement*, 64:715–734, Aug. 1987. doi: 10.1086/191215.

L. Hernquist. Some cautionary remarks about smoothed particle hydrodynamics. *Astrophysical Journal*, 404:717–722, Feb. 1993. doi: 10.1086/172325.

L. Hernquist and N. Katz. TREESPH - A unification of SPH with the hierarchical tree method. *Astrophysical Journal, Supplement*, 70:419–446, June 1989. doi: 10.1086/191344.

J. Hernández, M. Morales-Calderon, N. Calvet, L. Hartmann, J. Muzerolle, R. Gutermuth, K. L. Luhman, and J. Stauffer. Spitzer observations of the lambda orionis cluster. ii. disks around solar-type and low-mass stars. *The Astrophysical Journal*, 722(2):1226, 2010. URL `http://stacks.iop.org/0004-637X/722/i=2/a=1226`.

R. W. Hockney and J. W. Eastwood. *Computer simulation using particles.* Bristol: Hilger, 1988.

N. Hosono, T. R. Saitoh, and J. Makino. A comparison of sph artificial viscosities and their impact on the keplerian disk. *The Astrophysical Journal Supplement Series*, 224(2):32, 2016. URL `http://stacks.iop.org/0067-0049/224/i=2/a=32`.

D. A. Hubber, R. J. Allison, R. Smith, and S. P. Goodwin. A hybrid SPH/N-body method for star cluster simulations. *Monthly Notices of the RAS*, 430:1599–1616, Apr. 2013. doi: 10.1093/mnras/sts694.

P. Hut, J. Makino, and S. McMillan. Building a better leapfrog. *Astrophysical Journal, Letters*, 443:L93–L96, Apr. 1995. doi: 10.1086/187844.

J. J. Lissauer. Timescales for planetary accretion and the structure of the protoplanetary disk. *Icarus*, 69:249–265, Feb. 1987. doi: 10.1016/0019-1035(87)90104-7.

J. J. Lissauer. Planet formation. *Annual Review of Astron and Astrophys*, 31:129–174, 1993. doi: 10.1146/annurev.aa.31.090193.001021.

G. Lodato and D. J. Price. On the diffusive propagation of warps in thin accretion discs. *Monthly Notices of the Royal Astronomical Society*, 405(2):1212–1226, 2010. doi: 10.1111/j.1365-2966.2010.16526.x. URL `+http://dx.doi.org/10.1111/j.1365-2966.2010.16526.x`.

G. Lodato and J. E. Pringle. Warp diffusion in accretion discs: a numerical investigation. *Monthly Notices of the Royal Astronomical Society*, 381(3):1287–1300, 2007. doi: 10.1111/j.1365-2966.2007.12332.x. URL `+http://dx.doi.org/10.1111/j.1365-2966.2007.12332.x`.

S. H. Lubow and R. G. Martin. The evolution of planet–disk systems that are mildly inclined to the orbit of a binary companion. *The Astrophysical Journal*, 817(1):30, 2016. URL `http://stacks.iop.org/0004-637X/817/i=1/a=30`.

L. B. Lucy. A numerical approach to the testing of the fission hypothesis. *Astronomical Journal*, 82:1013–1024, Dec. 1977. doi: 10.1086/112164.

D. Lynden-Bell and J. E. Pringle. The evolution of viscous discs and the origin of the nebular variables. *Monthly Notices of the RAS*, 168:603–637, Sept. 1974. doi: 10.1093/mnras/168.3.603.

R. K. Mann, S. M. Andrews, J. A. Eisner, J. P. Williams, M. R. Meyer, J. D. Francesco, J. M. Carpenter, and D. Johnstone. Protoplanetary disk masses in the young ngc 2024 cluster. *The Astrophysical Journal*, 802(2):77, 2015. URL `http://stacks.iop.org/0004-637X/802/i=2/a=77`.

R. G. Martin, C. Nixon, S. H. Lubow, P. J. Armitage, D. J. Price, S. Doğan, and A. King. The kozai-lidov mechanism in hydrodynamical disks. *The Astrophysical Journal Letters*, 792(2):L33, 2014. URL `http://stacks.iop.org/2041-8205/792/i=2/a=L33`.

L. Mayer, T. Quinn, J. Wadsley, and J. Stadel. Formation of Giant Planets by Fragmentation of Protoplanetary Disks. *Science*, 298:1756–1759, Nov. 2002. doi: 10.1126/science.1077635.

L. Mayer, T. Quinn, J. Wadsley, and J. Stadel. The evolution of gravitationally unstable protoplanetary disks: Fragmentation and possible giant planet formation. *The Astrophysical Journal*, 609(2):1045, 2004. URL `http://stacks.iop.org/0004-637X/609/i=2/a=1045`.

Z. Meglicki, D. Wickramasinghe, and G. V. Bicknell. Three-Dimensional Structure of Truncated Accretion Discs in Close Binaries. *Monthly Notices of the RAS*, 264: 691, Oct. 1993. doi: 10.1093/mnras/264.3.691.

D. Merritt. Optimal Smoothing for N-Body Codes. *Astronomical Journal*, 111:2462, June 1996. doi: 10.1086/117980.

F. Meru and M. R. Bate. On the convergence of the critical cooling time-scale for the fragmentation of self-gravitating discs. *Monthly Notices of the RAS*, 427: 2022–2046, Dec. 2012. doi: 10.1111/j.1365-2966.2012.22035.x.

P. Miocchi and R. Capuzzo-Dolcetta. An efficient parallel tree-code for the simulation of self-gravitating systems. *Astronomy and Astrophysics*, 382:758–767, Feb. 2002. doi: 10.1051/0004-6361:20011609.

J. J. Monaghan. Particle methods for hydrodynamics. *Computer Physics Reports*, 3: 71–124, Oct. 1985. doi: 10.1016/0167-7977(85)90010-3.

J. J. Monaghan. An introduction to SPH. *Computer Physics Communications*, 48: 89–96, Jan. 1988. doi: 10.1016/0010-4655(88)90026-4.

J. J. Monaghan. On the problem of penetration in particle methods. *Journal of Computational Physics*, 82:1–15, May 1989. doi: 10.1016/0021-9991(89)90032-6.

J. J. Monaghan. Smoothed particle hydrodynamics. *Annual Review of Astron and Astrophys*, 30:543–574, 1992. doi: 10.1146/annurev.aa.30.090192.002551.

J. J. Monaghan. Smoothed particle hydrodynamics. *Reports on Progress in Physics*, 68:1703–1759, Aug. 2005. doi: 10.1088/0034-4885/68/8/R01.

J. J. Monaghan and R. A. Gingold. Shock Simulation by the Particle Method SPH. *Journal of Computational Physics*, 52:374–389, Nov. 1983. doi: 10.1016/0021-9991(83)90036-0.

J. J. Monaghan and J. C. Lattanzio. A refined particle method for astrophysical problems. *Astronomy and Astrophysics*, 149:135–143, Aug. 1985.

J. P. Morris and J. J. Monaghan. A Switch to Reduce SPH Viscosity. *Journal of Computational Physics*, 136:41–50, Sept. 1997. doi: 10.1006/jcph.1997.5690.

B. Mukhopadhyay. Estimate of the shakura–sunyaev viscosity parameter in the keplerian accretion disk from hydrodynamic turbulence. *International Journal of Modern Physics D*, 17(03n04):467–473, 2008. doi: 10.1142/S0218271808012139. URL `http://www.worldscientific.com/doi/abs/10.1142/S0218271808012139`.

A. F. Nelson, W. Benz, F. C. Adams, and D. Arnett. Dynamics of Circumstellar Disks. *Astrophysical Journal*, 502:342–371, July 1998. doi: 10.1086/305869.

A. F. Nelson, W. Benz, and T. V. Ruzmaikina. Dynamics of Circumstellar Disks. II. Heating and Cooling. *Astrophysical Journal*, 529:357–390, Jan. 2000. doi: 10.1086/308238.

C. R. O'dell, Z. Wen, and X. Hu. Discovery of new objects in the Orion nebula on HST images - Shocks, compact sources, and protoplanetary disks. *Astrophysical Journal*, 410:696–700, June 1993. doi: 10.1086/172786.

C. Olczak, S. Pfalzner, and R. Spurzem. Encounter-triggered Disk Mass Loss in the Orion Nebula Cluster. *Astrophysical Journal*, 642:1140–1151, May 2006. doi: 10.1086/501044.

C. Olczak, T. Kaczmarek, S. Harfst, S. Pfalzner, and S. P. Zwart. The evolution of protoplanetary disks in the arches cluster. *The Astrophysical Journal*, 756(2):123, 2012. URL `http://stacks.iop.org/0004-637X/756/i=2/a=123`.

Pfalzner, S. Early evolution of the birth cluster of the solar system. *Astronomy and Astrophysics*, 549:A82, 2013. doi: 10.1051/0004-6361/201218792. URL `https://doi.org/10.1051/0004-6361/201218792`.

B. K. Pickett, P. Cassen, R. H. Durisen, and R. Link. The Effects of Thermal Energetics on Three-dimensional Hydrodynamic Instabilities in Massive Protostellar Disks. *Astrophysical Journal*, 504:468–491, Sept. 1998. doi: 10.1086/306059.

B. K. Pickett, P. Cassen, R. H. Durisen, and R. Link. The Effects of Thermal Energetics on Three-dimensional Hydrodynamic Instabilities in Massive Protostellar Disks. II. High-Resolution and Adiabatic Evolutions. *Astrophysical Journal*, 529: 1034–1053, Feb. 2000. doi: 10.1086/308301.

H. C. Plummer. On the problem of distribution in globular star clusters. *Monthly Notices of the RAS*, 71:460–470, Mar. 1911. doi: 10.1093/mnras/71.5.460.

D. J. Price and J. J. Monaghan. An energy-conserving formalism for adaptive gravitational force softening in smoothed particle hydrodynamics and N-body codes. *Monthly Notices of the RAS*, 374:1347–1358, Feb. 2007. doi: 10.1111/j.1365-2966.2006.11241.x.

T. Quinn, N. Katz, J. Stadel, and G. Lake. Time stepping N-body simulations. *ArXiv Astrophysics e-prints*, Oct. 1997.

Riols, A., Rincon, F., Cossu, C., Lesur, G., Ogilvie, G. I., and Longaretti, P. -Y. Dissipative effects on the sustainment of a magnetorotational dynamo in keplerian shear flow. *Astronomy and Astrophysics*, 575:A14, 2015. doi: 10.1051/0004-6361/201424324. URL `https://doi.org/10.1051/0004-6361/201424324`.

A. B. Romeo. Modelling gravity in N-body simulations of disc galaxies. Optimal types of softening for given dynamical requirements. *Astronomy and Astrophysics*, 335:922–928, July 1998.

G. P. Rosotti, J. E. Dale, M. de Juan Ovelar, D. A. Hubber, J. M. D. Kruijssen, B. Ercolano, and S. Walch. Protoplanetary disc evolution affected by star–disc interactions in young stellar clusters. *Monthly Notices of the Royal Astronomical Society*, 441(3):2094–2110, 2014. doi: 10.1093/mnras/stu679. URL `+http://dx.doi.org/10.1093/mnras/stu679`.

S. Rosswog and D. Price. MAGMA: a three-dimensional, Lagrangian magnetohydrodynamics code for merger applications. *Monthly Notices of the RAS*, 379:915–931, Aug. 2007. doi: 10.1111/j.1365-2966.2007.11984.x.

S. Rosswog, M. B. Davies, F.-K. Thielemann, and T. Piran. Merging neutron stars: asymmetric systems. *Astronomy and Astrophysics*, 360:171–184, Aug. 2000.

S. M. Rucinski. IRAS observations of T Tauri and post-T Tauri stars. *Astronomical Journal*, 90:2321–2330, Nov. 1985. doi: 10.1086/113937.

T. R. Saitoh and J. Makino. A necessary condition for individual time steps in sph simulations. *The Astrophysical Journal Letters*, 697(2):L99, 2009. URL `http://stacks.iop.org/1538-4357/697/i=2/a=L99`.

L. I. Sedov. *Similarity and Dimensional Methods in Mechanics.* CRC Press, Inc., 1959.

N. I. Shakura and R. A. Sunyaev. Black holes in binary systems. Observational appearance. *Astronomy and Astrophysics*, 24:337–355, 1973.

F. H. Shu, F. C. Adams, and S. Lizano. Star formation in molecular clouds - Observation and theory. *Annual Review of Astron and Astrophys*, 25:23–81, 1987. doi: 10.1146/annurev.aa.25.090187.000323.

V. Springel. The cosmological simulation code GADGET-2. *Monthly Notices of the RAS*, 364:1105–1134, Dec. 2005. doi: 10.1111/j.1365-2966.2005.09655.x.

V. Springel and L. Hernquist. Cosmological smoothed particle hydrodynamics simulations: the entropy equation. *Monthly Notices of the RAS*, 333:649–664, July 2002. doi: 10.1046/j.1365-8711.2002.05445.x.

R. Spurzem. Direct n-body simulations. *Journal of Computational and Applied Mathematics*, 109(1):407 – 432, 1999. ISSN 0377-0427. doi: https://doi.org/10.1016/S0377-0427(99)00166-1. URL `http://www.sciencedirect.com/science/article/pii/S0377042799001661`.

D. Stamatellos, A. Maury, A. Whitworth, and P. André. The lower limits of disc fragmentation and the prospects for observing fragmenting discs. *Monthly Notices of the Royal Astronomical Society*, 413(3):1787–1796, 2011. doi: 10.1111/j.1365-2966.2011.18254.x. URL `+http://dx.doi.org/10.1111/j.1365-2966.2011.18254.x`.

E. J. Tasker, R. Brunino, N. L. Mitchell, D. Michielsen, S. Hopton, F. R. Pearce, G. L. Bryan, and T. Theuns. A test suite for quantitative comparison of hydrodynamic codes in astrophysics. *Monthly Notices of the RAS*, 390:1267–1281, Nov. 2008. doi: 10.1111/j.1365-2966.2008.13836.x.

A. Toomre. On the gravitational stability of a disk of stars. *Astrophysical Journal*, 139:1217–1238, May 1964. doi: 10.1086/147861.

C. A. Tout. Current understanding of accretion disc viscosity. *New Astronomy Review*, 44:37–40, Apr. 2000. doi: 10.1016/S1387-6473(00)00010-5.

Vincke, Kirsten, Breslau, Andreas, and Pfalzner, Susanne. Strong effect of the cluster environment on the size of protoplanetary discs? *Astronomy and Astrophysics*, 577:A115, 2015. doi: 10.1051/0004-6361/201425552. URL `https://doi.org/10.1051/0004-6361/201425552`.

M. S. Warren and J. K. Salmon. Astrophysical n-body simulations using hierarchical tree data structures. In *Proceedings of the 1992 ACM/IEEE Conference on Supercomputing*, Supercomputing '92, pages 570–576, Los Alamitos, CA, USA, 1992. IEEE Computer Society Press. ISBN 0-8186-2630-5. URL `http://dl.acm.org/citation.cfm?id=147877.148090`.

M. Wetzstein, A. F. Nelson, T. Naab, and A. Burkert. Vine—a numerical code for simulating astrophysical systems using particles. i. description of the physics and the numerical methods. *The Astrophysical Journal Supplement Series*, 184(2):298, 2009. URL `http://stacks.iop.org/0067-0049/184/i=2/a=298`.